Vortices on curved surfaces

Ari M. Turner

Department of Physics, Harvard University, Cambridge Massachusetts 02138, USA and Department of Physics, University of California, Berkeley, California 94720, USA

Vincenzo Vitelli

Instituut-Lorentz for Theoretical Physics, Leiden University, Leiden NL 2333 CA, The Netherlands

David R. Nelson

Department of Physics, Harvard University, Cambridge Massachusetts 02138, USA

(Published 30 April 2010)

Topological defects in thin films coating a deformed substrate interact with the underlying curvature. This coupling mechanism influences the shape of biological structures and provides a new strategy for the design of interfaces with prescribed functionality. In this article, a mathematical formalism based on the method of conformal mapping that is presented permits the calculation of the energetics of disclinations, dislocations, and vortices on rigid substrates of spatially varying Gaussian curvature. Special emphasis is placed on determining the geometric force exerted on vortices in curved superfluid films. This force, which attracts (repels) vortices towards regions of negative (positive) Gaussian curvature, is an illustration of how material shape can influence quantum mechanical degrees of freedom.

DOI: 10.1103/RevModPhys.82.1301 PACS number(s): 67.25.dk, 61.30.Jf, 02.40.Hw, 05.30.Jp

CONTENTS

I. Introduction 1301
II. Overview of Basic Concepts 1303
III. Fluid Dynamics and Vortex-Curvature Interactions 1306
A. Anomalous force on rotationally symmetric surfaces 1308
B. Vortex-trapping surfaces 1310
C. Negative curvature which does not trap 1311
D. Hysteresis of vortices and trapping strength 1313
IV. Rotating Superfluid Films on a Corrugated Substrate 1313
A. The effect of rotation 1313
B. Single defect ground state 1314
C. Multiple defect configurations 1316
D. Abrikosov lattice on a curved surface 1317
V. Experimental Considerations 1318
A. The van der Waals force and thickness variation 1319
VI. Complex Surface Morphologies 1320
A. Derivation of the self-energy by conformal mapping 1322
B. Vortices on a "soap film" surface 1325
C. Periodic surfaces 1326
D. Band flows on elongated surfaces 1328
E. Interactions on a closed surface 1331
VII. Limits on the Strength and Range of Geometrical Forces 1333
VIII. Conclusion 1335
Acknowledgments 1336
Appendix A: Nearly Flat Surfaces 1336
Appendix B: The Saddle Surface's Potential 1337
Appendix C: van der Waals Attraction on a Curved Surface 1338
Appendix D: Guide to Green's Functions on Compact Surfaces 1340
Appendix E: Approximations for Long Surfaces of Revolution 1341
Appendix F: Derivations of Bounds Valid Even for Strong Distortions 1345
References 1347

I. INTRODUCTION

The delicate interplay between geometry and condensed matter order has provided a fascinating venue to develop sophisticated theoretical ideas that, along with experimental investigations, contribute to the appeal of the subject (Bowick and Travesset, 2001; Kamien, 2002; Nelson, 2002b; Witten, 2007). This is particularly evident in the study of two-dimensional (2D) systems characterized by the condition that the sample thickness is much smaller than its lateral extension (Cerda and Mahadevan, 2005). The separation of length scales often implies that these thin layers can be easily bent, naturally raising the question of how the imposed geometric deformations couple to the in-plane order (David *et al.*, 1987; Nelson and Peliti, 1987). For example, bending a plate into a surface of nonvanishing Gaussian curvature causes a stretching of its elastic bonds. Several pioneering ideas and mathematical methods that address this issue have been first introduced while investigating the rich physics of membranes and interfaces modeled as a surface whose shape is itself subject to thermal fluctuations (de Gennes and Taupin, 1982; Helfrich, 1985; Peliti and Leibler, 1985; Kantor *et al.*, 1987; Aronovitz and Lubensky, 1988; Duplantier, 1989; Gompper and Kroll, 1997; Kohyama *et al.*, 2003).

Fueled by the drive towards technological applications based on the notion of self-assembly directed by

geometry, considerable research efforts have recently been invested in understanding the properties of thin liquid crystal or crystalline layers draped over a *frozen* topography (Sachdev and Nelson, 1984; Bowick *et al.*, 2000; Blanc and Kleman, 2001; Vitelli and Nelson, 2006; Santangelo *et al.*, 2007). The rigidity condition is easily satisfied experimentally by monolayers confined on curved interfaces between two immiscible fluids whose surface tension dominates over thermal fluctuations (Dinsmore *et al.*, 2002; Bausch *et al.*, 2003; Subramaniam *et al.*, 2005; Fernandez-Nieves *et al.*, 2007) and for films wetting a solid surface (Hexemer, 2006; Irvine *et al.*, 2009). The coupling between in-plane order and the geometry of the substrate opens up a novel venue to control the self-assembly of interfaces with tailored functionality (Nelson, 2002a; DeVries *et al.*, 2007). In the natural world, this coupling plays a role in determining the shape of biological structures, such as viral shells (Ganser *et al.*, 1999; Li *et al.*, 2000; Lidmar *et al.*, 2003; Nguyen *et al.*, 2005) and cell membranes (McMahon and Gallop, 2005). The challenge to the theorist is to predict the large elastic deformations that take place in these two-dimensional materials as a result of the strong geometric constraints. In this nonlinear regime, perturbative expansions from a flat zero-energy configuration fail and one has to resort to more versatile tools such as the method of conformal mapping. This technique is frequently utilized to solve complicated boundary value problems in fluid mechanics and electromagnetism (Guyon *et al.*, 2001), or to picture space-times in general relativity with the help of Penrose diagrams (D'Inverno, 1992). One objective of this article is to illustrate, by means of examples, how conformal transformations can aid the study of order and defects on curved surfaces (Ovrut and Thomas, 1991; Lubensky and Prost, 1992; Vitelli and Turner, 2004).

Topological defects in two dimensions come in different varieties such as vortices, disclinations, and dislocations, depending on the type of order they disrupt (Kleman and Friedel, 2008). The simplest type of defect occurs in two-dimensional neutral superfluids that can be approximately described by an XY model; that is to say, an angle-valued field representing the local phase of the superfluid wave function. A topological defect in this field is a point around which the phase increases by an integer multiple of 2π. For most purposes such defects can be regarded as 2D "electrostatic" charges interacting logarithmically and with charge equal to the phase change around a path enclosing each of them. For other phases, the form of the interaction between defects is characteristic of the symmetry of the order parameter and the type of discontinuity which the topological defect engenders.

On a surface with a varying Gaussian curvature, a single defect experiences an additional one-body geometric potential, which reflects the broken translational invariance of the substrate and the type of order in the monolayer. For example, the regular lattice preferred by the particles in a 2D crystal is distorted when the crystal is bent. Defects seek locations of the surface where they can help ease the bond stretching or compression induced by the curvature of the surface. A dislocation in a 2D crystal is a defect located at the end of an extra "half-row" of atoms. Inserting part of a row of atoms in a stretched region of the curved monolayer releases the tension in the bonds. In this case, the topological charge is the Burger vector, which is perpendicular to the extra row of atoms and has a magnitude comparable to the lattice spacing (Nelson, 2002b). The Burger vector prefers particular orientations in the tangent plane of the surface and can be viewed as a defect dipole moment. The energetically favored orientation of the dipole ensures that the extra row of atoms is inserted in the most stretched part of the surface; for example, on the top of a bump (Vitelli *et al.*, 2006). Likewise, defects in a liquid crystal on a curved surface experience a geometric potential because of the coupling of the liquid crystal director to the surface (Park and Lubensky, 1996; Bowick *et al.*, 2004; Achard *et al.*, 2005; Jiang *et al.*, 2007; Chen and Kamien, 2009).

More surprising is the existence of a coupling between defects in a superfluid film and the curvature of the underlying substrate, since the phase angle of the superfluid wave function does not indicate a direction in the tangent space of the surface, as does the angle describing the local orientation of the bonds in a curved crystal (Vitelli and Turner, 2004). Nonetheless in all these two-dimensional systems, defects can be described by an effective free energy cast in terms of particles (the defects) interacting among each other and with a smeared out charge distribution (the underlying Gaussian curvature). In the remainder of this article, we derive the form of these interactions by conformal mappings and clarify their origin for vortices and liquid crystal disclinations with an emphasis on the former. The application of these techniques to the problem of curved-space crystallography has been reviewed from a similar perspective by Bowick and Giomi (2009).

There are two reasons behind our choice of concentrating on vortices in thin layers of liquid helium. On the one hand, superfluid order provides the simplest setting to introduce more general ideas about order and geometry by concentrating on a simple scalar field theory cast in terms of the phase of the superfluid wave function. On the other hand, it presents a paradigmatic example of how *quantum* degrees of freedom are influenced by the shape of materials (da Costa, 1981; Entin and Magarill, 2001; Atanasov and Dandoloff, 2008). This novel arena extends through the traditional boundaries of disciplines as diverse as applied mechanics and quantum physics and holds promise for the design of devices based on curved quasi-two-dimensional nanostructures (Tanda *et al.*, 2002; Duan *et al.*, 2003).

Determining the geometric forces for defects on rigid substrates can be regarded as the inverse problem of studying the buckling of a membrane (Seung and Nelson, 1988). As an illustration, consider a defect located at a fixed position in a flexible elastic sheet. In order to screen the strain induced by the defect, the initially flat substrate will buckle into a curved surface with a char-

acteristic shape that depends qualitatively on the type of defect and on the symmetry of the order parameter (Pomeau, 1998; Frank and Kardar, 2008). Conversely, the energy of a defected monolayer confined on a *rigid* surface can be minimized by moving the defects so that the deformations they induce in the monolayer conform to the curvature of the underlying substrate.

The geometrical force on a single defect is a long-range interaction that depends on the inhomogeneous distribution of Gaussian curvature throughout the surface. This means that naive approximations that rely on a Taylor expansion of the curvature around the location of the defect are bound to fail. By contrast, the method of conformal mapping illustrated in this article rests on a change of coordinates that maps the entirety of a complicated surface onto a disk or a perfect sphere whose simpler metric is fully amenable to analytical treatment. The kernel of the defect-curvature interaction, usually the inverse of the Laplacian (or bi-Laplacian) operator on the curved surface, can be found on the simplified surface and then transformed back to the physical substrate. In this review we explain how to perform this crucial step and highlight the subtleties involved in dealing with a nonflat metric.

Describing an ordered phase in terms of the interactions of its defects is a more convenient, mesoscopic approach than keeping track of the state of the microscopic components, e.g., individual particle positions or molecular orientations. The energetics of the defects provides a useful starting point from which one can derive the curvature-induced inhomogeneities in the thermal and mechanical properties of many two-dimensional materials. Indeed, topological defects are the linchpin of the concept of topological phase transition (Berezinskii, 1971; Kosterlitz and Thouless, 1973). At low temperature, vortices and antivortices are tightly bound in dipole pairs. A topological phase transition occurs above a critical temperature for which entropic effects win over the energy cost of nucleating a defect. This leads to a high-temperature phase characterized by a plasma of unbound vortices. A similar mechanism underpins the defect mediated melting of two-dimensional crystalline monolayers (Kosterlitz and Thouless, 1973; Halperin and Nelson, 1978; Young, 1979).

Unlike their flat-space counterparts, crystalline and liquid crystalline monolayers confined on a curved substrate typically have unbound defects even in their ground state which are not generated thermally. The simplest mechanism relies on the presence of a global constraint that the sum of the topological charges must satisfy on a closed surface (Kamien, 2002). For example, a vector field continuously defined on a sphere must have at least two defects each with topological charge 2π; think of the lines of latitude on the globe that naturally create two vortices at the north and south poles. More generally, the Poincaré-Hopf theorem states that the sum of all topological charges must be exactly 4π, that is, equal to the integral of the Gaussian curvature over the area of the sphere (Cole, 1974; Volodin *et al.*, 1977; Salomaa and Williams, 1981; MacKintosh and Lubensky, 1991; Evans, 1996; Dodgson and Moore, 1997; Pérez-Garrido *et al.*, 1997; Bowick *et al.*, 2000; Tempere *et al.*, 2001; Chantawansri *et al.*, 2007; Shin *et al.*, 2008; Xing, 2008).

Even in the absence of any topological constraints or boundary conditions that force their presence, defects can still be nucleated at zero temperature to minimize the elastic energy of a curved crystalline or liquid crystalline monolayer (Vitelli and Nelson, 2004; Hexemer *et al.*, 2007; Giomi and Bowick, 2008). Typically, a dimensionless control parameter characterizing the curvature of the substrate (e.g., the aspect ratio of a bump) plays the role of temperature. Above a certain threshold of the geometric control parameter, a cascade of defect unbinding instabilities takes place to screen the preexisting elastic deformations (Kohyama and Gompper, 2003; Bowick *et al.*, 2004; Giomi and Bowick, 2007; Hexemer *et al.*, 2007).

II. OVERVIEW OF BASIC CONCEPTS

In flat space both superfluid and liquid crystal films can be described, as a first approximation, by the XY model (Nelson and Kosterlitz, 1977), which focuses on the statistics of a position-dependent angle. This angle can equally represent either the phase of the superfluid wave function or the angle of the director of the liquid crystal, a vector (with both ends identified in the case of a nematic phase) describing the local orientation of the chainlike molecules in the film. Despite the obvious similarities, there is a fundamental difference between these two classes of systems. The angle of the liquid crystal director lives in the tangent space of the surface while the phase angle is a quantum mechanical object that transforms like a *scalar* since it is defined in an internal space. This subtle difference resurfaces upon considering the distinct curved-space generalizations of the XY model that apply to each of these two systems.

On a curved surface, the liquid crystal order is geometrically frustrated (Sadoc and Mosseri, 2006). Geometrical frustration also occurs in magnetic systems, where it can affect thermodynamic properties dramatically. A system is said to be geometrically frustrated if the molecular arrangements favored by local interactions cannot be extended throughout space (Toulouse, 1977; Moessner and Ramirez, 2006). The simplest example is the ground state of the two-dimensional antiferromagnet on a triangular lattice. Consider classical spin degrees of freedom that can be in either an up or down position. The interaction of a pair of neighboring spins may favor their orientations to be opposite. In order to see the origin of the frustration focus on the spins on a triangular unit cell. If the first spin is up then the next one encountered by traveling clockwise around the triangle must be down. By the same reasoning the next one on the path must be up. However, if a final step is taken to close the loop, one returns to the initial vertex whose spin has already been assigned to be up. Therefore there is no way to satisfy all pair interactions encountered on these closed loops. As a result, there is an

unavoidable "strain" (and typically a large degeneracy) in the ground state whose energy cannot be made to vanish. These general properties of geometric frustration depend critically on the combined choice of lattice geometry and local interactions. (Note that there is no geometric frustration for an antiferromagnet on a square lattice or a ferromagnet on a triangular lattice.).

The concept of geometric frustration provides a point of view for studying several phenomena involving spin glasses, artificial ice, frustrated colloidal systems, and bulk properties of some liquid crystals (Kleman, 1987; Ramirez, 2005; Libal *et al.*, 2006; Wang *et al.*, 2006; Han *et al.*, 2008; Qi *et al.*, 2008). Several investigations of the properties of glasses and amorphous solids rely on the concept of frustration and often employ models defined on a curved space (Nelson, 1983; Tarjus *et al.*, 2005; Modes and Kamien, 2007, 2008).

Liquid crystal molecules constrained to be tangent to a curved substrate cannot be oriented parallel to their neighbors. The free-energy functional $\mathcal{F}_{\text{vector}}$ to be minimized for the case of orientational order on a surface with points labeled by the coordinates $\mathbf{u}=(u_1,u_2)$ reads (David, 1989)

$$\mathcal{F}_{\text{vector}} = \frac{K}{2}\int d^2u\sqrt{g}g^{\alpha\beta}[\partial_\alpha\theta(\mathbf{u}) - \Omega_\alpha(\mathbf{u})] \times[\partial_\beta\theta(\mathbf{u}) - \Omega_\beta(\mathbf{u})], \tag{1}$$

where $g_{\alpha\beta}$ and g indicate the metric tensor and its determinant while $\Omega_\alpha(\mathbf{u})$ is a connection that compensates for the rotation of the 2D basis vectors $\mathbf{E}_\alpha(\mathbf{u})$ [with respect to which $\theta(\mathbf{u})$ is measured] in the direction of the u_α coordinate axis (Kamien, 2002).

The crucial mathematical result, needed in this context, is that the curl of the field $\Omega_\alpha(\mathbf{u})$ is equal to the Gaussian curvature $G(\mathbf{u})$ (David, 1989). As a result, the positive definite integrand in the free energy of Eq. (1) cannot vanish everywhere because the field $\Omega_\alpha(\mathbf{u}) \neq \partial_\alpha\theta$ cannot be expressed as the gradient of a "potential" field, on a surface with curl $\Omega = G(\mathbf{u}) \neq 0$. Therefore, the orientational order is geometrically frustrated. In analogy with the example of the antiferromagnet considered above, the local direction of the liquid crystal molecules in adjacent portions of an arbitrary loop cannot be parallel everywhere if the Gaussian curvature is nonvanishing. As the substrate becomes more curved, the resulting energy cost of frustration can be lowered by generating disclination dipoles in the ground state even in the absence of topological constraints.

The connection $\Omega_\alpha(\mathbf{u})$ is a geometric gauge field akin to the electromagnetic vector potential, with the Gaussian curvature playing the role of a magnetic field. If topological defects are present, they appear as monopoles in the singular part of $\partial_\alpha\theta(\mathbf{u})$. In analogy with electromagnetic theory, their interaction with the Gaussian curvature arises mathematically from the cross terms between $\partial_\alpha\theta(\mathbf{u})$ and the geometry-induced vector potential $\Omega_\alpha(\mathbf{u})$, see Eq. (1). As a result of this interaction, disclinations in a liquid crystal are attracted to regions of the substrate whose curvature has the same sign as the defect's topological charge (Park and Lubensky, 1996), whereas vortices in a superfluid will be shown to favor negatively curved regions independently of their sense of circulation.

For a disclination in a vector field with topological index n_i (defined by the amount, in units of 2π, that θ increases along a path enclosing the defect's core), the geometric interaction $E_{\text{vector}}(\mathbf{u}_i)$ reads (Vitelli and Turner, 2004)

$$E_{\text{vector}}(\mathbf{u}_i) = 2\pi K n_i(1 - n_i/2)U_G(\mathbf{u}_i), \tag{2}$$

where K is the elastic stiffness and U_G is the geometric potential obtained from solving a covariant Poisson equation with the Gaussian curvature $G(\mathbf{u}_i)$ acting as a source,

$$\nabla^2 U_G(\mathbf{u}_i) = G(\mathbf{u}_i). \tag{3}$$

Note that in addition to the gauge coupling just discussed, which gives rise to the term linear in n_i, there is also a correction to the energy of liquid crystal disclinations that is quadratic in n_i. The latter term occurs even in systems that are not geometrically frustrated, such as vortices in superfluid films.

To understand the distinct physical and mathematical mechanisms behind these two terms, note that in a geometrically frustrated system like a liquid crystal the gauge coupling between defects and the underlying curvature is mediated by the deformed ground-state texture that exists in the liquid crystal layer prior to the introduction of the defects simply as a result of geometrical constraints. Once a defect is introduced it interacts with these preexisting elastic deformations. Unlike the case of orientational order, no geometric frustration exists in the superfluid film, as may be seen from the expression for the superfluid free energy $\mathcal{F}_{\text{scalar}}$. This free energy is a simple scalar generalization of the familiar flat space counterpart

$$\mathcal{F}_{\text{scalar}} = \frac{K}{2}\int d^2u\sqrt{g}g^{\alpha\beta}\partial_\alpha\theta(\mathbf{u})\partial_\beta\theta(\mathbf{u}), \tag{4}$$

where $K=\rho_s\hbar^2/m^2$ is the superfluid stiffness expressed in terms of the ^{4}He atomic mass m and the superfluid mass density ρ_s. The crucial point is that no connection $\Omega_\alpha(\mathbf{u})$ is necessary to write down the covariant derivative for this simpler case of a scalar order parameter. Therefore the ground state is given by $\theta(\mathbf{x})$ equal to a constant and the corresponding energy vanishes. There is no preexisting deformation of the field for a vortex to interact with, and so only the second term from Eq. (2) remains,

$$E_{\text{scalar}}(\mathbf{u}_i) = -\pi K n_i^2 U_G(\mathbf{u}_i), \tag{5}$$

where $U_G(\mathbf{u}_i)$ is the potential defined in Eq. (3). A distinct mechanism is required to explain the existence of this coupling in spite of the absence of a connection. As we see, this additional interaction, henceforth referred to as the anomalous coupling, is a self-energy originating from the distortion of a vortex's own flow pattern by the protrusions and wrinkles of the surface.

In the following sections, we derive this self-interaction by conformal mapping. The interaction implies that, when an isolated vortex is placed on a curved surface, it feels a force as if there were a background topological charge jointly proportional to the vortex's own circulation and the Gaussian curvature across the substrate. Such an imaginary topological charge distribution produces a *real* force analogous to the force exerted on an electrostatic charge by its mirror image in a conducting surface.

The method of conformal mapping may seem, *prima facie*, a surprising route to derive a coupling between vortices and geometry, because the free energy of Eq. (4) is invariant under conformal mappings. These transformations introduce a nonuniform compression of the surface while keeping local angles unchanged. This invariance property at first seems to rule out the possibility of a geometrical interaction. This apparent contradiction can be seen by choosing a special set of (isothermal) coordinates that brings the two-dimensional metric tensor into the diagonal form $g_{\alpha\beta}(\mathbf{u})=e^{2\omega(\mathbf{u})}\delta_{\alpha\beta}(\mathbf{u})$. [In fact, such a coordinate system can be constructed for any surface. This result is due to Gauss, Riemann, and Koebe and is presented in David (1989).] The result of this step is to eliminate the geometry dependence from the free energy of Eq. (4) since the product $g^{\alpha\beta}(\mathbf{u})\sqrt{g}=\delta_{\alpha\beta}(\mathbf{u})$ and $\mathcal{F}_{\text{scalar}}$ reduces to its counterpart for a planar surface, where there is, of course, no geometry dependence.

An interaction between vortices and geometry violates this conformal symmetry of the free energy from which it emerges. The point to keep in mind is that the conformal symmetry is not an exact property of this theory when vortices are present. Analogous subtleties frequently arise in the study of fields that fluctuate thermally or quantum mechanically (Capper and Duff, 1974), due to the occurrence of a cutoff length scale below which fluctuations cannot occur. A conformal mapping is a symmetry only of the continuum model of a system; it stretches lengths and therefore does not preserve the structure at a microscopic scale. At finite temperatures, the discreteness of a system, such as a thermally fluctuating membrane (Polyakov, 1981), which is actually made up of a network of molecules, can have an important effect because the fluctuations excite modes with microscopic wavelengths. This produces violations of the conformal symmetry at every point of the surface. In a superfluid at *zero temperature*, however, short wavelengths not describable by the continuum free energy $\mathcal{F}_{\text{scalar}}$ are only excited in the cores of vortices.

Obtaining a finite value for the energy necessitates the removal of vortex cores of a certain fixed radius in the local tangent plane, so a conformal mapping is not a symmetry in the neighborhood of a vortex. However, the amount by which this symmetry fails can be calculated in a simple form (independent of the microscopic model of the cores) in terms of the rescaling function $\omega(\mathbf{u})$ evaluated at the locations of the vortices, where the symmetry fails.

Rather than ruling out the possibility of a geometric interaction, a realistic treatment of conformal mapping becomes a powerful mathematical tool for deriving these interactions. In general, whenever a symmetry of a field theory is broken by introducing a small distance cutoff, additional terms are generated that describe the symmetry breaking. Such terms are dubbed anomalies. The calculation of conformal anomalies is useful in several branches of theoretical physics such as the study of scattering amplitudes in string theory (Polyakov, 1987) and quantum field theory in curved space-time (Birrell and Davies, 1982). The Hawking radiation from a black hole and possibly the smallness of the cosmological constant can also be related to conformal anomalies (Christensen and Fulling, 1977; Antoniadis *et al.*, 2007).

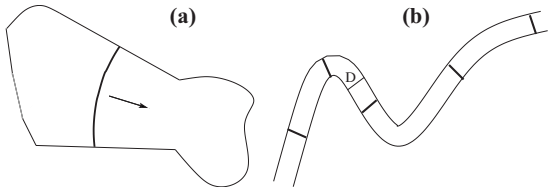

FIG. 1. Cross sections of two regions in which one can study vortex energetics. (a) A region with nonparallel boundaries. The vortex is pushed to the right. This tendency can be interpreted in terms of either a drive toward a shorter length or as the local induction force due to the curvature in the vortex enforced by the boundaries. (b) A cross section of a constant thickness layer of helium bounded above by air and below by the substrate. The vortices keep a constant length and remain straight while moving around. Hence there is no local induction force or thickness-variation force to overwhelm the geometrical forces that we focus on.

While the free energy $\mathcal{F}_{\text{scalar}}$ of the curved superfluid layer in Eq. (4) does not incorporate a *geometric* gauge field, rotating the sample at a constant angular velocity leads to an energy of the same form as Eq. (1). The resulting forces exerted on the vortices compete with the geometric interactions to determine the equilibrium configurations of an arrangement of topological defects. This simple idea is behind some of the experimental suggestions put forward in this article to map out the geometric potential by progressively increasing the rotational speed while monitoring the equilibrium position of, say, a single vortex on a helium-coated surface. Since the position dependence of the force induced by the rotation is easily calculated, one can read off the geometric interaction by assuming force balance.

The theory of curved helium films also helps build intuition for the more general case of vortex lines confined in a bounded three-dimensional (3D) region such as the cavity shown by the cross section in Fig. 1(a). The vortex, drawn as a bold black line, can be pinned by the constriction of the container. The classic problem of understanding the interaction of the vortex with itself and with the bump as the superfluid flows past (Schwarz, 1981) is of crucial importance in elucidating how vortices can be produced when a superfluid starts rotating despite the absence of any friction. A possible mechanism, known as the "vortex mill," assumes that vortex rings break off a pinned vortex line, while the pinned vortex

remains in place (Glaberson and Donnelly, 1966; Schwarz, 1990). A current experiment is investigating how a single pinned vortex moves in chambers of various shapes (Voll *et al.*, 2006; Zieve and Neumann, 2010). The common theoretical route to studying vortex dynamics in three-dimensional geometries is the "local induction approximation," which assumes that each element of a vortex experiences a force determined only by its local radius of curvature. This simplifying assumption omits any long-range forces experienced by the vortices as they interact with the boundaries (or among themselves). In the opposite limit of films with uniform thickness [which can be thought of as special types of bulk superfluid regions with two parallel boundaries, as in Fig. 1(b)], all the forces exerted on the vortices are long range. This is the regime of interest to our investigation.

This article is organized in two parts. The first, comprising Secs. III–V, is phenomenological in nature and emphasizes intuitive analogies between the (nonlinear) geometric forces and conventional electrostatics, simple illustrations of the main results, and experimental ideas. The second, Secs. VI and VII, is more technical and presents a unified derivation of the geometric potential by conformal mapping and its application to the study of complex surface morphologies.

The first part starts with a review of superfluid dynamics that can be used to relate the anomalous coupling to hydrodynamic lift. In Sec. III.A, the geometrical force is evaluated, using a mapping between the geometric potential studied here and the familiar Newton's theorem that allows an efficient calculation of the gravitational field for a spherically symmetric mass distribution. An intriguing consequence of this analogy is that vortices on saddle surfaces can be trapped in regions of negative curvature, leading to geometrically confined persistent currents as discussed in Sec. III.B. Section III.C relates this observation to Earnshaw's theorem from electrostatics. Upon heating and subsequently cooling a curved superfluid film, some of the thermally generated defects can remain trapped in metastable states located at the saddles of the substrate. The existence of such geometry-induced vortex hysteresis is conjectured in Sec. III.D. In Sec. IV.A we derive the forces experienced by vortices when the vessel containing the superfluid layer is rotated around the axis of symmetry of a curved surface shaped as a Gaussian bump. The dependence of single- and multiple-defect configurations on the angular speed and aspect ratio of the bump is studied in Secs. IV.B and IV.C. The Abrikosov lattice of vortices on a curved surface is discussed in Sec. IV.D. In realistic experimental situations, a possible hindrance to observing these phenomena is that the thickness of the superfluid layer will not be uniform and additional forces will drive vortices towards thinner regions of the sample. The strength of these forces is assessed in Sec. V and related to spatial variations of the film thickness due to gravity and surface tension.

The second part starts with a general derivation of the geometric potential by conformal mapping in Sec. VI.A. The computational efficiency of this approach is illustrated in Sec. VI.B, where the geometric potential of a vortex is evaluated on an Enneper disk, a strongly deformed minimal surface. The next three sections show that changing the geometry of the substrate has interesting effects not only on the one-body geometric potential but also on the two-body interaction between vortices: In Sec. VI.C we use conformal methods to show how a periodic lattice of bumps can cause the vortex interaction to become anisotropic. In Sec. VI.D we demonstrate that the quantization of circulation leads to an extremely long-range force on an elongated surface with the topology of a sphere. The interaction energy is no longer logarithmic, but now grows linearly with the distance between the two vortices. As we demonstrate, the whole notion of splitting the energy in a one-body geometric potential and a vortex-vortex interaction is subject to ambiguities on deformed spheres. Section VI.E provides some guidance on how to perform calculations in this context by choosing a convenient Green's function among the several available. Finally, in Sec. VII we present a discussion of some general upper bounds which constrain the strength of geometric forces. The conclusion serves as a concise summary and contains a table designed to locate at a glance our main results throughout the article, including the more technical points relegated to appendices but useful to perform calculations.

III. FLUID DYNAMICS AND VORTEX-CURVATURE INTERACTIONS

In superfluid helium, vortices form when the helium is rotated rapidly or when there is turbulence (Vinen, 1958, 1969; Tilley and Tilley, 1990; Nemirovskii and Fiszdon, 1995). Though such vortices are similar to the vortices that make up a vortex street behind the wings of an airplane or to the funnel clouds of tornadoes, they are only an angstrom or two across (Guyon *et al.*, 2001). A more essential difference is that the vortices in a superfluid do not need a constant source of energy to survive. In fact, a vortex is long lived because the strength of its flow is fixed by the quantization of angular momentum. Thus, the dissipative mechanisms of a conventional fluid are absent.

We start by writing down the collective wave function of the superfluid as

$$\Psi(\mathbf{u}) = \sqrt{\rho_s(\mathbf{u})/m}e^{i\theta(\mathbf{u})}, \tag{6}$$

where $\mathbf{u}=\{u_1,u_2\}$ is a set of curvilinear coordinates for the surface, m is the mass of a ^{4}He atom, and ρ_s is the superfluid mass density that we assume to be constant. To obtain the superfluid current we use the standard expression $j_\alpha(\mathbf{u})=(i\hbar/2m)(\Psi\partial_\alpha\Psi^*-\Psi^*\partial_\alpha\Psi)$, showing that the superfluid velocity is given by

$$v_\alpha(\mathbf{u}) = (\hbar/m)\partial_\alpha\theta(\mathbf{u}). \tag{7}$$

The circulation along a path C enclosing a vortex is given by

$$\oint_C du^\alpha v_\alpha = n\kappa, \tag{8}$$

where the quantum of circulation $\kappa = h/m$ is equal to 9.98×10^{-8} m^2 s^{-1} and the integer n is the topological index of the vortex. The free energy can be cast in the form

$$E = \frac{1}{2}\rho_s \frac{\hbar^2}{m^2}\int_S d^2u \sqrt{g} g^{\alpha\beta}\partial_\alpha\theta\partial_\beta\theta, \tag{9}$$

where $g^{\alpha\beta}$ is the (inverse) metric tensor describing the surface on which the superfluid layer lies and g is its determinant. We use the superfluid stiffness

$$K = \rho_s\hbar^2/m^2. \tag{10}$$

This expression for the free energy can be parametrized in terms of the vortex positions once the seemingly divergent kinetic energy near a vortex core is correctly accounted for. As is well known, the radius independence of the circulation about a vortex implies that the velocity in its proximity is given by $\hbar/mr$, which leads to a logarithmic divergence in Eq. (9). The energy stored in an annulus of internal radius r_{in} and outer radius r_{out} reads

$$E_{\text{near}} = \pi K \ln(r_{\text{out}}/r_{\text{in}}), \tag{11}$$

which diverges as $r_{\text{in}} \to 0$. A physical trait of superfluid helium prevents this from happening: it cannot sustain speeds which are greater than v_c, the critical velocity. Thus the superfluidity is destroyed below a core radius of $a \sim \hbar/mv_c$. This breakdown may be modeled by excising a disk of radius a around each vortex and by adding a constant core energy ϵ_c to account for the energy associated with the disruption of the superfluidity in the core.

Starting on the flat plane, the interaction of two vortices can now be determined. Superimposing the fields of the two vortices and integrating the cross term in the kinetic energy of Eq. (9) leads to a Coulomb-like interaction $V_{ij} = -2\pi K n_i n_j \ln|\mathbf{u}_i - \mathbf{u}_j|/a$ in addition to vortex self-energies. In deducing the force between the vortices from this expression, it is useful to assume that a does not vary significantly with position. The justification for this simplification is that the background flow due to other vortices only gives a fractionally small correction to the $1/r$ flow near each vortex, and therefore barely affects where the critical velocity is attained.

For the more complicated case of a *curved* surface, with a very distant boundary [see Vitelli and Nelson (2004) for the discussion of effects due to a boundary at a finite distance], Vitelli and Turner (2004) found that the energy of several vortices including both single-particle and two-particle interactions is

$$\frac{E(\{n_i, \mathbf{u}_i\})}{K} = \sum_{i<j} 4\pi^2 n_i n_j V_{ij}(\mathbf{u}_i, \mathbf{u}_j) + \sum_i [-\pi n_i^2 U_G(\mathbf{u}_i)]. \tag{12}$$

The braces indicate that E is a function of many variables, corresponding to all i's between 1 and N. Equation (12) omits only a position-independent term [given for a distant circular boundary of radius R by $\pi(\Sigma_i n_i)^2 \ln(R/a) + N\epsilon_c/K$, with ϵ_c the core energy of a vortex]. The pair potential $V_{ij} = \Gamma(\mathbf{u}_i, \mathbf{u}_j)$ is expressed in terms of Γ, and the Green's function of the covariant Laplacian is defined by

$$\nabla_u^2 \Gamma(\mathbf{u}, \mathbf{v}) = -\delta_c(\mathbf{u}, \mathbf{v}). \tag{13}$$

Note that the covariant delta function δ_c includes a factor of $1/\sqrt{g}$ so that its integral with respect to the "proper area" $\sqrt{g}du_1 du_2$ is normalized. Equation (13) determines the Green's function up to a constant, provided that we assume additionally that the Green's function is symmetric between its two arguments. The constant is fixed by assuming that at large separations the Green's function approaches the Green's function of an undeformed plane. This expression shows that vortices behave like electrostatic particles, with charges given by $2\pi n_i$ and coupling constant K.

The single-particle potential $U_G(\mathbf{u})$ is the "geometric potential" defined in Eq. (3). This potential entails a repulsion $\nabla \pi n^2 K U_G$ of vortices of either sign from positive curvature and an attraction to negative curvature. The interaction of a vortex (or an electrostatic charge) with a boundary likewise produces a force whose sign is independent of the vortex's sense of rotation. In the analogous problem in electrostatics, the attraction to a boundary for charges of both signs is ordinarily explained with the method of images, since a charge and its image always have the opposite sign. A more general point of view is that the flow pattern of the vortex (or the electrostatic field of the charge) has to be modified to satisfy the boundary conditions, changing the energy stored in the flow field. Likewise, the geometric potential arises because the equations of fluid mechanics are modified by curvature.

The modifications of fluid flow by either boundaries or curvature may be compared by analyzing the streamlines on the bump and in the presence of a circular boundary as shown in Fig. 2. Streamlines are tangent to the direction of flow and their density is proportional to the local speed. Only an incompressible velocity field (div $\mathbf{v} = 0$) may be described by streamlines, since incompressibility ensures that any closed curve has an equal number of streamlines entering and exiting. This condition is satisfied for superfluids (far below the critical speed) since minimizing Eq. (9) leads to $\nabla \cdot \nabla\theta = 0$, or div $\mathbf{v} = 0$ according to Eq. (7). Thus the flow is both irrotational (the circulation around any curve, not enclosing a vortex, is 0) and incompressible,

$$\text{div}\,\mathbf{v} = 0, \quad \text{curl}\,\mathbf{v} = 0. \tag{14}$$

The former relation implies that we may write

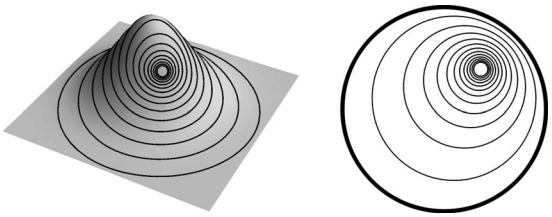

FIG. 2. A comparison between the forces on vortices due to curvature and due to boundaries. Left: the flow around a vortex situated on the side of a Gaussian bump, calculated with the methods described in this paper. The low density of flow lines above the vortex indicates a lower velocity and thus a higher pressure, leading to the repulsion represented in Eq. (12), $-\nabla(-\pi K n^2 U_G)$. Right: the analogous flow around a vortex in a disk with a solid boundary. The attraction to the boundary is also seen to result from high speeds, since the flow lines are compressed in between the vortex and the boundary.

$$\mathbf{v} = \text{curl}\ \chi\hat{\mathbf{n}} \tag{15}$$

so that the streamlines are equally spaced level curves of χ. [For example, around a vortex, the radii of the successive streamlines, indexed by the integer l, form a geometric sequence $a(1+\epsilon)^l$, where ϵ sets the ratio between flowline density and speed.]

Now consider the flow field on the slope of the bump represented in Fig. 2. The curves must spread out to go over the bump, leading to a lower velocity above the vortex. By Bernoulli's principle (true for irrotational flows), this creates a high pressure that pushes the vortex away from the bump. Note, however, that the actual motion of a vortex is more subtle: Although the gradient of the energy points away from the bump, a vortex (disregarding friction) always moves at right angles to the gradient of the energy. Thus a vortex in the absence of drag forces actually circles around the bump, in the same direction as the fluid flows around the vortex. Dissipation converts the motion into an outward spiral (Ambegaokar *et al.*, 1978). We will not study the dynamics.

A convenient mathematical formulation of the problem of determining the flow pattern of a collection of vortices is obtained by introducing the scalar function $\chi(\mathbf{u})$ which satisfies

$$\nabla^2\chi(\mathbf{u}) = -\sum_i 2\pi n_i \delta_c(\mathbf{u},\mathbf{u}_i) \equiv -\sigma(\mathbf{u}). \tag{16}$$

The sum can be described as a singular distribution of surface charge. This relation follows from the circulation condition, $2\pi n_i = \oint \nabla\theta\cdot\mathbf{dl}$, which can be rewritten as the integral of the flux of $\nabla\chi$ through the boundary, $\oint \nabla\chi\cdot\hat{\mathbf{n}}dl$, using Eq. (15). In analogy with Gauss's law, there must therefore be delta-function sources for χ at the locations of the vortices, as described by Eq. (16). Solving Eq. (16) in terms of the Green's function gives

$$\chi(\mathbf{u}) = \sum_i \frac{hn_i}{m}\Gamma(\mathbf{u},\mathbf{u}_i). \tag{17}$$

The flow due to a given vortex is proportional to its "charge" $2\pi n_i$. The energy as a function of the positions

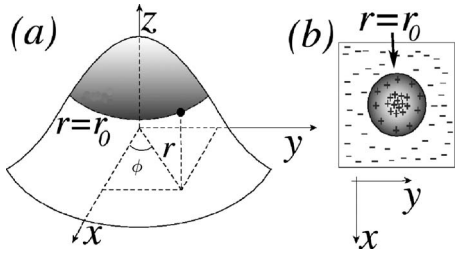

FIG. 3. Vortices on a Gaussian bump. (a) A bumpy surface shaped as a Gaussian. (b) Top view of (a) showing a schematic representation of the positive and negative intrinsic curvature as a nonuniform background "charge" distribution that switches sign at $r=r_0$. The varying density of + and − signs tries to mimic the changing curvature of the bump.

of the vortices, Eq. (12), can now be derived by integrating the kinetic energy in the flow determined by Eq. (16) for each placement of the vortices.

We begin by discussing applications of Eq. (12), saving its derivation until later (Sec. VI.A). Interestingly, the *energy* of the vortices can be described by a differential equation analogous to Eq. (16) for the *flow*. We choose one vortex and fix the positions of all others. We take the Laplacian of Eq. (12) with respect to the position of the chosen vortex and use Eqs. (3) and (13). The energy as a function of the chosen vortex $E(\mathbf{u}_i)$ satisfies

$$\nabla^2\frac{E(\mathbf{u}_i)}{2\pi K n_i} = -\sigma_i(\mathbf{u}_i) - \frac{n_i}{2}G(\mathbf{u}_i). \tag{18}$$

The notation σ_i stands for the delta-function charge distributions of all vortices with the exception of the ith, so that $\sigma_i(u) = \Sigma_{j,j\neq i} 2\pi n_j \delta(\mathbf{u}-\mathbf{x}_j)$. The self-charge term which we have had to remove in order to avoid an infinite right-hand side is replaced here by a spread-out charge. Like an image vortex on the other side of a boundary, this dispersed charge is proportional to vortex i's own charge.

A. Anomalous force on rotationally symmetric surfaces

On an azimuthally symmetric surface the force on a defect can be found by exploiting Gauss's law. This is analogous to the familiar "Newton's shell" theorem that predicts the gravitational field at the surface of a sphere surrounding a spherically symmetric mass distribution by concentrating all the enclosed mass at the center.

Points on an azimuthally symmetric two-dimensional surface embedded in three-dimensional Euclidean space are specified by a three-dimensional vector $\mathbf{R}(r,\phi)$ given by

$$\mathbf{R}(r,\phi) = \begin{pmatrix} r\cos\phi \\ r\sin\phi \\ h(r) \end{pmatrix}, \tag{19}$$

where r and ϕ are plane polar coordinates in the x-y plane of Fig. 3, and $h(r)$ is the height as a function of

radius; e.g., $h(r)=h_0e^{-r^2/2r_0^2}$ for the Gaussian bump with height h_0 and spatial extent $\sim r_0$.

It is useful to characterize the deviation of the bump from a plane in terms of a dimensionless aspect ratio

$$\alpha \equiv h_0/r_0. \tag{20}$$

The metric tensor $g_{\alpha\beta}$ is diagonal for this choice of coordinates. In general, $g_{\phi\phi}=r^2$, $g_{rr}=1+h'(r)^2$, and for the Gaussian bump we have

$$g_{\alpha\beta}=\begin{pmatrix} 1+\alpha^2\dfrac{r^2}{r_0^2}\exp\left(-\dfrac{r^2}{r_0^2}\right) & 0 \\ 0 & r^2 \end{pmatrix}. \tag{21}$$

Note that the $g_{\phi\phi}$ entry is equal to the flat space result r^2 in polar coordinates, while g_{rr} is modified in a way that depends on α but tends to the plane result $g_{rr}=1$ for both small and large r.

The Gaussian curvature for the bump is readily found from the eigenvalues of the second fundamental form (Dubrovin *et al.*, 1992), e.g., for the Gaussian bump,

$$G_\alpha(r)=\frac{\alpha^2e^{-r^2/r_0^2}}{r_0^2[1+(\alpha^2r^2/r_0^2)\exp(-r^2/r_0^2)]^2}\left(1-\frac{r^2}{r_0^2}\right). \tag{22}$$

Note that α controls the overall magnitude of $G(r)$ and that $G(r)$ changes sign at $r=r_0$ [see Fig. 3(b)]. The integrated Gaussian curvature inside a cup of radius r centered on the bump vanishes as $r\to\infty$. The positive Gaussian curvature enclosed within the radius r_0 (see Fig. 3) approaches 2π for $\alpha\gg 1$, half the integrated Gaussian curvature of a sphere. We show below that there is always more positive than negative curvature within any given radius, for an azimuthally symmetric surface. It will follow that the force on a vortex is repulsive at any distance.

In general a single vortex of index n confined on a curved surface at position $\mathbf{u}$ feels a geometric interaction described by the energy

$$E(\mathbf{u})=-\pi Kn^2U_G(\mathbf{u}). \tag{23}$$

When there are multiple vortices on a curved surface (as discussed after Sec. III.D), this same function describes the self-energy of each of them. For an azimuthally symmetric surface such as the bump represented in Fig. 3, we can derive Newton's theorem as follows. Define $\mathbf{E}=-\nabla U_G$ so that the covariant radial component of $\mathbf{E}$ is $E_r=-\partial_rU_G$. Then $-\nabla^2U_G=\mathrm{div}\,\mathbf{E}=(1/\sqrt{g})\partial_r\sqrt{g}g^{rr}E_r$, and if we integrate both sides of Eq. (3) out to r,

$$2\pi\sqrt{g}g^{rr}E_r=-\int\int\sqrt{g}drd\phi G(r) \tag{24}$$

so that E_r has a simple expression in terms of the net Gaussian curvature at a radius less than r. Now E_r is the "covariant component" of the geometrical "electric field," not the actual field, which would be obtained by differentiating with respect to arclength rather than the projected coordinate r. Therefore the magnitude of $\mathbf{E}$ is $E_r/\sqrt{g_{rr}}$, which, rephrasing Eq. (24), obeys this generalized version of Newton's theorem: The magnitude of $\mathbf{E}$ is $-1/2\pi r$ times the integrated Gaussian curvature. (Recall that $g^{rr}=1/g_{rr}$ and $g=\det g_{\alpha\beta}=r^2g_{rr}$.) Note that the force on the vortex is $\mathbf{F}=-\nabla E=-\pi Kn^2\mathbf{E}$ according to Eq. (23), so that the geometrical force is proportional to the integrated Gaussian curvature divided by the distance of the vortex from the axis of symmetry of the surface; the expression for the force on the vortex obtained in the next section by integrating the Gaussian curvature is

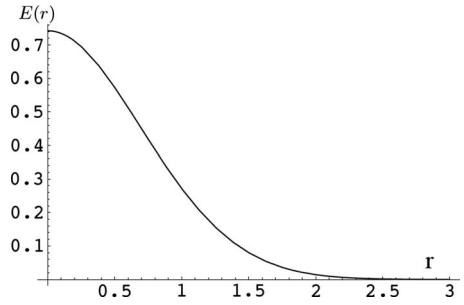

FIG. 4. Plot of the interaction energy $E(r)=-\pi KU_G(r)$ between a singly-quantized vortex and a Gaussian bump with $\alpha=1$. The energy is measured in units of K and the radius is measured in units of r_0. Note that the force points away from the bump and has its maximum strength near r_0.

$$F_{\mathrm{geom}}=\frac{K\pi}{r}\left(1-\frac{1}{\sqrt{1+h'^2}}\right), \tag{25}$$

if the vortex is singly quantized, i.e., $n=\pm 1$. Note that this force is always *repulsive* since the integrated curvature is positive.

The geometric potential can now be expressed explicitly by integrating $\mathbf{E}_r=-\partial_rU_G$ with the aid of Eq. (24),

$$U_G(r)=-\int_r^\infty dr'\frac{\sqrt{1+(\alpha^2r^2/r_0^2)\exp(-r^2/r_0^2)}-1}{r'}. \tag{26}$$

The resulting potential $U_G(r)$ vanishes at infinity. Its range and strength are given, respectively, by the linear size of the bump and its aspect ratio squared (see Fig. 4).

We now summarize an intuitive argument that explains why the energy of a vortex on top of the bump is greater than the energy of a vortex that is far away (Halperin, 2004; Vitelli and Turner, 2004). Figure 5 focuses on a rotationally symmetric bump coated by a helium film (of a constant thickness). We estimate the energy of a vortex on top of the bump by comparing the situation to a vortex on a plane, illustrated vertically below the bump. Rotational symmetry implies that the superfluid phase is given by $\theta=\phi$, the azimuthal angle. The velocity depends on the rate of change of the phase according to Eq. (7), so since an infinitesimal arc of the circle concentric with the top of the bump has size $rd\phi$, the velocity is $\hbar/mr$. Here r is the radius of the circle measured horizontally to the axis of the bump. This calculation shows that the velocity and thus the energy *density* are the same at any point on the bump and its projection into the plane. However, the energy contained in the tilted

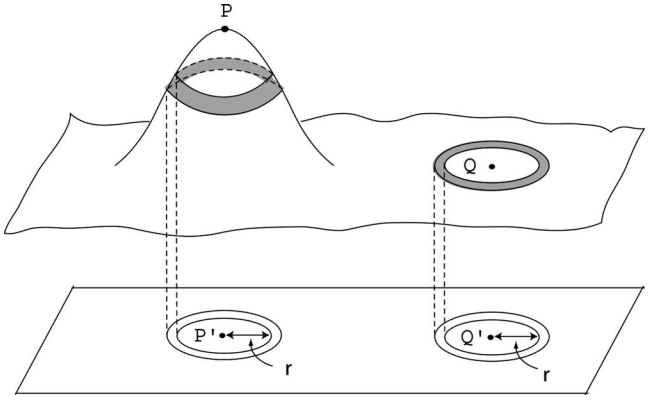

FIG. 5. An azimuthally symmetric substrate and its downward projection on a flat plane. The shaded strip surrounding P is more stretched than the one surrounding Q despite their projections onto the plane having the same area. As discussed in the text, it follows that the energy stored in the field will be lower if the center of the vortex is located at Q rather than P. From Vitelli and Turner, 2004.

annulus on the bump stretching from r to $r+dr$ is greater than the energy in the annulus directly below it because, though the energy *density* is the same, the annulus's area is greater. Hence a vortex on a bump has a greater energy than a vortex in a plane, whether it is the vortex at P' in the projection plane or the vortex at Q which is very far from the bump. This reasoning indicates a repulsive force, since the vortex lowers its energy by moving away from the bump.

The intuitive argument suggests that the Gaussian curvature should appear in the force law, as in Eq. (3); in fact, it is a widely known fact that the sign of the Gaussian curvature of a surface determines how fast the circumference of a circle on the surface increases, relative to the circumference of a circle on the plane, as a function of the radius.

Of course, this argument applies only for azimuthally symmetric surfaces. For less symmetric surfaces, comparing the energy on a curved surface to that on a flat reference plane directly below it will be more complicated, since symmetry and the constant circulation constraint do not force energy densities to be equal at corresponding postions. Thus, a simple vertical projection will not set up a monotonic relation between energies. The conformal-mapping technique which we use in Sec. VI is a variation on the idea of comparing a "target" substrate to a simple "reference" surface, which is in principle applicable to arbitrary surfaces, and furthermore not only allows one to compare energies, but also to calculate them quantitatively. The technique can also be used to give a concise derivation of Eq. (3).

B. Vortex-trapping surfaces

In order to illustrate the consequences of the curvature-induced interaction for different surface morphologies, we study a "Gaussian saddle" surface (suggested by Stuart Trugman) for which the geometric potential has its absolute minimum at the origin. First, we show that an alternative design for a vortex trap geometry fails because of the long-range nature of the curvature-induced interaction. Figure 3 shows that bumps have negative curvature on their flanks; it might seem possible that a well-chosen bump would have enough negative curvature to hold a vortex. However, a vortex cannot be held by nearby negative curvature alone; it also feels the positive curvature at the center of symmetry because, according to Gauss's law applied to the azimuthally symmetric region, the force is due to the *net* curvature contained in any circle concentric with the top of the bump. This curvature is given generally by

$$G = -\frac{1}{r\sqrt{1+h'(r)^2}}\partial_r\frac{1}{\sqrt{1+h'(r)^2}}, \tag{27}$$

and the net curvature within radius r_v is thus

$$\int_0^{r_v}\sqrt{g}drd\phi G(r) = 2\pi\left(1-\frac{1}{\sqrt{1+h'(r)^2}}\right)$$
$$= 2\pi(1-\cos\theta[r_v]), \tag{28}$$

where θ is the angle between the surface at the location of the vortex and the horizontal plane. This formula also describes the cone angle of a cone tangent to the surface at radius r_v; it can also be derived from the Gauss-Bonnet theorem, which implies that the net curvature of a curved region depends only on the boundary of the region and how it is embedded in a small strip containing it; thus the net curvature of the cone (concentrated at the sharp point of the cone) is the same as the net curvature of the bump to which it is tangent. Since this curvature is always positive, the defect is always repelled from the top of an azimuthally symmetric bump.[1] To find a way to trap a vortex, one must therefore investigate some nonsymmetric surfaces. The curvature-defect interaction energy on a generic surface is mediated by the Green's function of the surface, Eq. (13), as can be seen by solving Eq. (3),

$$E(\mathbf{u}) = K\pi\int d^2\mathbf{u}\Gamma(\mathbf{u},\mathbf{v})G(\mathbf{v}), \tag{29}$$

for a singly quantized vortex. One such surface, which we treat perturbatively in the amount of deformation from flatness (Sec. VI.B treats a different confining surface exactly), is the Gaussian saddle represented in Fig. 6 and described by the height function

$$h_\lambda(x,y) = \frac{\alpha}{r_0}(x^2-\lambda y^2)e^{-(x^2+y^2)/2r_0^2}, \tag{30}$$

where the exponential factor was included to make the surface flat away from the saddle (Trugman, 2004). Here

[1]Some surfaces may have an intrinsic geometry that is azimuthally symmetric, although they do not have any azimuthally symmetric *embeddings* in three-dimensional space. Such a surface can attract a vortex; an example is a negative curvature cone, as discussed in Sec. VII.

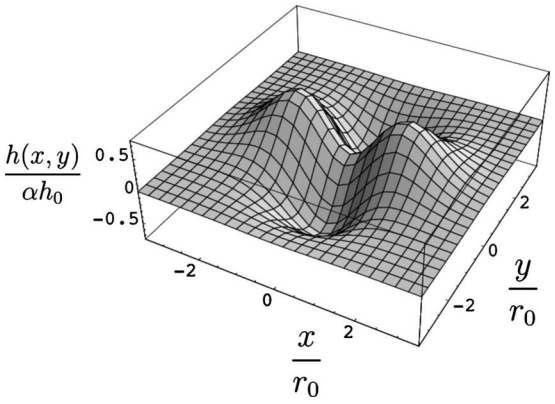

FIG. 6. Plot of vortex trapping surface.

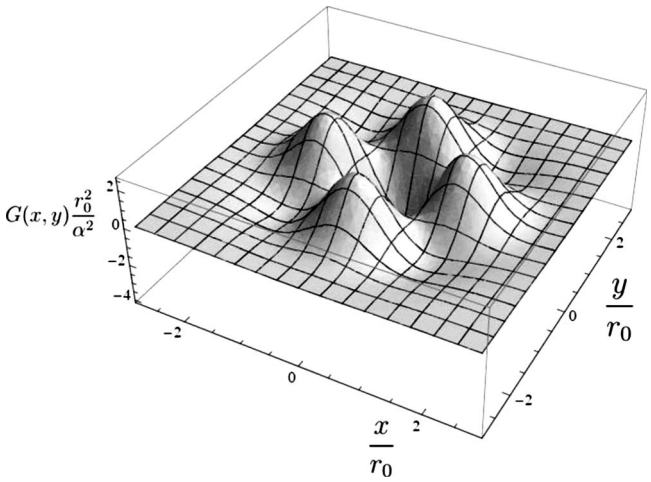

FIG. 7. Plot of the curvature of the $\lambda=1$ vortex trapping surface, measured in units of $(\alpha/r_0)^2$.

λ is a parameter which we later vary to illustrate the nonlocality of the interaction. The leading-order contribution to the curvature-defect interaction (for $\alpha \ll 1$) is of the same order α^2 as the curvature corrections to the defect-defect interaction (calculated in Appendix A). In fact Γ is multiplied in Eq. (29) by the Gaussian curvature $G(\mathbf{u}')$, of order α^2. Thus, the Green's function mediating interactions must be calculated to first order in the curvature, but for the interaction with the geometry the lowest order approximation is sufficient. For a single defect, it is sufficient to use the flat space Green's function Γ_{flat}:

$$\Gamma_{\text{flat}}(x-x',y-y') = -\frac{1}{2\pi}\ln\sqrt{(x-x')^2+(y-y')^2} \tag{31}$$

for calculating the defect-curvature interaction. Furthermore, the Gaussian curvature that acts as the source of the geometric potential can be calculated from the usual second-order approximation

$$G_\lambda(x,y) \approx \frac{\partial^2 h_\lambda}{\partial x^2}\frac{\partial^2 h_\lambda}{\partial y^2} - \left(\frac{\partial^2 h_\lambda}{\partial x \partial y}\right)^2. \tag{32}$$

This function is plotted in Fig. 7, and its sign is represented in the middle frame of Fig. 10.

The graph of the vortex-curvature interaction energy for this surface, Fig. 8, shows that a vortex is indeed confined at the center of the saddle; the energy graphed in Fig. 8 is given by

$$E_\lambda(x,y) \approx K\pi \int dx'dy' \Gamma_{\text{flat}}(x-x',y-y')G_\lambda(x',y'), \tag{33}$$

for $\lambda=1$. For realistic film thicknesses and α of order unity (see Sec. V), the depth of the well is about 50 K. We have found that the energy associated with a vortex at the origin is less than for any other position. Of course, the configuration with a vortex at the origin cannot beat the configuration with no vortices at all. The latter has zero kinetic energy; when the vortex is at the origin, the energy is positive provided that Eq. (12) is supplemented by the position-independent contribution $\pi K \ln(R/a)$. This term is always necessary for comparing configurations with different numbers of defects, as when one studies the formation of a vortex lattice at increasing rotational frequencies (Campbell and Ziff, 1979).

C. Negative curvature which does not trap

In this section, we discuss what happens when the parameter λ of the saddle surface is increased. Figure 9 shows such a surface corresponding to $\lambda=17$. To give a hint of what causes the equilibrium to change its character, Fig. 10 shows the sign of the curvature for the Gaussian bump, the saddle with $\lambda=1$, and the saddle with $\lambda=17$.

In the graph of the defect-curvature interaction energy with $\lambda=17$, one notices that the origin is an unstable equilibrium position for the vortex. We derive the exact value of λ where this instability first occurs below. However, symmetry considerations alone show that the origin is a stable equilibrium point when $\lambda=1$, as Fig. 8

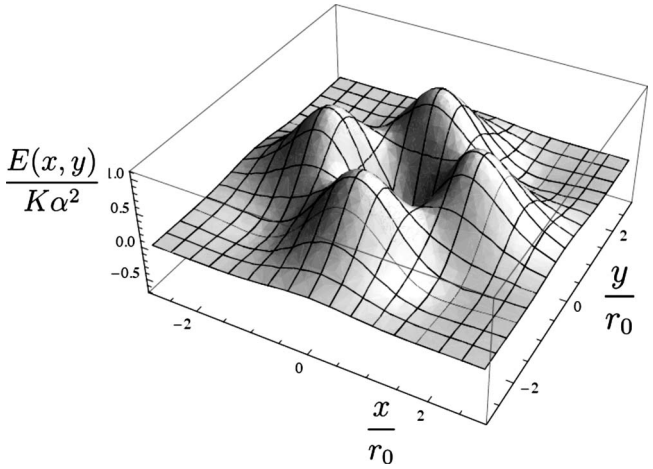

FIG. 8. Plot of the geometric potential for the $\lambda=1$ vortex trapping surface.

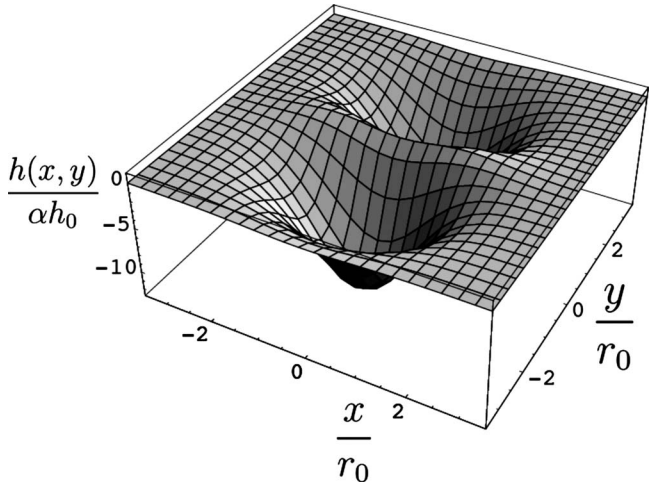

FIG. 9. A saddle surface with $\lambda=17$; this parameter value is just large enough to destabilize a vortex at the center.

shows. One might be tempted to argue from Newton's theorem that a vortex at a small enough radius r is always attracted to the origin by the negative curvature at radii smaller than r. However, the asymmetry of the saddle surfaces invalidates Newton's theorem and positive curvature more distant from the origin than the vortex might be able to push the vortex toward infinity. This does not occur for the saddle surface with $\lambda=1$ also because of symmetry; although the rotational symmetry needed for Newton's theorem is absent, the surface does have order four symmetry, under a 90° rotation combined with the isometry $z\to -z$.

Upon expanding the defect-curvature interaction energy about the origin, we obtain

$$E = E_0 + ax + by + cx^2 + 2dxy + ey^2 + \cdots . \tag{34}$$

This energy must be invariant under the symmetries of the surface (without a sign change). Order two symmetry implies that the linear terms vanish, so the center point is an equilibrium. Order four symmetry [apparent in Fig. 10(b)] implies that it is either a maximum or a minimum (a quadratic function with a saddle point has only 180° symmetry). In more detail, 90° rotational symmetry, given by $x\to y, y\to -x$, implies that $c=e, d=0$. Since the Laplacian of E at the origin is proportional to minus the *local* curvature, $2c=2e=c+e$ is positive, so the origin is a local minimum. Without order four symmetry the negative curvature only ensures that $c+e>0$.

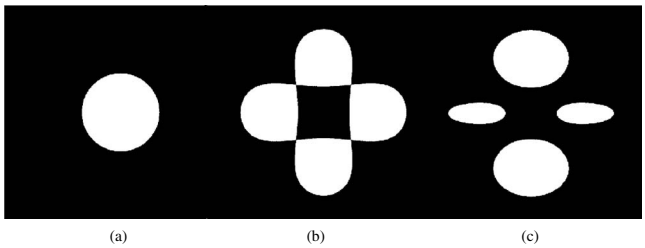

FIG. 10. Plots of the sign of the curvature, with white for positive curvature. (a) The Gaussian bump, and (b) and (c) the saddle surfaces with $\lambda=1$ and 17, respecitvely. Because of the lack of symmetry in (c), the center point becomes a saddle point of the energy; the vortex is pushed away by the strong positive curvature in the ellipsoidal regions at positive and negative y.

Earnshaw's theorem of electrostatics (Earnshaw, 1842; Jeans, 1927; Scott, 1959) states that an electric charge cannot have a stable equilibrium at a point where the charge density is zero or has the same sign as the charge. The charge cannot be confined by electric fields produced by electrostatic charge distributions in a surrounding apparatus. (This theorem motivated the design of magnetic and electrodynamic traps for trapping charged particles in plasma physics and atomic physics.) The argument provided here can be generalized to give the following converse rule based on discrete symmetries (whereas Newton's theorem applies only for continuous azimuthal symmetry): If P is a symmetry point of a charge distribution with rotation angle $2\pi/m$, and $m\geqslant 3$, and the charge density at P is positive, then P is a point of stable equilibrium for particles of negative charge.

This is the formulation for electrical charges in two dimensions; for vortices, the sense of the rotation of the vortex does not matter of course, since the geometric interaction is *quadratic* in the vortex strength. Hence if the curvature at P is negative, then a vortex will be trapped there.

Similar reasoning can be used to show that a generalization of Eq. (30), the "Gaussian monkey saddle" given by $h(x,y)=(\alpha/r_0^2)\Re(x-iy)^3 e^{-(x^2+y^2)/2r_0^2}$, traps vortices in an energy well of the form $E=E_0+(9\pi K/4)r^4/r_0^4+(\text{const}+\text{const}\times\cos 6\theta)r^6+\cdots$. The reasoning needs to be modified because the curvature at the origin of the monkey saddle is zero and the trapping is due to the negative curvature near the origin.

At a point of low symmetry [such as the origin in Eq. (30) when $\lambda\neq 1$], the character of an extremum depends on the charge distribution elsewhere, since the previous argument only implies that $c+e>0$. Figure 10(c) suggests that, when $\lambda=17$, a vortex at the origin is destabilized by its repulsion from the positive curvature above and below the origin, which is not balanced by enough positive curvature to the left and right. In fact, more detailed calculations show that the range of λ for which the origin is an energy minimum is $\sqrt{65}-8<\lambda<\sqrt{65}+8$; the origin is a saddle point outside this range, as is just barely visible for the case of $\lambda=17$ in Fig. 11. (Likewise, for negative values of λ, the origin is a maximum when $\sqrt{65}-8<-\lambda<\sqrt{65}+8$, but a saddle point outside this range.)

These results follow by changing the integration variables to $\xi=x-x'$, $\eta=y-y'$ in Eq. (33) and then expanding to second order about the origin $(x,y)=(0,0)$. The integral expressions for second derivatives of the energy can be evaluated explicitly,

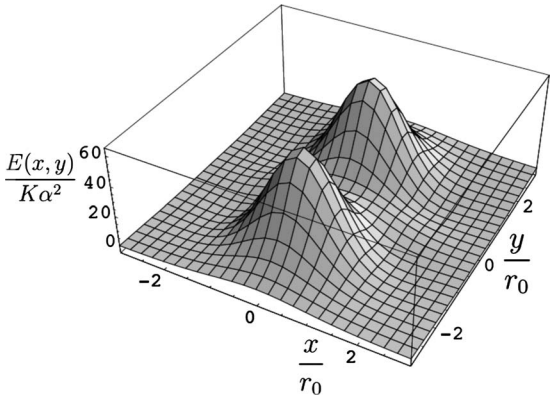

FIG. 11. The geometry-defect interaction energy of a vortex on the saddle surface with $\lambda=17$. One notices a slight instability in the x direction.

$$E_\lambda(x,y) = K\pi\left[\alpha^2\frac{1+\lambda^2-6\lambda}{16} + \frac{x^2}{4}\left(\alpha^2\frac{1-\lambda^2}{4r_0^2} - G_0\right) + \frac{y^2}{4}\left(\alpha^2\frac{\lambda^2-1}{4r_0^2} - G_0\right)\right], \tag{35}$$

where $G_0=-4\lambda\alpha^2/r_0^2$ is the curvature at the origin. In Appendix B, we determine the geometric potential for arbitrary x and y in (unwieldy) closed form.

D. Hysteresis of vortices and trapping strength

The geometrical interaction has its maximum strength when the Gaussian curvature is the strongest. However, the geometric charge (i.e., integrated Gaussian curvature) of any particular feature on a surface has a strength roughly equivalent at most to the charge of one or two vortices. Equation (25) therefore suggests that the force on a vortex due to a feature of the surface is not large; it is less than the force due to a couple vortices at the same distance. Precise limits on the strength of the geometric interaction will be stated and proven in Sec. VII, for arbitrary geometries.

As a consequence the geometric interaction has its most significant effects when the number of vortices is comparable to the number of bumps and saddles on the surface, so that the geometrical force is not obscured by interactions with the other vortices. This is a recurring (melancholy) theme of our calculations, to be illustrated in Sec. IV.D for arrangements of vortices in a rotating film. The current section illustrates the point by discussing hysteresis on a surface with multiple saddle points (i.e., traps). If a vortex-free superfluid film is heated, many vortices form in pairs of opposite signs. When it is cooled again, positive and negative vortices can remain trapped in metastable states in the saddles, but even with the strongest curvature possible the argument above suggests that not more than one vortex can be trapped per saddle.

The effectiveness of the defect trapping by geometry is determined mainly by the ratio of the saddle density to vortex density. As shown in the previous section, the geometric energy near the center of a vortex trap with 90° symmetry is given by

$$E(r) \approx \frac{\pi}{4}K|G_0|r^2. \tag{36}$$

The force on the vortex found by differentiating the energy reads

$$F(r) \approx -\frac{\pi}{2}K|G_0|r. \tag{37}$$

Equation (37) shows that the trap pulls the vortex more and more strongly as the vortex is pulled away from the center, like a spring, until the vortex reaches the end of the trap at a distance of the order of r_0 where the force starts decreasing. Since $G_0\sim\alpha^2/r_0^2$ (which is valid for a small aspect ratio α), the spring breaks down when the vortex is pulled with a force greater than

$$F_{\max} \sim F(r_0) \sim K\alpha^2/r_0 \sim \hbar^2\rho_s\alpha^2/m^2r_0, \tag{38}$$

where K is given by Eq. (10).

Consider a pair of saddles separated by distance d. It is possible that one vortex can be trapped in each saddle even for a small α provided that d is large enough. Remote vortices do not interact strongly enough to push one another out of their traps. The Coulomb attraction or repulsion of the vortices must be weaker than the breakdown force of the trap $F_{\max}$, i.e., $K\alpha^2/r_0 \gtrsim K/d$. The minimum distance between the two saddles is therefore

$$d_{\min} \sim r_0/\alpha^2. \tag{39}$$

Next consider the maximum density of trapped vortices that can remain when the helium film is cooled through the Kosterlitz-Thouless temperature. Suppose there is a lattice of saddles forming a bumpy texture. Suppose bumps cover the whole surface, so that the spacing between the saddles is of order r_0. Then not every saddle can trap a vortex; the largest density of saddles which trap vortices is of the order of $1/d_{\min}^2$, so the fraction of saddles which ultimately contain vortices is at most $r_0^2/d_{\min}^2 \propto \alpha^4$. Note that not as many vortices can be trapped if they all have the same sign, since the interactions from distant vortices add up producing a very large net force. On the other hand, producing vortices of both signs by heating and then cooling the helium film results in screened vortex interactions, which are weaker and hence less likely to push the defects out of the metastable states in which they are trapped.

IV. ROTATING SUPERFLUID FILMS ON A CORRUGATED SUBSTRATE

A. The effect of rotation

Suppose that the vessel containing the superfluid layer is rotated around the axis of symmetry of the Gaussian bump with angular velocity $\mathbf{\Omega}=\Omega\hat{\mathbf{z}}$. The container can rotate independently of the superfluid in it because

there is no friction between the two. However, a state with vanishing superfluid angular momentum is not the ground state. To see this, note that the energy $E_{\rm rot}$ in a frame rotating at angular velocity $\mathbf{\Omega}$ is given by

$$E_{\rm rot} = E - \mathbf{L}\cdot\mathbf{\Omega}, \tag{40}$$

where E is the energy in the laboratory frame and $\mathbf{L}$ is the angular momentum. Hence $E_{\rm rot}$ is lowered when $\mathbf{L}\cdot\mathbf{\Omega}>0$, that is, when the circulation in the superfluid is nonvanishing. This is achieved by introducing quantized vortices in the system [see Eq. (8)], whose microscopic core radius (of the order of a few angstroms) is made of normal rather than superfluid component. The energy of rotation $-\mathbf{L}\cdot\mathbf{\Omega}$ corresponding to a vortex of strength n at radius r_v on the bump can be evaluated from

$$L_z = \rho_s \int_S dxdy\sqrt{g(x,y)}(xv_y - yv_x). \tag{41}$$

Upon casting the integral in Eq. (41) in polar coordinates r,ϕ and using the identity

$$(xv_y - yv_x) = r\hat{\phi}\cdot\mathbf{v}, \tag{42}$$

we obtain

$$L_z = \rho_s \int_0^R dr\sqrt{g(r)}\oint_{C_r} du^\alpha v_\alpha, \tag{43}$$

where R is the size of the system. The loop integral in Eq. (43) is evaluated over circular contours of radius r centered at the origin of the bump. The circulation is equal to $n\kappa$ if the vortex is enclosed by the contour of radius r and vanishes otherwise,

$$\oint_{C_r} du^\alpha v_\alpha = n\kappa\Theta(r - r_v), \tag{44}$$

where Θ is the unit step function. Upon substituting into Eq. (43), we obtain

$$L_z = n\rho_s\kappa\int_{r_v}^R dr\sqrt{g(r)} = \frac{n\rho_s\kappa}{2\pi}[A(R) - A(r_v)], \tag{45}$$

where $A(R)$ is the total area spanned by the bump and $A(r_v)$ is the area of the cup of the bump bounded by the position of the vortex. Thus, after suppressing a constant, the rotation generates an approximately parabolic potential energy $E_\Omega(r)$ (see Fig. 13) that confines a vortex of positive index n close to the axis of rotation as in flat space:

$$E_\Omega(r_v) = n\frac{\hbar\Omega\rho_s}{m}A(r_v), \tag{46}$$

where a constant has been neglected. One recovers the flat space result (Vinen, 1969) by setting α equal to zero. Equation (45) has an appealing intuitive interpretation as the total number of superfluid atoms beyond the vortex $(\rho_s/m)[A(R)-A(r)]$ times a quantum of angular momentum $\hbar$ carried by each of them. The closer the vortex is to the axis, the more atoms there are rotating with the container.

Above a critical frequency Ω_1, the restoring force due to the rotation [the gradient of Eq. (46)] is greater than the attraction to the boundary. The energy of attraction to the boundary is $\sim\pi K\ln(1-r^2/R^2)$, where we assume the aspect ratio of the bump is small so that the flat space result is recovered. Upon expanding this boundary potential harmonically about the origin and comparing to Eq. (46), one sees that

$$\Omega_1 \sim \hbar/mR^2. \tag{47}$$

Above Ω_1, the origin is a local minimum in the energy function for a single vortex, though higher frequencies are necessary to produce the vortex in the first place. What determines the critical frequency for producing a vortex is unclear. There is a higher frequency Ω_1' $\sim(\hbar/mR^2)\ln(R/a)$ at which the single vortex actually has a lower energy [according to Eq. (45)] than no vortex at all, but critical speeds are rarely in agreement with the measured values (Vinen, 1963). In the context of thin layers, it is likely that a third, much larger critical speed $\Omega_{\rm crit}\sim\hbar/mRD_0$ is necessary before vortices form spontaneously, where D_0 is the thickness of the film.[2]

B. Single defect ground state

The equilibrium position of an isolated vortex far from the boundary is determined from the competition between the confining potential caused by the rotation and the geometric interaction that pushes the vortex away from the top of the bump. The energy of the vortex $E(r)$ as a function of its radial distance from the center of the bump is given up to a constant by the sum of the geometric potential and the potential due to rotation,

[2]This estimate follows if we assume that the critical speed is $v_c=(\hbar/mW)\ln(W/2a)$, where W is the shortest dimension of the chamber which is perpendicular to the flow of the normal fluid. The critical speed for a tall, narrow cylinder is determined by setting W equal to the radius R of the cylinder so $\Omega_c=v_c/R=(\hbar/mR^2)\ln(R/a)$, as seen by Yarmchuk and Packard (1982). For a thin film on a disk (a short, fat cylinder of fluid), the shortest dimension is the height, so $W=D_0$, giving $\Omega_c=\hbar/mRD_0$ apart from a logarithmic factor. That the critical velocity is determined by W follows from the remanent vorticity theory: At the critical speed, vortices are not created from scratch, but are believed to form by breaking away from pinned vortices (Glaberson and Donnelly, 1966); recently an experiment showed that the critical speed increases after pinned vortices are cleared away (Hashimoto *et al.*, 2007). The pinned vortices that are stretched across the shortest dimension can be stretched most easily by the passing current, causing a ring vortex of diameter W to twist off, expand until it hits container's walls and break into two line vortices with opposite circulations. The critical speed is the speed at which a ring vortex of size W would expand due to the Magnus force of the current passing through it rather than contracting due to its attraction for itself.

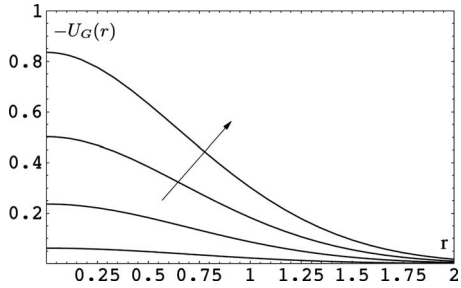

FIG. 12. Plot of minus the geometric potential $-U_G(r)$ for $\alpha=0.5,1,1.5,2$. The arrow indicates increasing α. The radial coordinate r is measured in units of λ and $r_0=\lambda$.

$$\frac{E(r)}{K} = -\pi U_G(r) + \frac{A(r)}{\lambda^2}, \tag{48}$$

where we have ignored the effects of the distant boundary; boundary effects are discussed in the next section. The "rotational length" λ is defined as

$$\lambda \equiv \sqrt{\hbar/m\Omega}. \tag{49}$$

A helium atom at radius λ from the origin rotating with the frequency of the substrate has a single quantum of angular momentum. The geometric contribution to $E(r)$ (see Fig. 12) varies strongly as the shape of the substrate is changed. The confining rotational contribution to $E(r)$ (see Fig. 13) varies predominantly as the frequency is changed; near the center of rotation, where the substrate is parallel to the horizontal plane, the rotational contribution barely changes as α is increased.

As one varies α (fixing r_0 and Ω) there is a transition to an asymmetric minimum. In fact, Fig. 14 reveals that for α greater than a critical value α_c, the total energy $E(r)$ assumes a "Mexican hat shape" whose minimum is offset from the top of the bump. The position of this minimum is found by taking a derivative of Eq. (48) with respect to r,

$$\pi\frac{dU_G}{dr} = \frac{1}{\lambda^2}\frac{dA}{dr}. \tag{50}$$

Now dA/dr can be shown to equal $2\pi r\sqrt{1+h'^2}$ by differentiating Eq. (45) and dU_G/dr, which is the same as $F_G\sqrt{1+h'^2}$, can be evaluated by substituting for F_G from

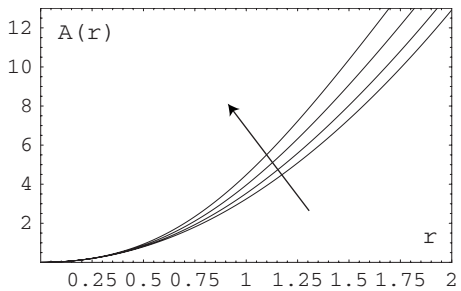

FIG. 13. Plot of the area of a cup of radius r for $\alpha=0.5,1,1.5,2$. The arrow indicates increasing α. The radial coordinate r is measured in units of λ and $r_0=\lambda$.

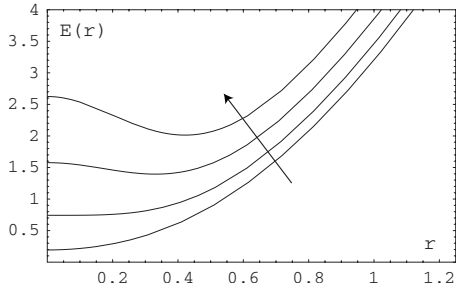

FIG. 14. Plot of $E(r)$ measured in units of $K=\hbar^2\rho_s/m^2$ as α is varied. In these units, the thermal energy k_BT is less than 0.02 below the Kosterlitz-Thouless transition, for 150-Å films. The radial coordinate r is measured in units of λ and $r_0=\lambda/2$. Note that this plot is a 2D slice of a 3D potential. For $\alpha<\alpha_c$, $E(r)$ is approximately a paraboloid while, for $\alpha>\alpha_c$, we have a Mexican hat potential.

Eq. (25). This leads to an implicit equation for the position of the minimum r_m, namely,

$$r_m/\lambda = \sin(\theta[r_m]/2). \tag{51}$$

Here $\theta(r)$, defined in Sec. III.B, is the angle that the tangent at r to the bump forms with a horizontal plane. A simple construction allows one to solve Eq. (51) graphically by finding the intercept(s) of the curve on the right-hand side with the straight line of slope $1/\lambda$ on the left-hand side (see Fig. 16). A calculation based on this construction shows that for $\alpha>\alpha_c=2r_0/\lambda$ there are two intercepts: one at $r=0$ (the maximum) and one at $r=r_m$, the minimum; whereas for $\alpha<\alpha_c$ only a minimum at $r=0$ exists exactly like in flat space.

It is possible to go through this second-order transition by changing other parameters such as the rotational frequency. See Figs. 14 and 15 for illustrations of how the transition occurs when the shape of the substrate is varied. More details on the choice of substrate parameters are given in Sec. V. Once these parameters have been chosen, changing the frequency would likely be more convenient; Fig. 16 shows how the equilibrium position of the vortex varies. If the vortex position r_m can

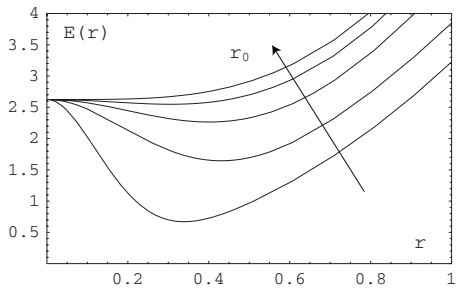

FIG. 15. Plot of $E(r)$ in units of $\hbar^2\rho_s/m^2$ vs r as r_0 is varied. The aspect ratio is kept fixed at $\alpha=2$ while the range of the geometric potential (corresponding to the width of the bump) is varied so that $r_0=0.2,0.4,0.6,0.8,1$ in units of λ. As r_0 decreases, the geometric force becomes stronger, so the system goes through a transition analogous to the one displayed in Fig. 14.

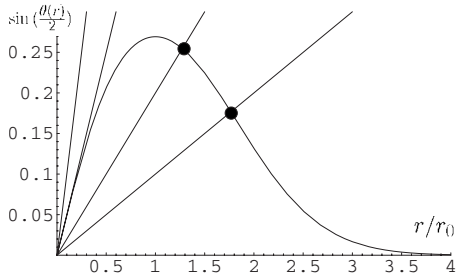

FIG. 16. Graphical method for determining equilibrium positions of one vortex. The equilibrium position is at the intersection of $\sin\theta(r)/2$ and r/λ. If we fix r_0 and set $\alpha=1$, the rotational frequency will control the position of the vortex. The four lines correspond to $\Omega=\hbar/mr_0^2, \hbar/4mr_0^2$ (which is the critical frequency Ω_c), $\hbar/25mr_0^2, \hbar/100mr_0^2$.

be measured precisely as a function of Ω and if there is not too much pinning, then the geometrical potential can even be reconstructed by integrating

$$U_G(r(\Omega)) = -\int_{\Omega}^{\Omega_c} 2\frac{m\Omega'}{\hbar} r_m(\Omega')\sqrt{1+h'[r_m(\Omega')]^2} \times \frac{dr_m}{d\Omega}(\Omega')d\Omega' + \text{const}$$

which follows from Eq. (50).

C. Multiple defect configurations

As the angular speed is raised, a cascade of transitions characterized by an increasing number of vortices occurs just as in flat space. The configurations vortices on a bump form illustrate how the geometric potential's importance is determined by the density of vortices (see Sec. III.D). In order to facilitate the mathematical analysis we introduce a conformal set of coordinates $\{\mathcal{R}(r), \phi\}$ [see Vitelli and Nelson (2004) for details]. The function $\mathcal{R}(r)$ corresponds to a nonlinear stretch of the radial coordinate that "flattens" the bump, leaving the points at the origin and infinity unchanged,

$$\mathcal{R}(r) = re^{U_G(r)}. \tag{52}$$

Note the unwanted appearance of the geometric potential $U_G(r)$ playing the role of the conformal scale factor; this surprise is the starting point for our derivation of the geometric interaction in Sec. VI.A. The free energy of N_v vortices on a bump bounded by a circular wall at distance R from its center is given by

$$\frac{E}{4\pi^2 K} = \frac{1}{2}\sum_{j\neq i}^{N_d} n_i n_j \Gamma^D(x_i;x_j) + \sum_{i=1}^{N_d}\frac{n_i^2}{4\pi}\ln[1-x_i^2] - \sum_{i=1}^{N_d}\frac{n_i^2}{4\pi}U_G(r_i) + \sum_{i=1}^{N_d}\frac{n_i^2}{4\pi}\ln\left[\frac{\mathcal{R}(R)}{a}\right]. \tag{53}$$

The Green's function expressed in scaled coordinates reads

$$\Gamma^D(t_i;t_j) = \frac{1}{4\pi}\ln\left(\frac{1+t_i^2t_j^2-2t_it_j\cos(\phi_i-\phi_j)}{t_i^2+t_j^2-2t_it_j\cos(\phi_i-\phi_j)}\right), \tag{54}$$

where ϕ_i is the usual polar angle and the dimensionless vortex position t_i is defined by

$$t_i \equiv \mathcal{R}(r_i)/\mathcal{R}(R). \tag{55}$$

Equation (53) is now cast in a form that is identical to the flat space expression apart from the third term which results from the curvature of the underlying substrate and vanishes when $\alpha=0$. However, we emphasize that the Green's function Γ^D also is modified by the curvature of the surface and thus depends on α.

The contributions from the second term and the numerator of the Green's functions in the first term account for the interaction of each vortex with its own image and with the images of the other vortices present on the bump [see Vitelli and Nelson (2004)]. If $R \gg r_0$, and all vortices are near the top of the bump (i.e., $r_i \sim r_0$), then these boundary effects may all be omitted when determining equilibrium positions, as the forces which they imply are on the order of Kr_0/R^2, small compared to the intervortex forces and geometric forces, which have a typical value of K/r_0.

Imagine rotating the superfluid, so that each vortex is confined by a potential of the form Eq. (46). In flat space, the locally stable configurations usually involve concentric rings of vortices (Campbell and Ziff, 1979). In particular, there are two stable configurations of six vortices. The lower-energy configuration has one vortex in the center and five in a pentagon surrounding it. The other configuration, six vortices in a hexagon, has a slightly higher energy, and Yarmchuk and Packard (1982) saw the configuration fluctuating randomly between the two, probably due to mechanical vibrations since thermal oscillations would not be strong enough to move the vortices. (The experiment used a $D_0=2$ cm high column of superfluid; if one regards the problem as two dimensional by considering flows that are homogeneous in the z direction, $\rho_s=D_0\rho_3$ is so large that $K=\hbar^2\rho_s/m^2$ is on the order of millions of degrees kelvin.) There are no other stable configurations. However, on the curved surface of a bump, there are several more configurations which can be found by numerically minimizing Eq. (53); the progression of patterns as α increases depends on how tightly confined the vortices are compared to the size of the bump, as shown in Fig. 17. If the vortices are tightly confined, the interactions of the vortices (which are different in curved space) stabilize the new vortex arrangements. If the vortices are spaced far apart, the geometric interaction is more important so it can push the central vortex away from the top of the bump as in the decentering transition in the previous section.

For example, if $\Omega=9\hbar^2/mr_0^2$, then at $\alpha=0$ the five off-center vortices start out in a ring of radius $0.6r_0$. This pentagonal arrangement (see frame A of Fig. 17) is locally stable for $\alpha<\alpha_1=2.7$. However, for $\alpha>\alpha_2=2.1$, another arrangement with less symmetry is also stable (see

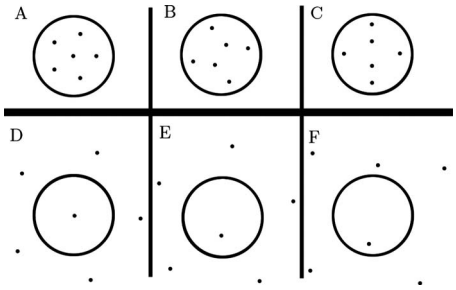

FIG. 17. Arrangements of six vortices that can occur on a curved surface, comparing tightly confined vortices (the top row) to more dispersed vortices (the bottom row). A circle of radius r_0 is drawn to give a sense of the size of the bump. The upper row shows the patterns which occur at large angular frequencies ($\Omega = 9\hbar^2/mr_0^2$). The transition from the pentagon to the rectangle with two interior points is discontinuous, and there is a range of aspect ratios $2.1 < \alpha < 2.7$, where both configurations are metastable. The third configuration is nearly degenerate with the second configuration. The lower row shows the configurations which occur for $\Omega = \hbar^2/mr_0^2$ as α increases. The first transition is continuous and caused by the central vortex's being repelled from the top by the geometric interaction. The third configuration is similar to the second large Ω configuration but the effect of the geometric repulsion is seen in its asymmetry.

frame B of Fig. 17), and above α_1 it takes over from the pentagon. For $\alpha_2 < \alpha < \alpha_1$, both arrangements are locally stable, with the asymmetric shape becoming energetically favored at some intermediate aspect ratio. (There is also a third arrangement which coexists with the less symmetric arrangement for the larger aspect ratios, seen in the frame C of Fig. 17.) These extra configurations are stabilized by the curvature. In the plane, the configuration labeled B, for example, is unstable, because the outer rectangle of vortices can rotate through angle ϵ, decreasing its interaction energy with the two interior vortices while keeping the rotational confinement energy constant. (That the interaction energy decreases can be demonstrated by expanding it in powers of ϵ.) Because the Green's functions are different on the curved surface (they do not depend solely on the distance between the vortices in the projected view shown), frames B and C are stabilized.

At lower rotational frequencies, the equilibria which occur are even less symmetric. For $\Omega = \hbar^2/mr_0^2$, the vortices form a pentagon of radius r_0 when the surface is flat. This pentagon is far enough away that it has a minor influence on the central vortex, which undergoes a transition similar to the one discussed in Sec. IV.B. At $\alpha_1' = 1.4$, the central vortex moves off-axis (the transition is continuous), causing only a slight deformation of the pentagon (see frame D of Fig. 17). As for the single vortex on a rotating bump, the geometric potential has pushed the central vortex away from the maximum, and the other vortices are far enough away that they are not influenced much. At higher aspect ratios, the figure distorts further, taking a shape similar to the one in Fig. 17, B which occurs for $\Omega = 9\hbar^2/mr_0^2$, but offset due to the geometric interaction. For these two rotational frequencies the hexagonal configuration is less stable than the pentagon; it will not take the place of the pentagon once the pentagon is destabilized. The hexagon is of course metastable for nearly flat surfaces.

D. Abrikosov lattice on a curved surface

As in Sec. III.D the geometric potential will have significant consequences only when the number of vortices near each geometrical feature such as a bump is of order unity. As an example, consider the triangular vortex lattice that forms at higher rotational frequencies ($\Omega \gg \hbar/mr_0^2$ is the criterion for a large number of vortices to reside on top of the Gaussian bump). In flat space, the vortex number density is approximately constant and equal to (Tilley and Tilley, 1990)

$$\nu(\mathbf{u}) = 4\pi m\Omega/\hbar = 2\Omega/\kappa. \tag{56}$$

At equilibrium, the force exerted on an arbitrary vortex as a result of the rotation exactly balances the force resulting from the interaction with the other vortices in the lattice and from the anomalous coupling to the Gaussian curvature. We can determine the distribution on a curved substrate by making the continuum approximation to Eq. (18). The sum of delta functions σ gets replaced by $2\pi\nu(r)$ and the self-charge subtraction can be neglected in the continuum approximation. The Gaussian curvature can be neglected because it is small compared to the large density of vortex charge. Upon applying Gauss's theorem to the vortex charge distribution in an analogous way to Sec. III.A, we find that the force on a vortex at radius r is given by

$$F_v = \frac{1}{r}\int_0^r 4\pi^2 K\nu(r')r'\sqrt{1+h'^2}dr', \tag{57}$$

while the rotational confinement force, obtained by differentiating Eq. (45), is

$$F_\Omega = -\rho_s(2\pi\hbar\Omega/m)r. \tag{58}$$

Balancing the two forces leads to an areal density of vortices,

$$\nu(r) = m\Omega/\pi\hbar\sqrt{1+h'^2}. \tag{59}$$

Equation (59) has a succinct geometric interpretation: the vortex density $\nu(r)$ arises from distributing the vortices on the bump so that the projection of this density on the x-y plane is uniform and equal to the flat space result. The superfluid tries to mimic a rigidly rotating curved body as much as possible, given that the flow must be irrotational outside of vortex cores as for the case of a rotating cylinder of helium (Tilley and Tilley, 1990). To check this, first notice that the approximate rigid rotation entails a flow speed of Ωr at points whose projected distance from the rotation axis is r. Hence, the circulation increases according to the quadratic law $\oint \mathbf{v}\cdot\mathbf{dl} = 2\pi\Omega r^2$. Since this quantity is proportional to the *projected* area of the surface out to radius r, the discretized version of such a distribution would consist of

vortices, each with circulation $\kappa=2\pi\hbar/m$, with a constant projected density $2\Omega/\kappa$ as in flat space. This result can be generalized with some effort to any surface rotated at a constant rate, whether the surface is symmetric or not.

The geometric force has to compete with interactions among the many vortices expected at high angular frequencies. More precisely, the maximum force at radius r_0 according to Eq. (25) is of order $K\pi/r_0$, while the force due to all vortices Eq. (57) is of order

$$K(2\pi)(\pi r_0^2)[2\pi\nu(0)]/2\pi r_0 = 2\pi^2 K r_0 \nu(0).$$

The last expression greatly exceeds $K\pi/r_0$, in the limit of high angular velocity. The geometrical repulsion leads to a small depletion of the vortex density of the order of one vortex in an area of order πr_0^2.

The vortex arrangements produced by rotation are reminiscent of Abrikosov lattices in a superconductor (Vinen, 1969). In fact, an analogy exists between a *thin film* of superconductor in a magnetic field and a rotating film of superfluid. A major difference between bulk superfluids and bulk superconductors is that the vortices in a bulk superconductor have an exponentially decaying interaction rather than a logarithmic one because of the magnetic field (produced by the vortex current) which screens the supercurrent. The analogy is more appropriate in a thin superconducting film, where the supercurrents (being confined to the film) produce a much weaker magnetic field. In fact, Abrikosov vortices in a superconducting film exhibit heliumlike unscreened logarithmic interactions out to length scales of order $\lambda' = \lambda_L^2/D$, where λ_L is the bulk London penetration depth and D is the film thickness [see Pearl (1964) and Nelson (2002b)]. Our results on helium superfluids without rotation therefore apply also to vortices in a curved superconducting layer in the absence of an *external* magnetic field. Curved superconducting layers in external magnetic fields can be understood as well by replacing the magnetic field by rotation of the superfluid. We now review the analogy between a container of superfluid helium rotating at angular speed $\mathbf{\Omega}$ and a superconductor in a magnetic field $\mathbf{H}$ (Vinen, 1969). Note that in Eq. (40) E is given by $\frac{1}{2}\rho_s\int\int d^2\mathbf{u}(\hbar^2/m^2)(\nabla\theta)^2$ and $\hbar\nabla\theta$ is the *momentum* in the rest frame $\mathbf{p}$, although we are working in the rotating frame (the frame in which a vortex lattice would be at rest). For helium, the momentum in the rest frame $\mathbf{p}$ is related to the momentum in the rotating frame $\mathbf{p}'$ by the "gauge" transformation

$$\mathbf{p} \to \mathbf{p}' + m\mathbf{r}\times\mathbf{\Omega}. \tag{60}$$

Similarly, in the case of a superconductor the momentum $\mathbf{p}$ in the absence of a magnetic field is related to the momentum $\mathbf{p}'$ in the presence of the field by the familiar relation (Tinkham, 1996)

$$\mathbf{p} \to \mathbf{p}' + (e/c)\mathbf{A}, \tag{61}$$

where $\mathbf{A}$ is the vector potential. Comparison of Eqs. (60) and (61) suggests a formal analogy between the two problems,

$$\mathbf{A} \leftrightarrow (mc/e)\mathbf{r}\times\mathbf{\Omega}. \tag{62}$$

Equation (61) establishes a correspondence between the angular velocity $\mathbf{\Omega}$ and the magnetic field $\mathbf{H}$ that allows us to convert most of the relations we derived for helium to the problem of a superconducting layer, with the identification

$$\mathbf{\Omega} \leftrightarrow (e/2mc)\mathbf{H}. \tag{63}$$

Of course, one should keep the external magnetic field small so that a dense Abrikosov lattice does not form, since (as for superfluids) when there are too many vortices, the curvature interaction is overcome by the vortex interactions.

V. EXPERIMENTAL CONSIDERATIONS

The two-dimensional theory of vortices described here can be used as a basis for studying an aspect of their interaction which is often hard to probe in the bulk. Vortices are extended objects such as curves connecting opposite boundaries, rings, or knots. A vortex interacts with itself and with its image generated by the boundary of the fluid. However, if the vortex is curved, such forces (the three-dimensional generalization of the geometric force) are usually dominated by a force which depends only on the local curvature of the vortex called the "local induction force." This force has a strength per unit length (Saffman, 1992) of

$$f_{\mathrm{LIA}} = \pi\frac{\hbar^2}{m^2}\rho_3\kappa\ln\frac{1}{\kappa a}, \tag{64}$$

where ρ_3 is the bulk superfluid density and κ is the curvature of the vortex at the point where this force acts. This force can dominate the long-range forces because of the core size appearing in the logarithm.

The nonlocal part of the self-interaction of a vortex is sometimes expected to modify a vortex's motion significantly (Ricca *et al.*, 1999; Barenghi *et al.*, 2006). Volumes of superfluid whose boundaries are parallel and at a small distance D_0 (i.e., thin films) provide an especially good setting for isolating the nonlocal-induction forces. In a constant-thickness film, the local induction force vanishes because the vortices crossing the superfluid will be *straight*. The remaining nonlocal interactions among vortices should all be captured by the two-dimensional theory described in this paper, once the two-dimensional superfluid density is defined by $\rho_s=\rho_3 D_0$.

In any realistic experiment, the boundaries of the film will not be perfectly parallel. In order to meet both boundaries at right angles, the vortices are forced to curve with curvature $\kappa\approx\nabla D/D_0$. There is then a relic of the local induction force in Eq. (64) which reads

$$F_{th} = -\frac{\pi\hbar^2}{m^2}\rho_s\frac{\nabla D}{D_0}\ln\frac{r_0}{a}, \tag{65}$$

where r_0 is the scale of the Gaussian curvature. Equivalently, this force can be derived from the fact that vortices are attracted to the thinnest portions of the film, to

minimize the length of their cores, where the kinetic energy is largest. Equation (65) can be derived heuristically by taking the gradient of the energy of a vortex. The small distance cutoff is given by the core of the vortex, whereas the long-distance one is given by the order of the radius of curvature of the surface. The choice of the latter is motivated by the fact that the gradient of the thickness of the film ∇D, induced by the curvature, vanishes when the surface flattens out at a distance from the indentation of the order of a few times of its radius of curvature.

A prospective experiment will need to ensure that the thickness of the film is uniform enough so that this force does not dominate over the geometric interaction in which we are interested. Comparing Eqs. (65) and (38) gives the condition $\pi(\nabla D/D_0)\ln(r_0/a) \lesssim \alpha^2/r_0$. Hence

$$\epsilon \lesssim \frac{\alpha^2}{\ln(r_0/a)}, \tag{66}$$

where ϵ is the relative variation in the film thickness,

$$\epsilon \equiv (D_t - D_0)/D_0. \tag{67}$$

D_t denotes the thickness on top of the bump and D_0 is the thickness far away so that $D_t - D_0 \sim r_0 \nabla D$.

An approximately uniform film of helium can form on a surface spontaneously with the help of the van der Waals force (de Gennes *et al.*, 2004). In experiments on helium films [see Sabisky and Anderson (1973)], a surface is exposed to helium gas at a pressure slightly below the pressure that is necessary to liquefy it. Within a certain distance of the surface, the van der Waals attraction of the gas's molecules to the surface is strong enough to convert the helium to a liquid (Andelman *et al.*, 1988). While this force alone would lead to a uniform film thickness, it must compete against gravity, which thickens the superfluid at lower portions of the substrate, and surface tension, which thickens the superfluid where the mean curvature of the substrate is negative. Both gravity and surface tension thin the film on hills and thicken it in valleys, but if the film is thin enough, the van der Waals force can keep the nonuniformity very small, as discussed next.

A. The van der Waals force and thickness variation

We now provide an estimate of the variation in the film thickness ϵ for a liquid layer which wets a bump and apply it to thin helium films. The wetting properties of very thin films ($\sim$100 Å) of dodecane on polymeric fibers of approximately cylindrical shape have been investigated by Quéré *et al.* (1989). For thick films on rough surfaces, an integrodifferential equation, which can be solved numerically, determines the films' profiles (Andelman *et al.*, 1988). Here we concentrate on a simplified local expression for the film thickness [similar to the Derjaguin approximation (Derjaguin, 1940)], taking advantage of the fact that a thin film on a solid substrate that is curved has a mean curvature approximately determined by the shape of the substrate. This contrasts with a large drop of water on a nonwetting surface that can change its shape by a large amount, adjusting its mean curvature to balance surface tension against gravity.

The van der Waals force, gravity, and surface tension generate distinct contributions to the total energy of the film. The corresponding generalized pressures p_i can be defined by measuring how each type of energy E_i decreases as the film thickens,

$$p_i = -\frac{1}{A_0}\frac{dE_i}{dD}, \tag{68}$$

where the thickness D is measured above a small area element of the substrate denoted by A_0.

The film thickness is determined by the following equilibrium condition:

$$p_{\mathrm{vdW}}(\mathbf{x}) + p_g(\mathbf{x}) + p_\gamma(\mathbf{x}) = (\mu_{\mathrm{liquid}} - \mu_{\mathrm{gas}})n_3. \tag{69}$$

The terms on the left-hand side of Eq. (69) are the generalized pressures corresponding to the van der Waals, gravitational, and surface energies. The right-hand side, which we denote by $-\Delta\mu$ for brevity, shows how the thickness of the film is regulated by the difference between the chemical potentials of the liquid and gas phases. (The factor n_3 represents the number density of liquid helium.)

The pressure generated by van der Waals interactions $p_{\mathrm{vdW}}(\mathbf{x})$, also called the "disjoining pressure," depends on the thickness $D(\mathbf{x})$ of the film at $\mathbf{x}$ (de Gennes *et al.*, 2004),

$$p_{\mathrm{vdW}}(\mathbf{x}) \approx \frac{-A_H}{6\pi D(\mathbf{x})^3}[1 - \tfrac{3}{2}H(\mathbf{x})D(\mathbf{x})], \tag{70}$$

where A_H is the Hamaker constant which is material dependent (de Gennes *et al.*, 2004). A simplified derivation of Eq. (70) is presented in Appendix C. Note that the second term in Eq. (70) arises because the surface bends away from the vapor molecules when $H>0$ as at the top of the bump. As a result, the nearby vapor molecules interact only with the very nearest atoms of the solid substrate. This effect is small if $D_0 \ll r_0$ and will be neglected in what follows.

The van der Waals pressure dominates over p_g and p_γ for very thin films. Hence the film thickness is given to leading order by neglecting p_g and p_γ in Eq. (69),

$$D_0 = \sqrt[3]{-A_H/6\pi(\Delta\mu)}. \tag{71}$$

This is also the exact thickness of the film far away from the bump where p_g and p_γ vanish. Note that a negative value of A_H is necessary for wetting, and, in this case, the equilibrium thickness increases with increasing $\Delta\mu$. The effects of surface tension and gravity can now be included as perturbations.

The pressure generated by the surface tension can be found by evaluating Eq. (68) with the energy $E_\gamma = \gamma A(D)$, where $A(D)$ is the area of a small patch of the liquid-vapor interface at a constant distance D from the

corresponding area of the solid surface $A_0(\mathbf{x})$. Upon using the geometric relation (Kamien, 2002)

$$A(D) = A_0[1 + 2H(\mathbf{x})D(\mathbf{x}) + G(\mathbf{x})D^2(\mathbf{x})], \tag{72}$$

we obtain the desired result

$$p_\gamma(\mathbf{x}) \approx -2\gamma H(\mathbf{x}), \tag{73}$$

where $H(\mathbf{x}) = \frac{1}{2}[\kappa_1(\mathbf{x}) + \kappa_2(\mathbf{x})]$ is the mean curvature of the substrate with the convention that the principle curvatures κ_1, κ_2 are positive when the surface curves away from the outward-pointing normal. Note that for a thin film the second term in Eq. (72) can be neglected.

The gravitational energy cost of thickening the film is just the work necessary to lift the helium out of the reservoir, so that

$$p_g(\mathbf{x}) \approx -\rho_3 g h(\mathbf{x}), \tag{74}$$

where $h=0$ corresponds to the surface of the reservoir.

Apart from the lengths r_0, h_0, and D_0 inherited from the geometry of the system, it is convenient to define three characteristic length scales δ, ϱ, and l_c, obtained by pairwise balancing each of the three pressures

$$\delta \equiv \sqrt{-A_H/6\pi\gamma},$$
$$\varrho \equiv \sqrt[4]{-A_H/6\pi\rho_3 g}, \tag{75}$$
$$l_c \equiv \sqrt{\gamma/\rho_3 g}.$$

The last relation in Eq. (75) defines the familiar capillary length below which surface tension dominates over gravity (Guyon *et al.*, 2001), while the first and the second give two additional length scales involving the disjoining pressure. For ^{4}He on CaF_2, $\delta \simeq 10$ Å, roughly one order of magnitude greater than for most liquids, $\varrho \simeq 0.7$ μm and $l_c \simeq 0.4$ mm. (Liquid ^{4}He on a CaF_2 surface has $A_H \approx -10^{-21}$ J, and has a liquid-vapor surface tension of 3×10^{-4} J/m^2.)

Upon substituting Eq. (71) into Eq. (69), we obtain an approximate relation between $D(\mathbf{x})$ and D_0,

$$\frac{D(\mathbf{x})}{D_0} \approx 1 - \frac{D_0^3}{3}\left(\frac{2H(\mathbf{x})}{\delta^2} + \frac{h(\mathbf{x})}{\varrho^4}\right), \tag{76}$$

applicable to thin films for which $D \ll r_0, h$.

Equation (76) can be evaluated at the top of the bump, where helium is shallowest and $D(\mathbf{x})$ attains the minimum value D_t. Supposing that $\alpha=1$, the bump height and its mean curvature at the top are given by r_0 and its inverse, respectively. Next, substitute D_t into Eq. (66). This leads to an upper bound that D_0 must satisfy for the geometric force to be stronger than the vortex attraction to the thinnest portion of the film,

$$D_0^3 \lesssim \frac{1}{(2/r_0\delta^2 + r_0/\varrho^4)\ln(r_0/a)}. \tag{77}$$

In order for the vortices to be easily observable, D_0 should be as large as possible, and the film can be made thickest (while retaining its approximate uniformity) if the substrate's size r_0 is chosen to maximize the right-hand side of Eq. (77). The maximum occurs at $r_0 \sim \sqrt{2} l_c$, where the surface tension and gravity have comparable effects on the thickness variation. For smaller bumps, surface tension plays the main role and for larger bumps, gravity is more important. Therefore, the upper bounds on the film thickness become very stringent in the opposing limits $r_0 \ll l_c$ and $r_0 \gg l_c$.

The optimal size r_0, of a Gaussian bump with $\alpha=1$, is therefore about $0=0.6$ mm, while the corresponding film thickness is 150 Å. Similar estimates apply to the saddle surface. Although such films are very thin, the geometrical force is still much stronger than random forces due to thermal energy. Upon setting $\rho_s = \rho_3 D_0 = 0.2$ g/cm^3 D_0, the characteristic energy associated with the geometric effects $K = \rho_s \hbar^2/m^2$ corresponds to a thermal energy $k_B T$ with $T \approx 40$ K. The geometric forces are strong enough to prevent the vortex from wandering out of the trap due to thermal Brownian motion except very close to the Kosterlitz-Thouless transition where ρ_s is depleted.

These considerations show that, in order to observe the effects of the geometrical force on helium vortices, one has to be able to observe vortices in a very thin film, and the substrate has to be smooth enough that the vortices do not become pinned.

VI. COMPLEX SURFACE MORPHOLOGIES

Up to this point, our discussion has been confined to rotationally symmetric surfaces and slightly deformed surfaces for which the electrostatic analogy and perturbation theory can be successfully employed to determine the geometric potential. To investigate geometric effects that arise for strong deformations and for surfaces with the topology of a sphere, we adopt a more versatile geometric approach based on the method of conformal mapping, often employed to solve complicated boundary problems in electromagnetism and fluid mechanics (Batchelor, 2001).

The conformal mapping approach also sheds light on the physical origin of the geometric potential. A concrete goal is to solve for the energetics (and the associated flows) of topological defects on a complicated substrate T, the target surface, whose metric tensor we denote by g_{Tab}. This is accomplished by means of a conformal map C that transforms the target surface into a reference surface R, with metric tensor g_{Rab}. The computational advantages result from choosing the conformal map so that R is a simple surface (e.g., an infinite flat plane, a flat disk, or a regular sphere) that preserves the topology of the target surface. Figure 18 represents a complicated planar domain denoted by T, which can be mapped conformally onto a simple annulus labeled by R. We introduce the basic concepts in the context of this simple planar problem before turning to the conformal mapping between target and reference surfaces which is represented schematically in Fig. 19. Such mappings can always be found in principle (David, 1989).

The conformal transformation will map the original

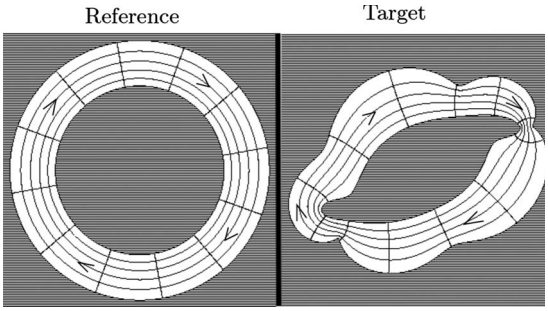

FIG. 18. The flow in a wiggly annular region (the target substrate T), obtained by conformally mapping the flow from a circular annulus (the reference substrate R). Since every pair of radial spokes in the first picture comprises the same energy, this is true in the conformal image as well. The small region in the constriction on the right manages this by compensating for its small area by having a high flow speed.

positions of the defects on T, denoted by $\mathbf{u}$, onto a new set of coordinates on R, denoted by $\mathcal{U}=C(\mathbf{u})$. In what follows, capital calligraphic fonts always indicate coordinates on the reference surface. For sufficiently small objects near a point $\mathbf{u}$ the map will act as a similarity transformation; that is, an infinitesimal length $ds_T = \sqrt{g_{Tab}du^a du^b}$ will be rescaled by a scale factor $e^{\omega(\mathbf{u})}$ which is independent of the orientation of the length on T,

$$ds_R = e^{\omega(\mathbf{u})} ds_T, \tag{78}$$

where $ds_R = \sqrt{g_{RAB}d\mathcal{U}^A d\mathcal{U}^B}$. This result in turn implies a simple relation between the metric tensors of the two surfaces,

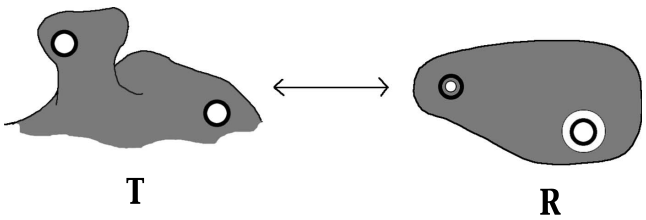

FIG. 19. Using conformal mapping to find the geometric energy of vortices on a complicated target surface T by comparison to a simple surface R. The target surface, left, has the topology of an infinite plane but is distorted by a three-dimensional lump. The reference plane R (shown in the plane of the page) is on the right. T is split up into portions I and O and different maps are used to map each to R. I consists of the interior of radius l disks (the circles in the figure with thick boundaries) in T, and is mapped *rigidly* to the heavily demarcated disks in R. O consists of the exterior of the disks in T (in gray), and is mapped *conformally* to the gray portion of R. I and O contain the same kinetic energy as their images in R, but the images do not fit together perfectly. Thus the difference in energy between the flows in T and in R is determined by calculating how much energy is contained in the annuli in R, which are either left bare or covered twice.

$$g_{RAB} = e^{2\omega(\mathbf{u})} g_{TAB}, \tag{79}$$

where we have assumed for simplicity that the coordinates used on the target surface are chosen so that corresponding points on the two surfaces have the same coordinates $\mathcal{U}^A$.

We demonstrate that, once the geometric quantity $\omega(\mathbf{u})$ is calculated, the geometric potential of an isolated vortex interacting with the curvature is automatically determined. For multiple vortices, the energy consists of single-vortex terms and vortex-vortex interactions. On a deformed sphere or plane, the geometric potential reads

$$E_1(\mathbf{u}_i) = -\pi n_i^2 K \omega(\mathbf{u}_i), \tag{80}$$

where K is the stiffness parameter defined in Eq. (10). For a deformed disk, there are boundary interactions not included in Eq. (80). (We will not consider multiply connected surfaces here, but the single-particle energy on a multiply connected surface has additional contributions which cannot be described by a local Poisson equation.) The interaction energy is

$$E_2(\mathbf{u}_i, \mathbf{u}_j) = -2\pi n_i n_j K \ln(\mathcal{D}_{ij}/a), \tag{81}$$

where $\mathcal{D}_{ij}$ is the distance between the two *image* points on the reference surface. When the reference surface is an undeformed sphere (the other possibilities are a plane or disk), $\mathcal{D}_{ij}$ is the distance between the points along a chord rather than a great circle (Lubensky and Prost, 1992). We show below that on a deformed plane ω is equal to U_G, but from now on we usually use ω instead; the two functions are conceptually different, and are equal only on an infinite deformed plane.

Equation (80) is derived by the method of conformal mapping in Sec. VI.A and its computational efficiency is illustrated in Sec. VI.B, where the geometric potential of a vortex is evaluated on an Enneper disk, a minimal surface that naturally arises in the context of soap films, but whose geometry is distorted enough compared to flat space that it cannot be analyzed with perturbation theory. This example also shows how to include the effects of boundary interactions. Changing the geometry of the substrate has interesting effects not only on the one-body geometric potential but also on the two-body interaction between vortices. In Sec. VI.C, we use conformal methods to show how a periodic lattice of bumps can cause the vortex interaction to become anisotropic. In Sec. VI.D, we demonstrate that the quantization of circulation leads to an extremely long-range force on an elongated surface with the topology of a sphere. The interaction energy is no longer logarithmic as in Eq. (81), but now grows linearly with the distance between the two vortices. Indeed the charge neutrality constraint imposed by the compact topology of a sphere blurs the distinction between geometric potential and vortex interaction drawn in Eqs. (80) and (81). This is most easily seen by bypassing vortex energetics on the reference surface (which is after all an auxiliary concept) and opting for a more direct restatement of the problem in terms of the Green's functions on the actual target sur-

face coated by the helium layer, which is valid for both distorted planes and spheres. The interaction energy now reads

$$E_2'(\mathbf{u}_i,\mathbf{u}_j) = 4\pi^2 K n_i n_j \Gamma(\mathbf{u}_i,\mathbf{u}_j), \tag{82}$$

and the single-particle energy takes the form of a self-energy

$$E_1'(\mathbf{u}_i) = -\pi n_i^2 K U_G(\mathbf{u}_i) = \pi n_i^2 K \int\int G(\mathbf{u}')\Gamma(\mathbf{u}_i,\mathbf{u}')d^2\mathbf{u}', \tag{83}$$

where Γ is a Green's function for the surface that generalizes the logarithmic potential familiar from two-dimensional electrostatics. For a deformed plane the two descriptions of the interaction energy are equivalent since the Green's function on a deformed plane can be obtained by conformal mapping,

$$\Gamma(\mathbf{u}_i,\mathbf{u}_j) = -\frac{1}{2\pi}\ln\frac{\mathcal{D}_{ij}}{a}. \tag{84}$$

We will see that the expressions for the single-particle energies are also equivalent. In contrast, for a deformed sphere, we show in Sec. VI.E and Appendix D that the two formulations do not agree term by term ($E_1' \neq E_1$ and $E_2' \neq E_2$), although the *combined* effect of one-particle and interaction terms is the same (up to an additive constant). Both self-energies and interaction energies include effects of the geometry and explicit formulas are provided on an azimuthally symmetric deformed sphere. Finally, in Sec. VII, we present a discussion of some general upper bounds to which the strength of geometric forces is subjected (even in the regime of strong deformations), which are useful in experimental estimates and which illustrate a major difference between electrostatic and geometric forces: The former can always be increased by piling-up physical charges but the latter are generated by the Gaussian curvature that can grow only at the price of "warping" the underlying geometry of space. Too much warping leads to either self-intersection of the surface or a dilution of the long-range force.

A. Derivation of the self-energy by conformal mapping

We start by proving a simple relationship between the total energies (including self-energy and interaction parts) E_T and E_R of two corresponding vortex configurations on the target and reference surfaces, respectively,

$$E_T = E_R - \pi K \sum_{i=1}^{N} \omega(\mathbf{u}_i). \tag{85}$$

The right-hand side of Eq. (85) can be calculated for the reference surface and then subsequently decomposed into single-vortex and vortex-vortex interactions; several examples are worked out in Secs. VI.B and VI.C.

The general approach is best illustrated by considering the planar flow in the complicated annular container shown in Fig. 18, which can be tackled by conformally mapping it to a simpler circular annulus.

The flow in the reference annulus is clearly circular, and it has the same $1/r$ dependence as for a vortex. A crucial property of conformal transformations allows us to transplant this understanding of the reference flow to the target annulus:

1. The conformal image of a physical flow pattern is still a physical pattern. This statement refers to a mapping of the stream function χ [see Eq. (15)] from the reference surface to the target surface,

$$\chi_T(\mathbf{u}) = \chi_R(\mathcal{U}), \tag{86}$$

where $\mathcal{U}$ and $\mathbf{u}$ are related by the coordinate change $\mathcal{U} = C(\mathbf{u})$. From the stream function $\chi_T(\mathbf{u})$ can be constructed a velocity field on the target surface. Visually, all we are doing is taking the streamlines on the reference surface, which are level curves of χ_R, and mapping them by C^{-1} to the target surface. The mathematical statement of property 1 is that the irrotational and incompressible properties of the flow which determine the velocity field (up to a factor) are invariant under conformal mapping (Needham, 2000).

Although any multiple $\alpha\chi_T(\mathbf{u})$ of the mapped stream function corresponds to an irrotational and incompressible flow, the circulation is not necessarily quantized correctly. Only the choice $\alpha=1$ ensures that both the target and reference flows have the same number n of circulation quanta around the hole (or around each vortex if some are present.) This follows from another basic property of conformal maps:

2. In flow patterns related by a conformal map circulation integrals around corresponding curves are the same. This property follows from the fact that the contribution to the circulation from each element of the contour, $\mathbf{v}\cdot\mathbf{dl}$, is conformally invariant. The infinitesimal length $\mathbf{dl}$ and the velocity $\mathbf{v}$ scale inversely to each other under conformal transformations and the angle between them is preserved by the map. To understand why, note that flow lines are compressed together (stretched apart) when they are mapped to the target space if the conformal parameter ω is greater (less) than zero. As a result, the velocity increases (decreases) by the same factor as distances are decreased (increased). This heuristic argument is confirmed by noting that the velocity is given by the *covariant* curl of the stream function, see Eqs. (15) and (86). By definition, the covariant curl carries a multiplicative factor of $g^{-1/2}=e^{\omega}$ (Dubrovin *et al.*, 1992), hence

$$v_T = e^{\omega} v_R. \tag{87}$$

On the other hand, $|\mathbf{dl}_T| = e^{-\omega}|\mathbf{dl}_R|$ rescales in the opposite way, as indicated in Eq. (78).

The problem of finding the *energy* in the deformed annulus can now be reduced to a simple rotationally symmetric problem by appealing to a third property of the conformal mapping:

3. The kinetic energies in corresponding regions are equal, provided the regions do not contain vortices. The proof of this statement relies on the previous discussion: the kinetic energy contained in an element of the area of the surface dA is $\frac{1}{2}\rho_s \mathbf{v}^2 dA$. By Eq. (87), $\mathbf{v}^2$ scales as $e^{2\omega}$ whereas dA scales by $e^{-2\omega}$, making the energy conformally invariant. Figure 18 shows pictorially that the energy density in the original flow on the target surface is smoothed out and simplified by the mapping to R, its variations being replaced by variations in the conformal scale factor.

We now return to the energetics of flows containing point vortices. The starting point of our analysis follows from the defining property of a conformal map, namely, that a conformal image of a small figure has the same shape as the original figure, while a larger shape becomes distorted (consider Greenland, which has an elongated shape, but appears to round out at the top in a Mercator projection, which is itself a conformal map). To quantify the size limits, note that if a shape has size l, ω changes by about $l\nabla\omega$ across the shape. Thus, as long as

$$l \ll 1/|\nabla\omega|, \tag{88}$$

the mapping rescales the shape uniformly. The right-hand side is ordinarily of order L, the curvature scale of the surface, since ω, being dimensionless, has a variation on the order of 1. As a result we can conclude with another property:

4. The circular shape of the streamlines near a microscopic vortex core on a substrate of slowly varying curvature is preserved. On a deformed substrate with a flow induced by vortices, the flow speeds will increase or decrease not just depending on the distance to the vortex, but also depending on the shape of the surface. For example, the vortex on top of the bump in the example of Sec. III.A has a flow that decays more slowly with distance than in flat space. For a vortex well off to the side of a bump, if the bump's height h is larger than its width $2r_0$, it turns out that the flow pattern penetrates only up to an elevation of about r_0 up the side of the bump.

The method of conformal mapping elucidates these geometrical rearrangements of the flow pattern. To find the flow pattern around the vortices at positions $\mathbf{u}_i$, we find the flow pattern around vortices at the corresponding positions $\mathcal{U}_i$ on the reference surface and then map these streamlines onto the target surface by Eq. (86). The energies are not equal in this case, in spite of property 3. Property 3 does not apply to a region containing vortex cores, because we would have to suppose the area of the cores on the reference surface to be greater by $e^{2\omega}$ and the energy in the cores to be smaller by a factor of $e^{2\omega}$, in order for the conformal relation equation $\frac{1}{2}\rho_s v_T^2 dA_T = \frac{1}{2}\rho_s v_R^2 dA_R$ to continue to hold. In contrast, the core radius is fixed by the short-distance correlations of the helium atoms and the core energy is related to the interaction energy of the atoms.

The vortex cores are not significantly affected by the curvature of the substrate; moreover, the whole flow pattern in the vicinity of the core is nearly independent of the location of a vortex. We observe that each vortex has a "dominion," a region where the flows are forced by the presence of the vortex to be

$$v = n\hbar/mr + \delta v. \tag{89}$$

The leading term has the same form as one expects for a vortex in a rotationally symmetric situation, and the effects of geometry are accounted for by δv; by dimensional analysis, this error is of the order of $\hbar/mL$, where L is the radius of curvature of the substrate (or possibly the distance to another vortex or to the boundary, whichever is shortest). Therefore we can introduce any length $l \ll L$ and note that l is then a distance below which the effects of curvature do not have a significant effect (compared to the diverging velocity field). The geometry correction gives a contribution to the energy within this radius that is also small, as seen by integrating the kinetic energy over the annulus between a and l [using Eq. (89)],

$$\pi K \ln(l/a) + \epsilon_c + O(K) l^2/L^2, \tag{90}$$

where a is the core radius and ϵ_c the core energy. The error term is *quadratic* in l/L because the integral over the cross term from squaring Eq. (89) cancels.

When we wish to find the kinetic energy of the superflow, these near-vortex regions are thus the simplest to account for, as their energy is nearly independent of their positions relative to features such as bumps on the substrate as long as

$$l \ll L. \tag{91}$$

Since the target and reference configurations have the same number N of vortices, the energies contained within radius l of the vortices are the same,

$$E^T_{<l} = E^R_{<l} = \pi N K \ln(l/\tilde{a}). \tag{92}$$

In order to find the forces on a set of vortices, we need to account for all the energy of the vortices in regions away from the vortices where the flow has been affected by the curvature. Imagine cutting the target surface up into an inner region I (the union of the radius l disks around each vortex) and an outer region O (consisting of everything else) as shown in Fig. 19. We can map I to the reference surface by simply translating each of the disks so that they surround the vortices on R. The modifications to the flow are all in O; for example, vortices' streamlines there are deformed from their circular shape. These irregularities can be removed (or at least simplified) using the conformal mapping to map O to R, just as in the case of the annulus illustrated above. The inhomogeneity of the conformal map compensates for the irregularity of the flow. Some portions of O are expanded and some are contracted, but its circular boundaries are small enough [see Eqs. (91) and (88)] that they are simply rescaled into circles of different radii (property 4),

$$l_i = e^{\omega(\mathbf{u}_i)} l. \tag{93}$$

Now we have mapped I and O from the target surface to regions on the reference surface which contain the same energy. But these images of the regions on R do not fit together. The conformal map on O stretches or contracts each hole in it, to circles of radii $e^{\omega(\mathbf{u}_i)}l$. These stretched edges (corresponding to the solid black circle in Fig. 19) do not fit together with the images of O, which have been moved rigidly from the target surface. The energies are related by

$$E_T = E^T_{<l} + E^T_{>l} = E^R_{<l} + E^R_{>l_i}. \tag{94}$$

We must correct for the gaps and overlaps between the two image regions on R in order to relate the last expression to E_R. If $\omega(\mathbf{u}_i) > 0$, there is an annular gap near vortex i; using Eq. (89) the energy omitted due to this gap (where the flow is controlled by the vortex) is

$$\Delta E_i = -\frac{1}{2}\rho_s \int_l^{l_i} 2\pi r dr \frac{n_i^2 \hbar^2}{m^2 r^2}, \tag{95}$$

$$\Delta E_i = -\pi K n_i^2 \omega(\mathbf{u}_i), \tag{96}$$

where Eq. (93) is used to evaluate the integral. Summing all these contributions gives our desired result, Eq. (85).

We emphasize that the energy difference is not produced within the cores, or anywhere near the vortices. The fact that the energies on T and R differ is a result of assuming that there is *no change* in the flow within a macroscopic distance l of the vortex. The scale $l \ll L$ only has to be small compared to the geometry of the system and has no relation to the atomic structure of the core. On the other hand, taking l as small as possible has an elegant consequence: Equation (85) actually has an error which is $O(K(a/L)^2)$, smaller than $O(K(l/L)^2)$ as predicted at first. Taking smaller values of l gives a more accurate result, since the conformal mapping [which does not suffer from the error in Eq. (90)] is used to calculate the energy of a larger portion of the flow pattern.

Equation (85) shows that the position-dependent scale factor $\omega(\mathbf{u})$ plays the role of a single-particle energy. Now we relate this single-particle energy to the geometric potential. In fact, for a deformed plane $\omega(\mathbf{u})$ is the same as the geometric potential defined in Eq. (3). To see this, note that $\omega(\mathbf{u})$ is related to the curvature in a way analogous to how the electrostatic potential is related to a charge distribution. The function ω depends on the shape of the boundaries and on the curvature of the surface. A varying scale factor is necessary to map between surfaces with different distributions of curvature (such as planes with and without bumps). (A constant scale factor only rescales the curvature.) The curvature therefore depends on the *variation* of ω. In fact, for any pair of target and reference surfaces,[3]

$$G_T(u,v) = e^{2\omega(u,v)} G_R(U(u,v), V(u,v)) + \frac{1}{\sqrt{\det(g_{T,cd})}} \partial_a \sqrt{\det(g_{T,cd})}\, g_T^{ab} \partial_b \omega, \tag{97}$$

where G_T and G_R label the Gaussian curvatures of the target and reference surface. The second term is the Laplacian of ω, considered as a function on the *target* surface, $\nabla_T^2 \omega = g_T^{ab} \nabla_{Ta} \nabla_{Tb} \omega$. On a deformed plane, it follows that the single-particle energy $\omega(u,v)$ is truly the "electrostatic potential" for the source $G_T(u,v)$, namely, $U_G(u,v)$ [from Eq. (3)]. [Note that $\omega(u,v)$ has the correct limit, 0, at infinity.]

For a deformed sphere or plane, the first term in Eq. (85) gives rise to the interaction, Eq. (81). For a single vortex, the reference energy E_R corresponding to vortices on a sphere or plane cannot favor one position over another, because of the homogeneity of these reference surfaces. This term therefore describes the vortex-vortex interactions which depend only on the separation of the vortices on the reference surface, again by symmetry; this energy is given by

$$E_R = 4\pi^2 K \sum_{i<j} n_i n_j \Gamma(\mathcal{U}_i, \mathcal{U}_j), \tag{98}$$

where Γ depends on the reference surface

$$\Gamma_{\text{plane}}(\mathcal{X}, \mathcal{Y}) = -\frac{1}{2\pi} \ln \frac{|\mathcal{X} - \mathcal{Y}|}{a} \tag{99}$$

and

$$\Gamma_{\text{sphere}}(\mathcal{X}, \mathcal{Y}) = -\frac{1}{2\pi} \ln \frac{2R \sin\frac{\gamma}{2}}{a} \tag{100}$$

$$= -\frac{1}{2\pi} \ln \frac{|\mathcal{X} - \mathcal{Y}|}{a}, \tag{101}$$

where γ is the angle between the two points. ($2R \sin \gamma/2$ is the *chordal* distance between the points, not the geodesic distance along the surface, as one might have guessed for the natural generalization of a Green's function to curved space.) The conformal factor ω is not equal to U_G on a deformed sphere because Eq. (97), with $G_R = 1/R^2$, reduces to a nonlinear equation

$$\nabla^2 \omega(u,v) = G_T(u,v) - e^{2\omega(u,v)}/R^2, \tag{102}$$

whereas $U_G(\mathbf{u})$ satisfies the ordinary Poisson equation. Nevertheless, the expressions for the vortex energies using the Green's functions [see Eqs. (82) and (83)] are equivalent to the conformal mapping expressions [Eqs.

[3]As a check of this identity, imagine reversing the roles of the reference and target surfaces. Then ω should be regarded as a function on the reference surface. This changes the Laplacian by a factor of $e^{2\omega}$ (because g_R is replaced by g_T). Also, the sign of ω should be reversed. Rearranging the equation now brings it back into the original form with T and R switched.

(80) and (81)] just derived. These results are illustrated in Sec. VI.E and they are derived in Appendix D. In contrast, on a deformed disk, U_G and ω both satisfy the Poisson equation, but still do not coincide because they do not satisfy the same boundary conditions. This discrepancy is illustrated in Sec. VI.B.

B. Vortices on a "soap film" surface

There are experimental and theoretical motivations for studying substrates shaped as minimal surfaces. An example of a minimal surface is easy to make by dipping a loop of wire in soap; the spanning soap film tries to minimize its area. Vortices can be studied on a helium film coating a *solid* substrate whose surface has the shape of such a film. Such surfaces are characterized by a vanishing mean curvature $H(\mathbf{x})$ so the contribution of the surface tension $2\gamma H(\mathbf{x})$ to the thickness-variation equation Eq. (69) is drastically reduced. From the mathematical point of view, there is a widely known parametrization due to Weierstrass (Hyde *et al.*, 1997), which readily leads to an *exact* expression for the geometric potential of a vortex on such a surface.

Weierstrass's formulas, which give a minimal surface for each choice of an analytic function $R(\zeta)$, read

$$x(\zeta) = \mathrm{Re}\int_0^\zeta R(\zeta')(\zeta'^2 - 1)d\zeta',$$

$$y(\zeta) = \mathrm{Im}\int_0^\zeta R(\zeta')(\zeta'^2 + 1)d\zeta', \tag{103}$$

$$z(\zeta) = \mathrm{Re}\int_0^\zeta R(\zeta')2\zeta' d\zeta'.$$

The correspondence between this parametric surface and the complex variable $\zeta = \mathcal{X} + i\mathcal{Y}$ is a conformal map, and the conformal factor can be expressed in terms of $R(\zeta)$. Therefore, the analysis of vortices on such a surface is not difficult at all when the $\mathcal{X}$-$\mathcal{Y}$ plane is used as the reference surface.

As an example, let $R(\zeta)$ be equal to $L\zeta$ where L controls the size of the target surface. Then the surface produced is given in parametric form by

$$x = L[\mathcal{X}^3/3 - \mathcal{X}\mathcal{Y}^2 - \mathcal{X}],$$

$$y = L[-\mathcal{Y}^3/3 + \mathcal{Y}\mathcal{X}^2 + \mathcal{Y}], \tag{104}$$

$$z = L(\mathcal{X}^2 - \mathcal{Y}^2).$$

We consider a superfluid film coating only a circle of radius A about the origin of the $\mathcal{X}$-$\mathcal{Y}$ plane because the complete surface has self-intersections. This surface can be called the Enneper disk and is shown in Fig. 20. The figure illustrates that the left- and right-hand sides of the saddle fold over it and would pass through each other if allowed to extend further while the front and the back would eventually intersect each other underneath the saddle. The former pair of intersection curves correspond to the two branches of the hyperbola $\mathcal{X}^2 = 3(\mathcal{Y}^2 + 1)$. When the reference surface is curved into the Enneper surface, the X axis bends upward so that both branches map to the same curve in the y-z plane. (The other intersection curves are obtained by exchanging $\mathcal{X}$ and $\mathcal{Y}$.) Since the points where these hyperbolas are closest to the origin are $(\pm\sqrt{3}, 0)$, $(0, \pm\sqrt{3})$, a non-self-intersecting portion of the Enneper surface results as long as $A < \sqrt{3}$.

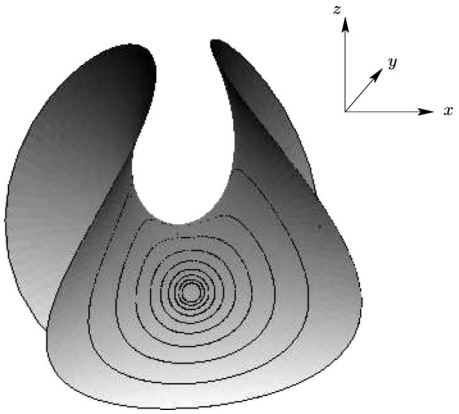

FIG. 20. Vortex and its streamlines on an "Enneper disk."

Now we explicitly calculate how a single vortex interacts with the curvature of such a surface using Eq. (85). [We use conformal mapping instead of Eq. (29) since the latter equation does not hold on a surface with the topology of a disk, as ω does not satisfy the Dirichlet boundary conditions which are implied by such an expression.] The metric obtained from Eq. (104) is given by

$$dx^2 + dy^2 + dz^2 = L^2(d\mathcal{X}^2 + d\mathcal{Y}^2)(1 + \mathcal{X}^2 + \mathcal{Y}^2)^2. \tag{105}$$

(Surprisingly, this *metric* is rotationally symmetric in the $\mathcal{X}\mathcal{Y}$ plane. This implies that the surface may be slid along itself without stretching, but with changing amounts of bending.) Hence

$$\omega_{\mathrm{Enneper}} = -\ln L(1 + \mathcal{R}^2), \tag{106}$$

where $\mathcal{R}^2 = \mathcal{X}^2 + \mathcal{Y}^2$. According to Eq. (85), this indicates that the vortex should be attracted to the middle of the surface, but of course this force competes with the boundary interaction $K\pi \ln[(A^2 - \mathcal{R}^2)/aA]$ which tries to pull the vortex to the edge. This expression for the boundary interaction is obtained from the familiar formula for the energy of a vortex interacting with its image in a flat reference disk (Vitelli and Nelson, 2004). The total energy is then

$$E = K\left[\pi \ln\frac{L}{aA} + \pi \ln(A^2 - \mathcal{R}^2)(1 + \mathcal{R}^2)\right]. \tag{107}$$

As long as $A > 1$, the central point of the saddle is a local minimum and this condition is compatible with the requirement $A < \sqrt{3}$ for non-self-intersecting disks. Figure 20 shows the flow lines of a vortex forced by the geo-

metric interactions towards the center of an Enneper surface with $A=1.5$.

In general, conformal mapping allows us to express the energy of a single vortex on a deformed surface with a boundary in the form

$$E = \pi K\left[-\omega(\mathbf{u}) + \ln\frac{A^2 - \mathcal{R}(\mathbf{u})^2}{aA}\right], \tag{108}$$

where $\mathcal{R}(\mathbf{u})$ refers to the image of a defect at $\mathbf{u}$ under a conformal map to a flat circular disk of radius A. The Green's function method cannot be used to determine the energy of defects on a surface with a boundary. Although the conformal factor $\omega(\mathbf{u})$ satisfies the Poisson equation, Eq. (3), it cannot be expressed as the integral of the curvature times the Green's function [as in Eq. (83)], since ω does not satisfy simple boundary conditions. In any case, the first term in Eq. (108) has no general expression in terms of ω either. Interestingly, the total single-particle energy satisfies a *nonlinear* differential equation (the Liouville equation),

$$\nabla^2_{\mathbf{u}} E(\mathbf{u}) = -\pi K G(\mathbf{u}) - (4\pi K/a^2)e^{-2E(\mathbf{u})/\pi K}. \tag{109}$$

This result can be derived by using Eq. (97) to calculate the Laplacian of the first term and using $\nabla^2 = e^{2\omega(\mathbf{u})}(1/\mathcal{R})(\partial/\partial\mathcal{R})\mathcal{R}(\partial/\partial\mathcal{R})$ to calculate the Laplacian of the second term. $E(\mathbf{u})$ also satisfies an asymptotic boundary condition

$$e^{E(\mathbf{u})/\pi K} \to 2d/a \tag{110}$$

as d, the distance from $\mathbf{u}$ to the boundary, approaches 0. This condition demands that the energy of a vortex near any boundary approach the energy of a vortex in an uncurved half-plane. (Since the flow of a vortex near a boundary extends over only a small region, the curvature of the boundary and the Gaussian curvature do not matter.) Together the differential equation and the boundary condition should determine the total geometrical and boundary energy of a single vortex, although the nonlinear equation (109) is difficult to solve.

C. Periodic surfaces

In this section, we illustrate how a periodically curved substrate distorts the flat space interaction energies between vortices, besides generating the single-particle geometric potential. This effect is shown to be a consequence of the action of a conformal map which generally will map the target surface into a reference substrate that is also periodic but has a lattice that is sheared relative to the actual substrate's. According to the general relation (84), the long-distance behavior of the Green's function is given by the logarithm of a distorted distance.

Consider a surface with a periodic height function $z = h(x,y)$, i.e., say h satisfies

$$h(x+\lambda_i, y+\mu_i) = h(x,y) \quad \text{for } i=\{1,2\}, \tag{111}$$

where i labels the two basis vectors, which are not assumed to be orthogonal. Figure 21 shows the corresponding periods (λ_i,μ_i). A conformal mapping can be chosen to preserve the fact that the substrate is periodic but not the actual values of the periods, which are therefore given on the reference substrate by two new pairs denoted by (Λ_i,M_i). In other words, we suppose that a tessellation of the target substrate by congruent unit cells is mapped to a set of congruent unit cells on the reference substrate. Then the map transforming the original coordinates (x,y) into the target coordinates $(\mathcal{X},\mathcal{Y})$ satisfies

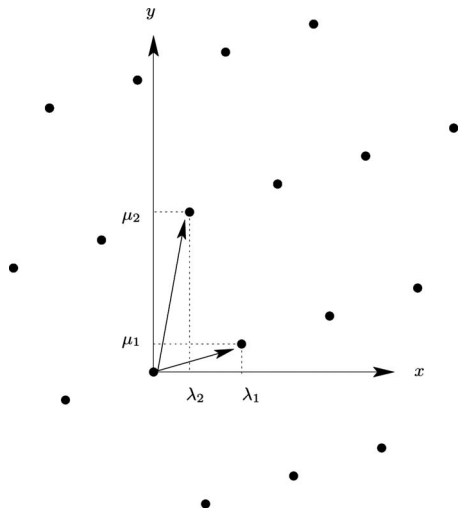

FIG. 21. An illustration of the period lattice of the target surface, projected into the x-y plane. The coordinates λ_1,μ_1 and λ_2,μ_2 describe the basis vectors, which we do not assume to be orthogonal.

$$\begin{aligned}\mathcal{X}(x+\lambda_i, y+\mu_i) &= \mathcal{X}(x,y) + \Lambda_i,\\ \mathcal{Y}(x+\lambda_i, y+\mu_i) &= \mathcal{Y}(x,y) + M_i.\end{aligned} \tag{112}$$

There is no simple formula for the new set of primitive lattice vectors (Λ_i,M_i) for the reference space. In some cases, though, precise information can be derived from the fact that (Λ_i,M_i) share the symmetry of the topography of the original substrate. For example, if the lattice is composed of bumps which have a 90° rotational point symmetry, then the reference lattice will be square. On the other hand, the topology of the periodic surface with a square lattice shown in the contour plot of Fig. 22 does not possess a 90° rotational symmetry and hence its conformal image will have a rectangular lattice.

To get an idea how the conformal mapping behaves macroscopically, we try to decompose it into a linear transformation $\mathcal{L}$ with matrix coefficients $\{A,B;C,D\}$ and a periodic modulation captured by the functions $\xi(x,y)$ and $\eta(x,y)$ that distort the $\mathcal{X}$ and $\mathcal{Y}$ axes, respectively,

$$\begin{aligned}\mathcal{X}(x,y) &= Ax + By + \xi(x,y),\\ \mathcal{Y}(x,y) &= Cx + Dy + \eta(x,y).\end{aligned} \tag{113}$$

(This decomposition is justified by the self-consistency of the following calculations.) The matrix coefficients of

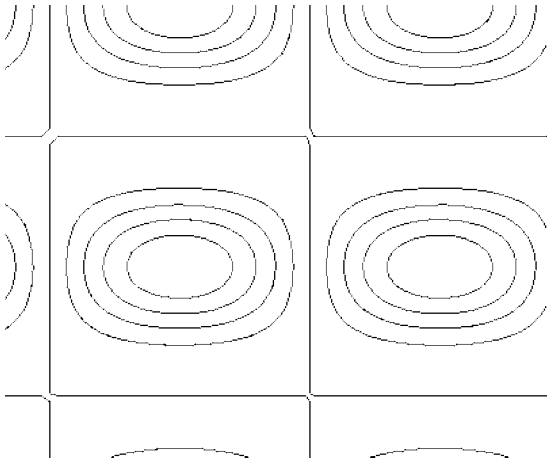

FIG. 22. A periodic surface with a square lattice but not square symmetry. This surface is illustrated by its contour plot. It has the two reflectional symmetries but not the 90° symmetry of a square lattice; hence, generically, the conformal image will have a rectangular lattice.

the linear transformation can be determined by requiring consistency with Eq. (112). Start by evaluating the left-hand sides of Eqs. (113) at the positions $\{x+\lambda_i, y+\mu_i\}$, and apply Eq. (112) to the left-hand side. Then subtract the resulting equations from the corresponding unshifted Eqs. (113), for each value of i. We then obtain two pairs of equations

$$A\lambda_i + B\mu_i = \Lambda_i,$$
$$C\lambda_i + D\mu_i = M_i \quad \text{for } i = \{1,2\}, \tag{114}$$

where we have used the fact that the periodic functions $\xi(x,y)$ and $\eta(x,y)$ are unchanged when shifted by the periods. We can now solve the four equations of Eqs. (114) simultaneously for A, B, C, and D to see that the linear transformation matrix $\mathcal{L}$ reads

$$\mathcal{L} = \begin{pmatrix} A & B \\ C & D \end{pmatrix} = \begin{pmatrix} \Lambda_1 & \Lambda_2 \\ M_1 & M_2 \end{pmatrix} \begin{pmatrix} \lambda_1 & \lambda_2 \\ \mu_1 & \mu_2 \end{pmatrix}^{-1}. \tag{115}$$

[Now we can justify the original decomposition, Eq. (113), by defining $\mathcal{L}$ by Eq. (115) and defining $\xi(x,y)$ and $\eta(x,y)$ as the discrepancy between the conformal map $\mathcal{X}(x,y), \mathcal{Y}(x,y)$ and the linear map $\mathcal{L}(x,y)$ as in Eq. (113). We can then check that $\xi(x,y)$ and $\eta(x,y)$ are periodic functions of the coordinates.]

The linear transformation can be used to calculate approximately the long-distance behavior of the Green's function

$$\begin{aligned} \Gamma(x,y;x',y') &= -\frac{1}{4\pi} \ln[(\Delta\mathcal{X})^2 + (\Delta\mathcal{Y})^2] \\ &\approx -\frac{1}{4\pi} \ln[(A\Delta x + B\Delta y)^2 \\ &\quad + (C\Delta x + D\Delta y)^2], \end{aligned} \tag{116}$$

where we used the fact that the periodic functions $\xi(x,y)$ and $\eta(x,y)$ are bounded and hence negligible in comparison to Δx and Δy at long distances. This expression illustrates the fact that the matrix $\mathcal{L}$ captures the long-distance lattice distortions induced by the conformal mapping, apart from the additional waviness described by $\xi(x,y)$ and $\eta(x,y)$. The linear transformation determined by $\mathcal{L}$ is by itself typically *not conformal*, meaning that it generates an anisotropic deformation of the target lattice which does not preserve the angle between the original lattice vectors. The full map is conformal for small shapes on the surface of the substrate.

The deformation of the lattice is controlled by the curvature of the substrate. To spell out this connection and allow an explicit evaluation of the long-distance Green's function in Eq. (116), we explicitly evaluate the matrix elements L_{ij} in terms of the height function $h(x,y)$ of a gently curved (or low-aspect-ratio) surface, one for which $h(x,y) \ll \{\lambda_i, \mu_i\}$, in which case $\{\xi(x,y), \eta(x,y)\} \ll 1$, and $\{A-1, D-1, B, C\} \ll 1$. The new set of (isothermal) coordinates $\mathcal{X}$ and $\mathcal{Y}$, used to implement the conformal transformation, are found by solving the Cauchy-Riemann equations (A3),

$$\partial_x \mathcal{X} = \sqrt{g} g^{yy} \partial_y \mathcal{Y} + \sqrt{g} g^{xy} \partial_x \mathcal{Y},$$
$$\partial_y \mathcal{X} = -\sqrt{g} g^{xx} \partial_x \mathcal{Y} - \sqrt{g} g^{xy} \partial_y \mathcal{Y},$$

which, upon substituting from Eq. (113) and making the small-aspect-ratio approximation discussed in Appendix A, reduce to

$$A + \partial_x \xi = D + \partial_y \eta + \tfrac{1}{2}(h_x^2 - h_y^2), \tag{117}$$

$$B + \partial_y \xi = -C - \partial_x \eta + h_x h_y. \tag{118}$$

We now proceed to show that these equations do not have solutions unless the lattice is distorted; that is to say, the matrix $\mathcal{L}$ cannot be the identity for a generic periodic function $h(x,y)$. Note that the periodicity of $\xi(x,y)$ and $\eta(x,y)$ implies that the integral of either one over any unit cell, e.g.,

$$\int\int_{\text{cell}} dx dy \xi(a+x, b+y) \tag{119}$$

is independent of the quantities (a,b) by which the unit cell is shifted. Upon differentiating the integral with respect to a, one obtains

$$\int\int_{\text{cell}} dx dy \xi_x(x,y) = 0. \tag{120}$$

Similarly, the averages of η_x, η_y, and ξ_y are also equal to zero. Hence, upon averaging Eq. (118) over a unit cell we obtain the key relations

$$A - D = \tfrac{1}{2}\langle h_x^2 - h_y^2 \rangle,$$
$$B + C = \langle h_x h_y \rangle, \tag{121}$$

which prove our assertion that $\mathcal{L}$ cannot be a simple dilation or rotation. Some shear is naturally introduced by the nontrivial metric (or height function) of the underlying surface.

The $\mathcal{L}$ matrix is undetermined up to a dilation and a rotation but this is of no consequence to the determination of the Green's function. In fact, to find the Green's function, note that Eq. (121) allows us to write the matrix coefficients in terms of two undetermined constants ϵ_1 and ϵ_2 that will drop out of the final answer,

$$A = 1 + \epsilon_1 + \tfrac{1}{4}\langle h_x^2 - h_y^2\rangle, \tag{122}$$

$$D = 1 + \epsilon_1 + \tfrac{1}{4}\langle h_y^2 - h_x^2\rangle, \tag{123}$$

$$B = \epsilon_2 + \tfrac{1}{2}\langle h_x h_y\rangle, \tag{124}$$

$$C = -\epsilon_2 + \tfrac{1}{2}\langle h_x h_y\rangle, \tag{125}$$

so that consistency with Eqs. (121) is guaranteed. [The variables ϵ_1 and ϵ_2 parametrize an overall infinitesimal scaling (by $1+\epsilon_1$) and a rotation (by angle ϵ_2), respectively.] Substitution of these equations into Eq. (116) gives the desired long-distance behavior of the Green's function purely in terms of derivatives of the height function, which we assume to be known,

$$\Gamma(x,y;x',y') \approx -\frac{1}{4\pi}\ln\{\Delta x^2 + \Delta y^2 + \tfrac{1}{2}\langle h_x^2 - h_y^2\rangle[(\Delta x)^2 - (\Delta y)^2] + 2\langle h_x h_y\rangle \Delta x \Delta y\}. \tag{126}$$

This is the central result of this section; it can also be applied to interactions between disclinations in liquid crystals (Vitelli and Nelson, 2004) and dislocations in crystals (Vitelli *et al.*, 2006). The anisotropic correction to the Green's function, captured by the second and third terms, suggests that a distorted version of the triangular lattice of vortices expected on a flat substrate may form when the helium-coated surface is rotated slowly enough that there is only one vortex to several unit cells. However, the actual ground state is likely to be difficult to observe, as the geometric potential will try to trap the vortices near saddles as discussed in Sec. III.B.

D. Band flows on elongated surfaces

In this section, we show that the quantization of circulation can induce an extremely long-range force on a stretched-out sphere (such as the surface of a very prolate spheroid). We first demonstrate the main result in the context of a simple example before presenting a general formula for the forces experienced by vortices on azimuthally symmetric surfaces. Details are presented in Appendix E. Consider a cylinder of length $2H$ and radius $R \ll H$ with hemispherical caps of radius R at the ends, shown in Fig. 23, and imagine a symmetric arrangement of a vortex ($n=1$) and an antivortex ($n=-1$) at the north and south poles, respectively.

Extrapolating our intuition from flat space suggests that the energy of the vortex and antivortex is $2\pi K \ln(D/a)$, where D is the distance between the vortices. However, more careful reasoning shows that the energy grows *linearly* rather than logarithmically with D.

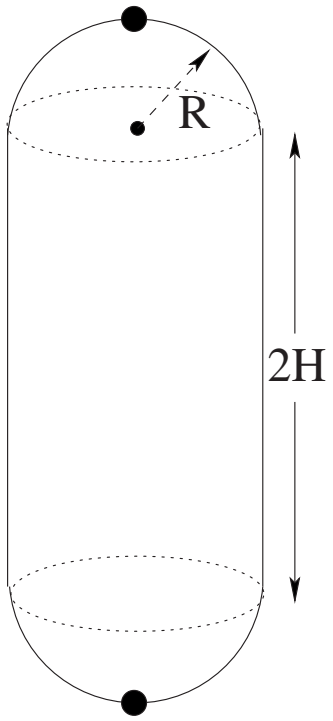

FIG. 23. A capped cylinder; a cylinder of length $2H$ is closed off by hemispheres at the north and south poles of radius R. The circulation around every lattitude is the same.

The reason is that, unlike in flat space, the velocity field does not fall off like the inverse of the distance from each vortex. Note that the azimuthal symmetry of the arrangement of the vortices implies that the flow is parallel to the lines of latitude of the surface. Since the circulation around each latitude must be h/m, the flow speed on the cylindrical part reads

$$v = h/2\pi m R. \tag{127}$$

The kinetic energy of this part of the flow is $[4\pi RH]\frac{1}{2}\rho_s v^2 = 2\pi KH/R$. Since this cylindrical part of the flow forms the main contribution to the kinetic energy when $H \gg R$, we find that the energy of a vortex-antivortex pair situated at opposite poles is linear,

$$E_{\text{poles}} \approx 2\pi KH/R. \tag{128}$$

[The exact expression also includes a near-vortex energy of approximately $2\pi K \ln(R/a)$.]

In contrast, when the vortices forming the neutral pair are across from each other on the same latitude, the aforementioned long-range persistence of the velocity field is absent because the vorticity is screened within a distance of order R. The resulting kinetic energy follows the familiar logarithmic growth

$$E_{\text{equator}} \approx 2\pi K \ln(2R/a). \tag{129}$$

More generally, consider an azimuthally symmetric surface described by the radial distance $r(z)$ as a function of height z, as shown in Fig. 24(a). If the north and south poles of the surface are at z_s and z_n, then $r(z_s) = r(z_n) = 0$ since the surface closes at the top and bottom.

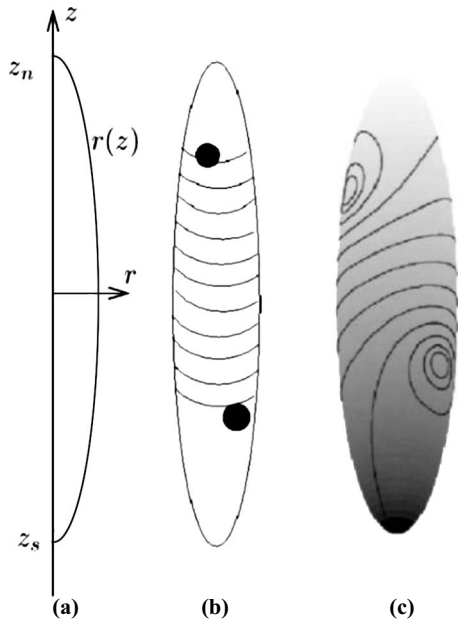

FIG. 24. The flow on an azimuthally symmetric surface, described by the coordinates (z,r) and an azimuthal angle ϕ (not shown). (a) The surface is defined as the surface of revolution of the curve $r(z)$ in the r-z plane. The other two images show the flow on an ellipsoid and compare the flow pattern predicted by the band model (b) and the exact solution determined by conformal mapping (c). The flow lines in the band between the two vortices become close to horizontal and are approximately azimuthally symmetric. Beyond the vortices, they are spaced far apart, indicating a vanishingly small speed for a greatly elongated surface.

A point on such a surface can be identified by the coordinates (ϕ,σ), where ϕ is the azimuthal angle and σ is the distance to the point from the north pole along one of the longitudes such as the one shown in Fig. 24(a).

In Appendix E, we develop an approximation scheme which shows that the flow pattern becomes mostly azimuthally symmetric if $dr/dz \ll 1$, even if the vortices break the azimuthal symmetry of the surface because they are not at the poles. If a pair of $n=\pm 1$ vortices are present at different heights $z_{1,2}$, then the fluid in the band between them flows almost horizontally and at a nearly ϕ-independent speed (except for irregularities near the vortices) while the fluid beyond them is approximately stagnant (see Fig. 24). Along any latitude inside the band the circulation is exactly h/m, while it is zero above and below it. These properties approximately determine the flow away from the vortices since the asymmetric irregularities near the vortices decay exponentially, giving a speed of

$$h/2\pi mr(z) \tag{130}$$

in between z_1 and z_2, the locations of the vortices, and zero elsewhere. We describe this approximation as the "band model." This expression shows that constrictions in the surface cause the speed to increase. For the cylinder with spherical caps and arbitrarily placed vortices, Eq. (130) shows that the speed is approximately constant within the band. (It increases within a distance on the order of R from the vortices, which are on the edges of the band.)

The kinetic energy can be determined approximately by noting that the energy in a thin ring on the surface between the vortices (extending from the longitudinal arclength σ to $\sigma+d\sigma$) is

$$[2\pi r(z)d\sigma]\left[\frac{1}{2}\rho_s\left(\frac{\hbar}{mr(z)}\right)^2\right] = \pi K\frac{d\sigma}{r(z)},$$

where the first factor represents the area of the ring since σ is the geodesic distance along the surface and the second factor represents the included kinetic energy. The flow is zero past the two vortices, so the total energy is

$$E = K\pi\int_{\sigma_1}^{\sigma_2}\frac{d\sigma}{r}. \tag{131}$$

For the capped cylinder with a constant $r(z)$ the integral is $\pi KD/R$, where D is the vertical distance between the vortices. This expression generalizes the result for vortices at the poles of the surface, Eq. (128). However, when the vortices are on opposite ends of an equator, they are too close for the asymmetries to be neglected. The energy in this case is calculated in Appendix E. The force $F_{1,\text{band}}$ experienced by vortex 1 can be determined by taking the gradient of Eq. (131). If vortex 1 is moved downward, the band of moving fluid shrinks so the energy drops. The force on the vortex therefore reads

$$F_{1,\text{band}} = [\pi K/r(\sigma_1)]\hat{\boldsymbol{\sigma}}. \tag{132}$$

On the capped cylinder, this force is independent of the positions of the vortices. Even on an arbitrary elongated surface, a noteworthy feature is that the force on vortex 1 does not depend on the position of vortex 2. This force can be explained with the familiar phenomenon of lift: the vortex is on the boundary between stationary and moving fluid, so there is a pressure difference due to the Bernoulli principle.

Approximating the flow pattern generated by multiple vortices in a similar fashion requires only minor modifications of the previous argument. In a low-resolution snapshot of the flow, the point vortices would appear as circles of discontinuity in the velocity field that go all the way around the axis (the analog for a layer of superfluid of a two-dimensional vortex sheet). If the vortices are labeled in order of decreasing z, a loop just below the lth vortex contains

$$N_l = \sum_{i=1}^{l} n_i \tag{133}$$

units of circulation above it. Approximate azimuthal symmetry of the flow then implies that

$$\mathbf{v}(z,\phi)_{\text{band}} = N_l\frac{\hbar}{mr(z)}\hat{\boldsymbol{\phi}} \quad (\text{for } z_l < z < z_{l+1}), \tag{134}$$

a natural generalization of Eq. (130) that is proved in Appendix E.

Conformal mapping can be employed to justify the decay of the nonazimuthally symmetric parts of the flow that are not determined by the quantization condition. We sketch the basic reasoning here by focusing on the flow pattern near the equator of the surface, at a distance σ_{eq} from the north pole. The conformal transformation that maps the elongated sphere onto a regular reference sphere with coordinates Θ,Φ reads (see Appendix E)

$$\tan\frac{\Theta}{2} = \exp\left(-\int_{\sigma}^{\sigma_{eq}} \frac{d\sigma'}{r(\sigma')}\right), \qquad \Phi = \phi. \tag{135}$$

The upper and lower halves of the elongated sphere can be mapped to the upper and lower hemispheres by choosing appropriately between the two values of Θ that correspond to a given value of $\sin\Theta$. Near the equator the integral can be approximated by $(\sigma-\sigma_{eq})/r_{eq}$ since r varies slowly. Suppose the vortices are far from the equator, at a distance greater than kr_{eq} for a large k. Then the vortices above the equator are mapped exponentially close (at a distance less than e^{-k}) to the sphere's north pole. Likewise vortices on the southern half of the surface map exponentially close to the sphere's south pole. We have thus reduced the task of finding the flow due to a complicated arrangement of vortices to a symmetric case. In fact, after mapping the flow on the long, thin surface to the reference sphere, nothing can be resolved beyond a pair of multiply quantized vortices at the north and south poles containing N and $-N$ units of circulation, respectively, where N is the total circulation number of all the vortices above the equator. Since the image vortices are very close to the poles, their flow pattern on the reference surface is approximately azimuthally symmetric near the equator. When mapped back to the elongated surface, the flow retains its approximate azimuthal symmetry in the region around the equator, completing our argument. A similar argument proves the approximate azimuthal symmetry of the flow near lines of latitude other than the equator; one simply adjusts the conformal map in Eq. (135) so that another latitude of the target surface is mapped to the equator of the reference sphere.

Now the geometrical force derived in Eq. (132) can compete with physical forces such as those induced by rotating an ellipsoid about its long axis with angular velocity $\mathbf{\Omega}=\Omega\hat{\mathbf{z}}$. The treatment of rotational forces on curved substrates, introduced in Sec. IV, can be extended to the case of an ellipsoid described by the radial function

$$r(z) = R\sqrt{1-z^2/H^2}. \tag{136}$$

We use the aspect ratio $\alpha=H/R$ to describe how elongated this ellipsoid is, and determine how a vortex-antivortex pair is torn apart by the rotation as the angular frequency is increased. As in Sec. IV, metastable vortex configurations can often be found, so we consider transitions between different *local* minima of the vortex-energy function. Recall that the effect of the rotation on the superfluid energy is expressed in terms of the angular momentum L_z by an extra term $-\Omega L_z$ in Eq. (40), which must be evaluated for a pair of opposite-signed vortices to satisfy the topological constraints imposed by the spherical topology of the surface. We find, in analogy to Eq. (45), that the extra contribution to the vortex energetics is additive and reads

$$-\Omega L_z = n_1\hbar\Omega(\rho_s/m)[A(\sigma_1)-A(\sigma_2)], \tag{137}$$

where $A(\sigma)$ represents the area of the ellipsoid out to a distance σ from the north pole while σ_1 and σ_2 represent the positions of the two defects ($\sigma_1<\sigma_2$). If $n_1=1$, the energy in Eq. (40) is decreased by moving the positive vortex closer to the north pole and the negative one closer to the south pole. To understand this, note that the sense of rotation of the superfluid around a vortex is defined by an observer facing the surface. Hence, a negative vortex on the southern half of the surface rotates in the same direction as a positive one on the northern half (relative to the positive z axis), and both agree with the sense of rotation of the substrate. The rotational force on vortex 1 derived from Eq. (40) is

$$\mathbf{F}_\Omega = -(n_1\hbar\rho_s/m)2\pi r(\sigma)\hat{\sigma}. \tag{138}$$

As Ω increases, *pairs* of positive and negative vortices will appear in this geometry. As each vortex pair is created, the positive vortex will move to the top side of the surface, and the negative one to the bottom. There is a critical frequency Ω_b at which a single pair of vortices, once created, can exist metastably in a configuration symmetric about the x-y plane. As the angular frequency is increased, the vortices are gradually pulled apart until at the frequency Ω_a, they reach the poles. (The latter transition is analogous to the center–off-center transition for a single vortex described in Sec. IV.B.) When $\Omega_a>\Omega>\Omega_b$, the equilibrium condition, obtained by balancing the forces in Eqs. (132) and (138), reads

$$\pi K/r_1 = 2\pi(\hbar\rho_s/m)\Omega r_1. \tag{139}$$

Since r and z are connected by the equation of the ellipsoid, the vortices are located at heights,

$$\pm z \approx \pm\alpha\sqrt{R^2-\hbar/2m\Omega}. \tag{140}$$

The vortices first become metastable when force balance is achieved with both vortices close to the equator. Upon substituting the equatorial value $r_1=R$ into Eq. (139), an estimate of Ω_b is obtained,

$$\Omega_b \approx \hbar/2mR^2. \tag{141}$$

When the pair first appears, there will actually be a nonzero defect separation, although substituting Eq. (141) (which neglects the short-range attraction) into Eq. (140) suggests otherwise. Imagine slowing the rotation speed through Ω_b. The vortices will approach each other gradually; within the large vortex-separation approximation of Eq. (132), the attraction between them will *decrease* as they become closer because $r(z)$ increases.

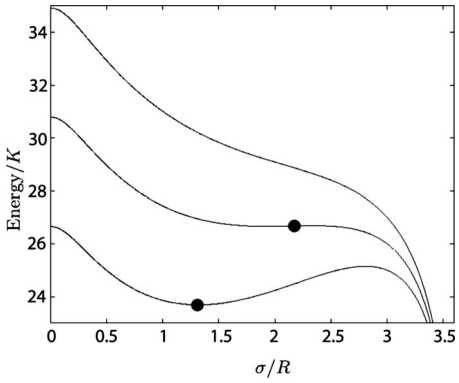

FIG. 25. The rotational and fluid energy (units of K) as a function of $\sigma_1=2\sigma_{\rm eq}-\sigma_2=\sigma$ (units of R) for $H=3.5R$ and $m\omega/\hbar=0.49R^{-2},0.61R^{-2},0.74R^{-2}$. The middle curve, roughly at $\omega=\omega_b$, shows the last position where the vortex is stable as ω is decreased.

However, when the vortices become close enough, the attraction between them starts increasing and the vortices are suddenly pulled together. The minimum z coordinate for metastable vortices is derived along these lines in Appendix E (which also discusses what happens at $\Omega=\Omega_a$) and reads

$$z_1=-z_2=z_b\approx R\ln\alpha. \tag{142}$$

The transition through Ω_b is shown in Fig. 25, which illustrates how the local minimum in the energy function disappears as the frequency decreases.

E. Interactions on a closed surface

To understand interactions between vortices on an arbitrary deformed sphere, one must come to terms with the neutrality constraint on the total circulation of a flow. On any compact surface,

$$\sum_i n_i=0. \tag{143}$$

This constraint on the sum of the circulation indices $\{n_i\}$ always holds: if the surface is divided into two pieces by a curve, the sum of the quantum numbers on the top and bottom halves must be equal and opposite (because they are both equal to the circulation around the dividing curve). As we shall see, this relation implies that there are multiple ways of splitting up the energy into single-particle energies and two-particle interaction energies, despite the fact that the total energy is well defined. The behavior of the one-particle and interaction terms depends on how the splitting is carried out. To illustrate this ambiguity, multiply Eq. (143) by $4\pi^2Kn_1f(\mathbf{u}_1)$ and separate out the $i=1$ term, to obtain

$$4\pi^2n_1^2f(\mathbf{u}_1)=-\sum_{i\neq1}4\pi^2n_1n_if(\mathbf{u}_1). \tag{144}$$

Hence, a portion $4\pi^2Kf(\mathbf{u}_1)$ of the "geometrical energy" of vortex 1 can be reattributed to the interaction of this vortex with all the others. This can be seen explicitly by checking that the *net* energy according to Eqs. (82) and (83), which reads

$$E(\{n_i,\mathbf{u}_i\})=\sum_{i<j}4\pi^2Kn_in_j\Gamma(\mathbf{u}_i,\mathbf{u}_j)-\sum_i\pi n_i^2KU_G(\boldsymbol{u}_i), \tag{145}$$

is not changed by the following transformations:

$$\Gamma'(\mathbf{u}_1,\mathbf{u}_2)=\Gamma(\mathbf{u}_1,\mathbf{u}_2)-f(\mathbf{u}_1)-f(\mathbf{u}_2), \tag{146}$$

$$U_G'(\mathbf{u})=U_G(\mathbf{u})+4\pi f(\mathbf{u}). \tag{147}$$

As we now illustrate, the function U_G defined in Eq. (83) is not equal to ω. If the Green's function on the right-hand side of Eq. (83) is defined as Green's functions on compact surfaces usually are, then $\nabla^2U_G(\mathbf{u})=G(\mathbf{u})-\text{const}$ while Eq. (102) states that $\omega(\mathbf{u})$ satisfies the nonlinear differential equation $\nabla^2\omega(\mathbf{u})=G(\mathbf{u})-e^{2\omega(\mathbf{u})}$ (if $R=1$). The detailed discussion of Green's functions in Appendix D uses the transformation equation (147) to show that, nevertheless, ω and U_G describe the same vortex energetics provided the two-vortex interactions are calculated using Eqs. (81) and (82), respectively.

Here we highlight the ambiguity resulting from the neutrality constraint by performing explicit calculations using two distinct choices of Green's functions on a model surface formed from a unit sphere. First cut the sphere in halves along a great circle. Choose one of the hemispheres and bring opposite sides of the great circle bounding it together and glue them. The result is a pointed sphere resembling a conchigliette noodle (i.e., a shell noodle) sealed shut [see Fig. 26(a)]. The surface closes up smoothly since opposite sides of the seal have matching curvatures; the surface also turns out to be rotationally symmetric. [A similar shape forms when a pollen grain with a weak sector dries out (Katifori *et al.*, 2010).]

The geometrical interaction on this surface can be given an interpretation in terms of the method of images from electrostatics. When one uses the method of images to study charges in a half-space bounded by a conducting plane, one completes the space with the other half-space. Then one introduces charges into this fictitious region to ensure that the right boundary conditions (orthogonality of the field lines to the original boundary plane) are satisfied. For the pointed sphere, we first complete the surface by opening it up again and adding back the second hemisphere. We can describe points on the pointed sphere by (ϕ,σ) (where σ is the distance from the north point and ϕ is the azimuthal angle, as for the general case described in Sec. VI.D). Points on the completed sphere are naturally labeled by the standard spherical coordinates (α,θ) that represent the azimuthal and polar angles, respectively. The mapping from the pointed sphere that returns each point to its position on the original sphere is given by

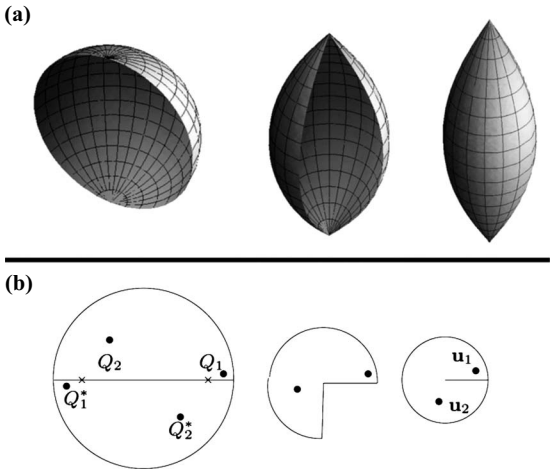

FIG. 26. Applying the method of images to a pointed sphere. (a) The process of folding a hemisphere into a pointed sphere, bounded at the north and south poles by two 180° disclinations. The north and south poles move outward along the axis, while the latitudes stay horizontal. The Gaussian curvature is invariant because the decreasing curvature of the lines of longitude is compensated by the tighter curvature around the lines of lattitude. (b) A top view of vortices during the furling up of one hemisphere. The first stage shows both the $(0<\alpha<\pi)$ hemisphere that will be retained and the other hemisphere together with two defects and their images. The hemisphere is sealed up into the pointed sphere so that the left and right halves of the cut (which appears as a horizontal diameter in this top view) are brought together to form the seam on the pointed sphere; simultaneously, the defects Q_1, Q_2 move to positions $\mathbf{u}_1$ and $\mathbf{u}_2$ on the pointed sphere. The furling process leads to a continuous flow pattern on the pointed sphere. For example, the two points marked with an × on the cut in the original sphere are sealed together. Both points feel a strong flow, the one on the right because it is close to the vortex at Q_1 and the one on the left because it is close to this vortex's image, and these flows are equal.

$$\alpha = \phi/2, \qquad \theta = \sigma. \tag{148}$$

As ϕ ranges from 0 to 2π, α goes from 0 to π, across the hemisphere used to make the pointed sphere. Note that $\theta=\sigma$ since the pointed sphere is formed by isometrically bending the hemisphere (the angle θ is equal to the geodesic distance to the north pole of the hemisphere).

Now for each vortex at $\mathbf{u}=(\phi,\sigma)$ on the pointed sphere, we introduce two vortices on the sphere, one at Q with $(\alpha,\theta)=(\phi/2,\sigma)$ and one at $Q^*=(\phi/2+\pi,\sigma)$. The latter is the image vortex of the former, obtained by rotating Q by 180° around the z axis.

The energy of a defect configuration on the pointed sphere is derived by halving the energy of the flow pattern produced by the doubled set of vortices on the full sphere. In analogy with the electrostatic problem, the purpose of situating the image defects in the way just described is to preserve the continuity of flows across the seam. Imagine drawing the flow pattern of all the vortices on the sphere. Focus on the hemisphere $0<\alpha<\pi$. Because the vortices are placed symmetrically about the sphere's axis, the flow near $\alpha=0$ will match the flow near $\alpha=\pi$ when the surface is sealed [see Fig. 26(b)].

The flow pattern on the pointed sphere results from rolling up half of the flow pattern on the sphere. Once the positions of the image defects are chosen, the flow pattern is found by deriving it from the stream function $\chi(\mathbf{u})$ introduced in Sec. III. The stream function at a point $\mathbf{u}$ on the pointed sphere can be expressed in terms of the Green's function of the sphere, according to Eq. (17),

$$\chi(\mathbf{u}) = \sum_i \frac{n_i h}{m}[\Gamma^{\text{sphere}}(Q,Q_i) + \Gamma^{\text{sphere}}(Q,Q_i^*)], \tag{149}$$

where Q is the point on the sphere corresponding to $\mathbf{u}$ on the pointed sphere and Q_i and Q_i^* are the locations of the ith pair of vortices on the sphere.

The energy of the vortices on the sphere takes up the familiar electrostatic form of a sum of the interactions between all pairs of defects and/or their images. The energy stored in the flow pattern on the pointed sphere (which is half as large as on the complete sphere) reads

$$\begin{aligned}\frac{E_N}{K} &= \frac{1}{4}\sum_{i\neq j} 4\pi^2 n_i n_j[\Gamma^{\text{sphere}}(Q_i,Q_j) + \Gamma^{\text{sphere}}(Q_i,Q_j^*) \\ &\quad + \Gamma^{\text{sphere}}(Q_i^*,Q_j) + \Gamma^{\text{sphere}}(Q_i^*,Q_j^*)] \\ &\quad + \frac{1}{2}\sum 4\pi^2 n_i^2 \Gamma^{\text{sphere}}(Q_i,Q_i^*) \\ &= \frac{1}{2}\sum_{i\neq j} 4\pi^2 n_i n_j[\Gamma^{\text{sphere}}(Q_i,Q_j) + \Gamma^{\text{sphere}}(Q_i,Q_j^*)] \\ &\quad + \sum 2\pi^2 n_i^2 \Gamma^{\text{sphere}}(Q_i,Q_i^*).\end{aligned} \tag{150}$$

In the second expression, we note that the terms in the first line are equal in pairs, so that a factor of $\frac{1}{2}$ cancels. This energy is given the same form as the second line of Eq. (145) by separating out the part which depends on the positions of two vortices, proportional to

$$\Gamma_s(\mathbf{u}_1,\mathbf{u}_2) = \Gamma^{\text{sphere}}(Q_1,Q_2) + \Gamma^{\text{sphere}}(Q_1,Q_2^*) \tag{151}$$

and the part which depends on one vortex,

$$U_s(\mathbf{u}) = -2\pi\Gamma^{\text{sphere}}(Q,Q^*). \tag{152}$$

The function in Eq. (151) is a Green's function for the pointed sphere, as the placement of the images guarantees that this function is well defined on the *pointed sphere*. It appears in the stream function, Eq. (149), as well as in the energetics, as expected for a Green's function.

The potential which describes the single-particle energy of a vortex becomes singular as the vortex approaches the apex of the cone at the north or south pole, since then the vortex Q approaches its image Q^*. This is in accord with the result, Eq. (83), that the Gaussian

curvature is the source of the single-particle energy since the pointed sphere has delta-function concentrations of curvature at its north and south poles,

$$G(\mathbf{u}) = 1 + \pi\delta_N(\mathbf{u}) + \pi\delta_S(\mathbf{u}), \tag{153}$$

where $\delta_N(\mathbf{u})$ and $\delta_S(\mathbf{u})$ are the appropriate delta funnctions. The geometric repulsion from the positive curvature points arises from the repulsion between vortices and their images. We can check step by step that U_s is sourced by the Gaussian curvature,

$$U_s(\mathbf{u}) = -\int\int \Gamma_s(\mathbf{u},\mathbf{u}')G(\mathbf{u}')d^2\mathbf{u}'. \tag{154}$$

We substitute for $G(\mathbf{u}')$ from Eq. (153) and for Γ_s from Eq. (151) which can be written in the form,

$$\begin{aligned}\Gamma_s(\sigma_1,\phi_1;\sigma_2,\phi_2) &= \Gamma^{\text{sphere}}\left(\sigma_1,\frac{\phi_1}{2};\sigma_2,\frac{\phi_2}{2}\right) \\ &\quad + \Gamma^{\text{sphere}}\left(\sigma_1,\frac{\phi_1}{2};\sigma_2,\frac{\phi_2}{2}+\pi\right) \\ &= -\frac{1}{4\pi}\ln 4\left[(1-\cos\sigma_1\cos\sigma_2)^2\right. \\ &\quad \left. -\sin^2\sigma_1\sin^2\sigma_2\cos^2\frac{\phi_1-\phi_2}{2}\right].\end{aligned} \tag{155}$$

In the last line, we have evaluated the Green's function for the sphere by writing the chordal distance between Q_1 and Q_2 in terms of the spherical coordinates $(\alpha_{1,2},\theta_{1,2})$, $D^2=2[1-\cos\theta_1\cos\theta_2-\sin\theta_1\sin\theta_2\cos(\alpha_1-\alpha_2)]$ [see Lubensky and Prost (1992)], and then combining the two terms together. To evaluate the integral in Eq. (154), we note that the area element of this integral is $d^2\mathbf{u}=\frac{1}{2}\sin\sigma d\sigma d\phi$. The area of a region on the pointed sphere is the same as the area $\sin\theta d\theta d\alpha$ of the corresponding region on the original sphere, and the factor of $\frac{1}{2}$ results from how the angles are related, $\alpha=\frac{\phi}{2}$, see Eq. (148). Now the integral on the right-hand side of Eq. (154) can be shown to be equal to the left-hand side using the identities

$$\begin{aligned}&\int_0^{2\pi}\ln|A+B\cos t|dt \\ &\quad = \begin{cases} 2\pi\ln\dfrac{A+\sqrt{A^2-B^2}}{2} & \text{if } B<A \\ 2\pi\ln\dfrac{B}{2} & \text{if } B>A. \end{cases}\end{aligned}$$

We have now derived one formulation of the energetics in terms of Γ_s and U_s, the corresponding geometric potential. We contrast this isometric mapping method with the conformal mapping method in order to illustrate how different approaches can naturally lead to different delineations between vortex-vortex and vortex-curvature interactions. (The net result is of course the same from either point of view.) As a result of the isometric mapping each point is doubled, whereas the distance-distorting conformal mapping transforms each point on the pointed sphere to one point on the reference sphere.

We first use Eq. (135) to find that the conformal map is given by

$$\tan\Theta/2 = \tan^2\sigma/2. \tag{156}$$

[Note that $r(\sigma)=\frac{1}{2}\sin\sigma$.] Comparing the conformal mapping results, Eqs. (80) and (81), to the Green's function formulation, Eqs. (83) and (82), suggests the following identification of the interaction potential (or Green's function) and single-particle potential:

$$\begin{aligned}&\Gamma_c(\mathbf{u}_1,\mathbf{u}_2) = \Gamma^{\text{sphere}}(\Theta(\sigma_1),\phi_1;\Theta(\sigma_2),\phi_2), \\ &U_c(\mathbf{u}) = \omega = \ln\frac{2\sin\sigma}{1+\cos^2\sigma}.\end{aligned} \tag{157}$$

These expressions differ from Eqs. (151) and (152). Nevertheless, as promised, the net energy is the same whether the pairs (Γ_s,U_s) or (Γ_c,U_c) are used in place of Γ and U_G. In fact,

$$\begin{aligned}&\Gamma_c(\mathbf{u}_1,\mathbf{u}_2) = \Gamma_s(\mathbf{u}_1,\mathbf{u}_2) - f(\mathbf{u}_1) - f(\mathbf{u}_2), \\ &U_c(\mathbf{u}) = U_s(\mathbf{u}) + 4\pi f(\mathbf{u}),\end{aligned} \tag{158}$$

where $f(\mathbf{u})=-(1/4\pi)\ln(1+\cos^2\sigma)$. This transforms the energy from the single-particle to the interaction terms consistently as described at the beginning of the section. Appendix D shows that the Green's function formulation is generally equivalent to the conformal mapping result derived in Sec. VI.A, even when there is no method of images that can be used to determine the Green's function explicitly in general.

VII. LIMITS ON THE STRENGTH AND RANGE OF GEOMETRICAL FORCES

Geometrical forces are limited in strength due to the nonlinear relation between the curvature and the geometric potential. Curvature affects both the source of the geometrical force and the force law, as illustrated in Sec. IV.C as well as Secs. VI.C and VI.D. As a consequence, even on a wildly distorted surface (with planar topology), there is a precise limit on the strength of the force on a single vortex as the esimates in Sec. III.D suggest. This result has the character of a geometrical optimization problem, like maximizing the capacitance of a solid when the surface area is given. Consider a vortex located at the center of a geodesic disk of radius R. Assume that the Gaussian curvature is zero within the disk, but may be different from zero elsewhere. Then the force $\mathbf{F}$ due to the curvature satisfies

$$|\mathbf{F}| \leq 4\pi K n_1^2/R, \tag{159}$$

where n_1 is the number of circulation quanta in the vortex. This relation between R and $\mathbf{F}$ is proven in Appendix F.

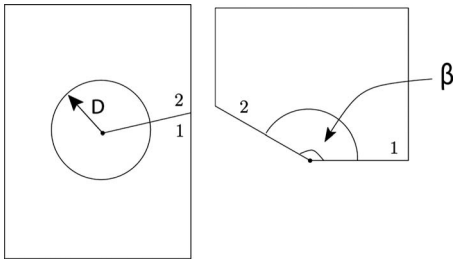

FIG. 27. How to form cones of negative curvature. One complete sheet of paper is slit and an angle is cut out of an additional sheet of paper. The edges labeled 1 are taped together, and then the edges labeled 2 are taped. The circular arcs join together to form an extra-large circle. The cone angle is $\theta = 2\pi + \beta$, and cones with even larger cone angles can be formed using additional sheets.

If one warps a surface in a vain attempt to overcome the limit, the force gets diluted because the distortion of the region around the curvature pulls the force lines apart, as we can understand from the simple example of vortices on cones.

A cone of cone angle θ is obtained by taking a segment of paper with an angle θ and gluing the opposite edges of the angle together. This is most familiar when $\theta < 2\pi$. If $\theta = 2\pi m + \beta$, such a cone can be produced by adding m extra sheets of paper, as shown in Fig. 27. We slit the m sheets of paper and put them together with an angle of size β cut out of an additional sheet. By gluing the edges of the slits together cyclically, a cone of arbitrary angle θ is made.

A cone has a delta function of curvature at its apex, but no Gaussian curvature elsewhere because the surface can be formed from a flat piece of paper without stretching. The weight of the delta function is the integral of the Gaussian curvature in any region containing the apex which can be expressed, according to the Gauss-Bonnet theorem (Kamien, 2002) as

$$\int\int G(\mathbf{u})d^2\mathbf{u} = 2\pi - \oint \kappa ds, \tag{160}$$

where κ is the geodesic curvature along the boundary of the region and s is its arclength. Apply this formula to the circle of radius D centered at the apex of the cone. Imagine the circle as it would appear on the original sheets of paper, as in Fig. 27. Its measure in radians is $\beta + 2\pi m = \theta$ since it consists of m complete circles together with an additional arc. The length is therefore $S = D\theta$. The *geodesic* curvature of the circle does not change when the cone is unfolded, so it is equal to $1/D$. Upon substituting into Eq. (160), we obtain

$$\int\int G(\mathbf{u})d^2\mathbf{u} = 2\pi - S\frac{1}{D} = 2\pi - \theta. \tag{161}$$

When $\theta > 2\pi$ the curvature is negative.

Now imagine a vortex (with $n_1 = \pm 1$, say) at a distance D from the cone point, on the circle of circumference S just considered. The arbitrarily large negative curvature which is possible by making m large seems to defy the general upper bound on the geometric force. According to Newton's theorem, applied to the radius D circle centered at the cone's apex and passing through the vortex, the force on the vortex is

$$F = \frac{\pi K \int\int G d^2\mathbf{u}}{S}.$$

Since the circumference $S = D\theta$ is larger than it would be in the plane, the force is diluted; substituting the integrated curvature from Eq. (161), we find that it is given by

$$F = \pi \frac{K}{D}\frac{2\pi - \theta}{\theta}. \tag{162}$$

This satisfies Eq. (159) for all negatively curved cones ($\theta > 2\pi$); even when $\theta \to \infty$ the magnitude of the force is less than $4\pi K/D$ because the large circumference in the denominator of the Newton's theorem expression cancels the large integrated curvature in the numerator.

In the opposite limit $\theta \to 0$, the theorem described by Eq. (159) is still correct of course. One has to be careful about applying it, however. The force on a vortex at radius D [given by Eq. (162)] exceeds $4\pi K/R$ with R set equal to D when θ is small enough [in fact, for an extremely pointed cone, $\theta \ll 1$, the force given by Eq. (162) diverges], but this does not contradict the inequality because the circle of radius D centered at the vortex is pathological: although it does not contain any curvature, the circle wraps around the cone and intersects itself. Taking R to be the radius of the largest circle centered at the defect which does not intersect itself, one finds that the inequality is satisfied for all values of the cone angle θ (see Appendix F). One can describe a more awkwardly shaped surface such that the force on a singly quantized vortex is arbitrarily close to the upper bound $4\pi K/R$ (see Appendix F).

One can also provide limits to the strength of the geometric force from a localized source of curvature. Rotationally symmetric surfaces such as the Gaussian bump have force fields that do not extend beyond the bump, since the net Gaussian curvature is zero, and Newton's theorem says that only the *integrated* Gaussian curvature can have a long-range effect for a rotationally symmetric surface. To get a longer-range force, one must focus on nonsymmetric surfaces, like the saddle surface of Sec. III.B. The integration methods of Appendix A can be used to show that this surface's potential has a quadrupole form at long distance. Consider, more generally, a plane which is flat except for a nonrotationally symmetric deformation confined within radius R of the origin. (The result will not apply directly to the saddle surface since its curvature extends out to infinity.) In this case, the total integrated Gaussian curvature is zero, implying that the long-range force law cannot have any monopole component. A dipole component is not ruled out by this simple reasoning, but Appendix F shows that the limit-

TABLE I. An outline of vortex interactions on curved surfaces. The net energy of a set of vortices on a surface with the topology of a plane, disk, or sphere is given by $\Sigma_i n_i^2 E_1(\mathbf{u}_i) + \Sigma_{i<j} E_2(\mathbf{u}_i, \mathbf{u}_j)$, where simple expressions for the single-particle (or geometric) potential and two-particle potentials are given. A conformal mapping is necessary for evaluating some of the these expressions. For example, $\boldsymbol{\mathcal{U}}_i$ (in the expression for the Green's function on a deformed plane) is the Cartesian coordinates of the conformal image of vortex i.

	Deformed plane	Deformed disk	Deformed sphere
Interaction $E_2(\mathbf{u}_i, \mathbf{u}_j)$	$Kn_i n_j\left[4\pi^2\Gamma(\mathbf{u}_i,\mathbf{u}_j) - 2\pi \ln\frac{R}{a}\right]$	$4\pi^2 K n_i n_j \Gamma_D(\mathbf{u}_i,\mathbf{u}_j)$	$4\pi^2 K n_i n_j \Gamma_p(\mathbf{u}_i,\mathbf{u}_j)$
Green's function	$-\frac{1}{2\pi}\ln\frac{\lvert\boldsymbol{\mathcal{U}}_i - \boldsymbol{\mathcal{U}}_j\rvert}{a}$	$\frac{1}{4\pi}\ln\left(\frac{1+\mathcal{R}_i^2\mathcal{R}_j^2 - 2\mathcal{R}_i\mathcal{R}_j\cos(\Phi_i-\Phi_j)}{\mathcal{R}_i^2+\mathcal{R}_j^2-2\mathcal{R}_i\mathcal{R}_j\cos(\Phi_i-\Phi_j)}\right)$	$-\frac{1}{2\pi}\ln\frac{\mathcal{D}_{ij}}{a} + \frac{1}{4\pi}[\omega(\mathbf{u}_i)+\omega(\mathbf{u}_j)]$
Geometric potential, $E_1(\mathbf{u}_i)$	$K\pi\left[\int\int d^2\mathbf{u}\Gamma(\mathbf{u}_i,\mathbf{u})G(\mathbf{u}) + \ln\frac{R}{a}\right]$	$\pi K \ln\frac{1-\mathcal{R}_i^2}{a} - \pi K\omega(\mathbf{u}_i)$	0
Differential equation for $E_1(\mathbf{u}_i)$	$\nabla^2 E_1(\mathbf{u}_i) = -\pi K G(\mathbf{u}_i)$	$\nabla^2 E_1(\mathbf{u}_i) = -\pi K G(\mathbf{u}_i) - \frac{4\pi K}{a^2} e^{-2E_1(\mathbf{u}_i)/\pi K}$	
Applications	Gaussian bumps and saddles: Secs. III.A–III.C Periodic surfaces: Secs. VI.C Nearly flat geometry: Appendix A	Interactions with images: Sec. IV.C Bounded Enneper surface: Sec. VI.B	Band flows on surfaces: Sec. VI.D Neutrality and Green's function flexibility: Appendix D

ing form of the potential is at least a *quadrupole* (or a faster decaying field),

$$E(\mathbf{r}) \sim n_1^2 \mu_2 \cos(2\phi - \gamma_2)/r^2, \tag{163}$$

where r and ϕ are the polar coordinates of the vortex relative to the origin, and μ_2 and γ_2 are constants that depend on the shape of the deformation in the vicinity of the origin. As in the previous case, there is an upper limit on the quadrupole moment μ_2, no matter how strong the curvature of the deformation is,

$$\mu_2 \leqslant \pi K R^2. \tag{164}$$

For electrostatics in the plane, the maximum quadrupole moment of N particles with charge 2π and N with charge -2π in a region of radius R is at most of the order of KNR^2, which has the same form as the bound in Eq. (164), except for the factor of N, which is umlimited. Because of the nonlinearity of the geometrical force and restrictions on how much positive and negative curvature can be separated from each other, the geometric quadrupole moment is bounded by the quadrupole moment of a small number of vortices no matter how drastically curved the surface is.

These results describe key physical *differences* (resulting from the fact that the curvature cannot be adjusted without changing the surface) between the geometrical forces discussed here and their electrostatic counterparts despite the close resemblance from a formal viewpoint.

VIII. CONCLUSION

In this article, we have laid out a mathematical formalism based on the method of conformal mapping that allows one to calculate the energetics of topological defects on arbitrary deformed substrates with a focus on applications to superfluid helium films. The starting point of our approach is the observation that upon a change of coordinates the metric tensor of a complicated surface can be brought into the diagonal form $g_{ab} = e^{2\omega(\mathbf{u})}\delta_{ab}$. This corresponds to the metric of a flat plane which is locally stretched or compressed by the conformal factor $e^{2\omega(\mathbf{u})}$. Many of the geometric interactions experienced by topological defects on curved surfaces are simply determined once the function $\omega(\mathbf{u})$ is known.

The curved geometry results in a modified law for defect interaction as well as in a one-body geometric potential. The geometric potential is always weaker than the field produced by one or two other vortices (see Secs. III.D, IV.C, IV.D, and VII). The changes to the defect interactions can be important even when the single particle force is weak (Secs. VI.C and VI.D). Table I presents a summary of the general form that the defect interaction (first row) and the geometric potential (third row) take up in curved spaces with the topology of a deformed plane (first column), disk (second column), and sphere (third column). These results can be derived starting from the differential equations that the geometric potential satisfies or the appropriate Green's functions that we list in the second and fourth rows, respectively, for each of the three surface topologies. The fifth row of Table I directs readers towards the relevant sections and appendixes of the paper where they will be able to find applications of the formalism and technical derivations.

On a deformed plane, the self-energy can be found by solving directly a covariant Poisson equation with the Gaussian curvature as a source. This task is simplified in the case of surfaces with azimuthal symmetry, such as the Gaussian bump described in Sec. III.A, because one can apply Gauss's law as familiar from electromagne-

tism. In general, the energetics of many defects is described by Eqs. (82) and (83). On strongly distorted geometries, like deformed spheres or disks, a more efficient route to the derivation of vortex energetics is obtained with the method of conformal mapping. In these more complicated cases, the one-body interactions are no longer described by the Poisson equation. This is illustrated in the examples discussed in the second part of this paper (please refer to the fifth row of Table I).

On a deformed sphere, the scale factor ω obtained from the conformal mapping is determined by the nonlinear equation (102), because of the nonzero curvature of the reference sphere. On a deformed disk, like the Enneper disk (a minimal surface of negative curvature described in Sec. VI.B), the scale factor satisfies Poisson's equation, but there is an additional interaction with image defects that accounts for the presence of the boundary. The overall one-body potential (generated by the curvature and the boundary of the deformed disk) satisfies a nonlinear differential equation analogous to the one arising for a deformed sphere, the Liouville equation listed in Table I. Solving these nonlinear equations can be circumvented using conformal mappings to obtain directly the scale factor $\omega(\mathbf{u})$ and the interactions of the vortices among themselves as well as with the curvature and boundary of the manifold. An alternative approach for the case of deformed spheres expresses the energies by means of Eqs. (83) and (82) with appropriately chosen Green's functions, as shown in Appendix D. In fact, the two-vortex interaction can be defined in such a way that all geometric effects are accounted for without introducing a one-body geometric potential explicitly; this is the formulation presented in Table I, so E_1 *vanishes*. This formulation is made possible by the constraint of topological charge neutrality that exists on a compact surface.

There is an overarching theme that underlies all the examples presented in the last sections. The most interesting physical phenomena that take place in a curved two-dimensional space can be viewed as a reflection of the geometry of the corresponding conformal maps. For example, the two-vortex interaction on a periodically modulated surface is anisotropic, because the conformal map to the plane stretches the lattice of the surface anisotropically. Similarly, the interaction energy between two defects on an elongated ellipsoid grows linearly with their separation, instead of logarithmically, because the conformal map from the ellipsoid to a sphere compresses the vortex cores by a factor that grows exponentially with their distance from the equator. This fact can also be explained more intuitively, starting from the quantization of circulation, as discussed in Sec. VI.D. Last, even the upper bound on the strength of the geometric forces arises from the connection between conformal maps and analytic functions.

We hope that the discussion of the geometric effects presented may also pave the way for the observation of the anomalous coupling in thin superfluid (see Sec. V) or liquid crystal layers on a curved substrate. A useful starting point could be the design of experiments to detect the geometric potential by balancing it with forces exerted on the defects by external fields or rotation of the sample as discussed in Sec. IV. Such experiments should focus on single vortices, or on situations where the separation between vortices is comparable to the length scale of the geometry.

While vortices in thin helium layers wetting a curved surface are a natural arena to explore the interplay between geometry and physics, the mathematical methods presented are also applicable to two-dimensional liquid crystals and crystals. Liquid crystal defects (at least when boundary interactions are not taken into account) are described by the same potentials as helium vortices, with only a slightly different coupling rule [see Eq. (2)]. The conformal mapping methods illustrated here can also be used to solve the biharmonic equation which occurs in the study of two-dimensional crystals. Moreover, bending a liquid crystal or crystal monolayer naturally causes the nucleation of disclinations and dislocations, which can be more easily imaged by microscopy than helium vortices.

ACKNOWLEDGMENTS

We thank B. Halperin, R. D. Kamien, S. Trugman, and R. Zieve for helpful suggestions. A.M.T., V.V., and D.R.N. acknowledge financial support from the National Science Foundation, through Grant No. DMR-0654191, and the Harvard Materials Research Science and Engineering Center through Grant No. DMR-0820484. V.V. acknowledges financial support from NSF under Grants No. DMR05-47230 and No. DOE-DE-FG02-05ER46199. It is a pleasure to acknowledge the Aspen Center for Physics for providing an interactive research environment where this article was completed.

APPENDIX A: NEARLY FLAT SURFACES

The calculations in Sec. III.B are based on perturbations about near flatness [see David (1989), and references therein]. The perturbation theory will be in powers of an aspect ratio α, which measures the ratio of surface height to width of the landscape features. [We imagine that the height of the surface is given in the form $\alpha m(x,y)$, where m is a fixed function.] The leading corrections to the flat space energies are second order in α. There are two of these; one is the geometric potential. When there are at least two vortices present, there is also a second-order correction to the Green's function, which ought to be retained since it is comparable to the geometric potential. The latter could be calculated by expanding the metric in Eq. (13) in powers of α. Nevertheless, because the perturbations are singular, we prefer to use conformal mapping for this step just as we use in Sec. VI.A to derive the geometric potential. Our calculations are limited to the case of an infinite deformed plane.

We use the x and y coordinates of a plane parallel to the surface for our coordinate system (the "Monge

gauge"). The metric is then $ds^2=dx^2+dy^2+dz^2=(1+h_x^2)dx^2+(1+h_y^2)dy^2+2h_xh_ydxdy$. Subscripts on h indicate derivatives, so that $h_{xx}=\partial_x^2 h$, etc. Upon calculating the curvature tensor we find the Gaussian curvature in the second-order approximation (David, 1989),

$$G(x,y)=h_{xx}h_{yy}-h_{xy}^2. \tag{A1}$$

The geometric potential is found by approximating the exact expression (29). The Green's function may be replaced by the planar one since G is already quadratic in α,

$$U_G(x,y)=-\frac{E}{\pi K}\approx-\int\int dx'dy'\Gamma_{\text{flat}}(x,y;x',y')\times(h_{xx}h_{yy}-h_{xy}^2). \tag{A2}$$

To do a conformal mapping to an equivalent flat space problem, we must solve the curved-space generalization of the Cauchy-Riemann equations (David, 1989) which define isothermal coordinates $\mathcal{X},\mathcal{Y}$, namely,

$$\nabla^a(Y)=-\gamma_b^a\nabla^b(X), \tag{A3}$$

where $\gamma_b^a=g^{ac}\sqrt{g}\epsilon_{cb}$. (In other words, the gradients of $\mathcal{X}$ and $\mathcal{Y}$ are at right angles to each other and have equal magnitudes at every point.) We insert the expression for the metric in terms of h into Eq. (A3) and expand to second order under the assumption that $\mathcal{X}=x+\xi$, $\mathcal{Y}=y+\eta$ where the deformation parameters ξ and η are second order in α,

$$\eta_x+\xi_y\approx h_xh_y, \tag{A4}$$

$$\eta_y-\xi_x\approx\tfrac{1}{2}(h_y^2-h_x^2). \tag{A5}$$

By taking the derivative of Eq. (A4) with respect to x and Eq. (A5) with respect to y and adding the results, we obtain

$$\nabla_{\text{flat}}^2\eta\approx h_y\nabla_{\text{flat}}^2h, \tag{A6}$$

which may be solved by means of the Green's function (keeping in mind the boundary condition that the conformal map must approach the identity at infinity; i.e., $\eta\to0$), giving the result

$$\eta(x,y)\approx-\int\int dx'dy'\Gamma_{\text{flat}}(h_y\nabla_{\text{flat}}^2h). \tag{A7}$$

Similarly, we may solve for ξ [and then check that Eq. (A5) is satisfied].

We can use our expression for the conformal mapping in conjunction with the conformal invariance of the Green's function, Eq. (84), which implies that $\Gamma(x_1,y_1;x_2,y_2)=\Gamma_{\text{flat}}(x_1+\xi_1,y_1+\eta_1;x_2+\xi_2,y_2+\eta_2)$. Upon expanding the flat space Green's function in ξ and η, we have

$$\Gamma(x,y;x',y')\approx-\frac{1}{4\pi}\ln(\Delta x^2+\Delta y^2)-\frac{\Delta\xi\Delta x+\Delta\eta\Delta y}{2\pi(\Delta x^2+\Delta y^2)}, \tag{A8}$$

where ΔQ indicates taking the difference between the values of Q at the two points where the Green's function is evaluated. Equation (A7), and its analog for ξ now show that Eq. (A8) gives the interaction energy to the same order as the geometric potential.

Two vortices of opposite signs that are very near to one another (a distance l such that $a\ll l\ll r_0$ for a Gaussian bump, say) cannot tell whether they are in curved or flat space. Indeed, the flow fields cancel one another outside a range moderately greater than l. If l is much less than the curvature scale, the effects of curvature are negligible. The energy of the vortices should therefore be $2\pi K\ln(l/a)$ as in flat space. This conclusion can be checked explicitly in the small-aspect-ratio approximation by combining the expressions for the geometric interaction and the correction to the Green's function equations (A2) and (A8). [One can take the $\Delta x,\Delta y\to0$ limit of $(\Delta\xi\Delta x+\Delta\eta\Delta y)/(\Delta x^2+\Delta y^2)$ with the help of Eqs. (A4), (A5), and (A7).] As expected, the dependence on the surface profile h cancels. This consistency check was behind our original suspicion about the existence of a geometric interaction. The energy of two vortices at $\mathbf{u}_1,\mathbf{u}_2$ without the geometric interaction included is $-4\pi^2K\Gamma(\mathbf{u}_1,\mathbf{u}_2)$. This energy differs from the flat space energy even when the vortices are very close to one another by a position-dependent contribution,

$$E_{\text{int}}(\mathbf{u}_1,\mathbf{u}_2)\approx2\pi K\ln s_{12}-4\pi^2Kg[\tfrac{1}{2}(\mathbf{u}_2+\mathbf{u}_1)]. \tag{A9}$$

This cannot be the correct expression, since the energy should be the same as in flat space. Single-particle energies give a simple resolution. If the total energy were

$$E=-4\pi^2K\Gamma(\mathbf{u}_1,\mathbf{u}_2)+2\pi^2Kg(\mathbf{u}_1)+2\pi^2Kg(\mathbf{u}_2), \tag{A10}$$

then all g's will cancel when $\mathbf{u}_1\to\mathbf{u}_2$. The Green's function calculations by Vitelli and Nelson (2004) and the conformal mapping calculations in Sec. VI.A show that this is actually the correct resolution, and that $g(\mathbf{u})=-U_G(\mathbf{u})/2\pi$.

APPENDIX B: THE SADDLE SURFACE'S POTENTIAL

For the saddle surface with a small aspect ratio [see Eq. (30)], we may determine the entire geometric potential analytically as a function of position. We only outline the procedure here. We evaluate

$$U_\rho(\mathbf{r})=-\int\frac{1}{2\pi}\ln|\mathbf{r}-\mathbf{r}'|\rho(\mathbf{r}')dx'dy' \tag{B1}$$

when $\rho(x,y)=G(x,y)$ is the curvature of the surface [at the point vertically above (x,y); we are using the small-aspect-ratio approximation of Appendix A]. Some thought shows that the curvature given by Eq. (A1) for the surface Eq. (30) takes the form of a polynomial P

times $G_0 = e^{-(x^2+y^2)/r_0^2}$. We therefore discuss how to evaluate the potential U_ρ for "charge" distributions of the form

$$\rho(x,y) = P(x,y)e^{-(x^2+y^2)/r_0^2}. \tag{B2}$$

We start with $\rho = G_0$; as discussed above, the azimuthal symmetry of this distribution allows its potential to be determined by Gauss's law,

$$-\nabla U_{G_0} = \frac{\mathbf{r}}{2\pi r^2}\int_0^r 2\pi r' G_0(r')dr'. \tag{B3}$$

This integral is elementary and U_{G_0} can be evaluated by one further integration, although this cannot be done in closed form.

Conveniently, the potential due to a distribution of the form (B2) can be determined from the special case of $\rho = G_0$ by differentiation. (Intuitively, derivative charge distributions such as $\partial_x G_0$ are superpositions of infinitesimally shifted copies of G_0. We can therefore apply superposition to find potentials for such distributions. This is analogous to finding the electric fields of multipoles by differenting the monopole field.) To this end, we rewrite Eq. (B1) for the special case $\rho = G_0$ as

$$U_{G_0}(\mathbf{r}) = -\int \frac{1}{2\pi}\ln|\mathbf{\Delta}|G_0(\mathbf{r}-\mathbf{\Delta})d\Delta_x d\Delta_y, \tag{B4}$$

where (Δ_x, Δ_y) are the components of $\mathbf{\Delta} = \mathbf{r} - \mathbf{r}'$. It follows that

$$\partial_x^n \partial_y^m U_{G_0}(\mathbf{r}) = -\int \frac{1}{2\pi}\ln|\mathbf{\Delta}|\partial_x^n \partial_y^m G_0(\mathbf{r}-\mathbf{\Delta})d\Delta_x d\Delta_y. \tag{B5}$$

The right-hand side represents the potential corresponding to the source in Eq. (B2) with a special degree k polynomial in place of P. This polynomial, obtained by multiple differentiations of a Gaussian, is complicated, but polynomials of this specific form can be superimposed to give any desired polynomial (including the degree 8 polynomial appropriate to our Gaussian saddle surface). We then, in principle, can express U_G as a superposition of U_{G_0} and its derivatives.

The expansion of the charge distribution of Eq. (B2) in terms of the derivatives of G_0 can be carried out with the help of Fourier integrals. Our goal is to find an expression of the form

$$\rho(x,y) = P(x,y)e^{-x^2-y^2} = Q(\partial_x, \partial_y)e^{-x^2-y^2}, \tag{B6}$$

where $P(x,y)$ is the polynomial appearing in Eq. (B2). We determine a polynomial operator $Q(\partial_x, \partial_y) = \Sigma_{n,m} q_{nm}\partial_x^n \partial_y^m$ so that Eq. (B6) is true. We have set $r_0 = 1$ for convenience. Applying the Fourier transform to both sides of Eq. (B6) gives

$$P(i\partial_{p_x}, i\partial_{p_y})e^{-[(p_x^2+p_y^2)/4]} = Q(ip_x, ip_y)e^{-[(p_x^2+p_y^2)/4]}, \tag{B7}$$

or (by substituting $u = ip_x, v = ip_y$)

$$Q(u,v) = e^{-[(u^2+v^2)/4]}P(-\partial_u, -\partial_v)e^{[(u^2+v^2)/4]}. \tag{B8}$$

The operator $Q(\partial_x, \partial_y)$ which satisfies Eq. (B6) can be produced by working out the derivatives in this expression and replacing u and v by ∂_x and ∂_y. Now the potential can be worked out using

$$U_G(\mathbf{r}) = Q(\partial_x, \partial_y)U_{G_0}(r). \tag{B9}$$

In fact, multiplying Eq. (B5) by q_{nm} and summing over n and m shows [with the help of Eq. (B6)] that $Q(\partial_x, \partial_y)U_{G_0}(\mathbf{r}) = -(1/2\pi)\int\int \ln|\Delta|\rho(|\mathbf{r}-\mathbf{\Delta}|)d\Delta_x d\Delta_y$.

Since all *derivatives* of U_{G_0} can be calculated analytically starting from Eq. (B3), Eq. (B9) will yield an analytic expression for U_G, provided we can show that Q has no constant term. To show this, we integrate both sides of Eq. (B6) to see that

$$\pi Q(0,0) = \int P(x,y)e^{-(x^2+y^2)}dxdy = \int G(x,y)dxdy. \tag{B10}$$

That is, Q's constant term is proportional to the net Gaussian curvature; since the net curvature is zero for any surface which flattens out at infinity, Q has no constant term.

The potential of the saddle surface can thus be determined in closed form by the following procedure: expand the curvature to determine the polynomial P. Calculate Q from (B8). Since (B10) guarantees that Q has no constant term, we may calculate the geometrical potential by differentiating (B3) repeatedly. This method is not much more practical for human calculations than is numerically integrating (B1) by hand. A computer program, such as MATHEMATICA (which produced 272 terms), can use Eqs. (B9) and (B8) to calculate the values rapidly and make the graphs shown in Figs. 11 and 8. There is one comprehensible consequence of these calculations: the long-distance potential is dominated by a quadrupole, attracting vortices from some directions and repelling them towards others. Hence there are four additional local minima *outside* of the central trap.

APPENDIX C: van der WAALS ATTRACTION ON A CURVED SURFACE

Consider a film that completely wets a solid surface. The substrate itself is described by its height function $h(\mathbf{x})$, where $\mathbf{x} = (x,y)$ denotes a pair of Cartesian coordinates in the horizontal plane below the surface (see Fig. 28), while the liquid-gas interface is described by $h_L(\mathbf{x})$.

The energy corresponding to the van der Waals interaction can be expressed in the form

$$E_{\mathrm{vdW}} = \int\int d^2\mathbf{x}\int_{h_L(\mathbf{x})}^{\infty} dz \int\int d^2\mathbf{x}' \times \int_{-\infty}^{h(\mathbf{x}')} dz' w[\sqrt{(\mathbf{x}-\mathbf{x}')^2 + (z-z')^2}]. \tag{C1}$$

This expression models the force between the helium

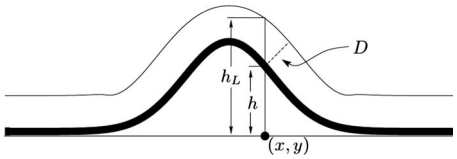

FIG. 28. Definition plot for a laminating film. $h(\mathbf{x})$ is the height of the substrate above the horizontal surface at a point $\mathbf{x}=(x,y)$, and $h_L(\mathbf{x})$ is the height of the upper surface of the film. $D(\mathbf{x})$ is the thickness of the film which (if the film has a slowly varying thickness) is given by $[h_L(\mathbf{x})-h(\mathbf{x})]\cos\theta(\mathbf{x})$, where $\theta(\mathbf{x})$ is the local inclination angle of the substrate.

atoms and the substrate assuming for simplicity a nonretarded two-body van der Waals interaction. [Liquid helium films were used as an early test (Sabisky and Anderson, 1973) of the more accurate Lifshitz theory of dispersion forces (Evans and Wennerström, 1999); see also Maradudin and Mazur (1980) and Mazur and Maradudin (1981) for the effects of retardation]. The energy involves an integral over interactions between pairs of points, one above the helium film and one in the substrate, but with no points in the liquid helium itself. This is equivalent to including interactions between all pairs of atoms contained in all combinations of the vapor, liquid, and solid regions, as long as $w(r)=-\alpha r^{-6}$ where α is the appropriate combination of parameters for these phases (Andelman *et al.*, 1988).

Now if the film thickens by a small amount above the point $\mathbf{x}$, then a small volume of gas around the point $\mathbf{r}=\{\mathbf{x},h_L(\mathbf{x})\}$ is replaced by liquid. Hence the disjoining pressure p_{vdW} defined by Eq. (68) expresses the energy of interaction between the substrate and the replaced gas,

$$p_{\mathrm{vdW}}(\mathbf{r})=\int w(|(\mathbf{r}-\mathbf{r}'|)d^3\mathbf{r}', \tag{C2}$$

where the integral over $\mathbf{r}'$ extends over the interior of the substrate. For a very thin film on a flat substrate, the dependence of the disjoining pressure on the film thickness D can be found by integrating Eq. (C2) with the standard result (de Gennes *et al.*, 2004)

$$p_{\mathrm{vdW}}(D)=-A_H/6\pi D^3, \tag{C3}$$

where $A_H=\pi^2\alpha$ is the Hamaker constant for the solid and the vapor interacting across the liquid layer.

Because the van der Waals force is very short ranged, the curvature of the substrate is negligible when the film is thin ($D\ll r_0$, the scale of the curvature). Therefore the disjoining pressure is given to lowest order by the previous expression, and even the first correction depends only on the local curvature of the substrate. To evaluate this correction, we can use a simpler coordinate system (see Fig. 29), rotating space so that the tangent plane to the substrate at the point of the substrate closest to $\mathbf{r}$ becomes horizontal. We take the point of tangency to be the origin of our new coordinates (ξ_1,ξ_2,ξ_3). In this coordinate system, $\mathbf{r}$ is the point $(\xi_1,\xi_2,\xi_3)=(0,0,D)$ (where D is the thickness of the film at $\mathbf{r}$). The rotated

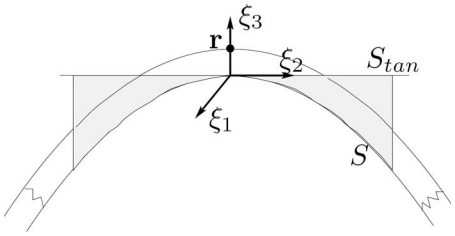

FIG. 29. The disjoining pressure is the interaction between $\mathbf{r}$ and the substrate, which is below the surface S in the figure. This can be calculated using the result for the interaction with an imaginary flat substrate (below the tangent plane S_{tan}) and subtracting the very narrow shaded region.

substrate can be described by its height relative to the new "horizontal plane" using the equation $\xi_3=h_{\mathrm{rot}}(\xi_1,\xi_2)$. The disjoining pressure is

$$\begin{aligned}p_{\mathrm{vdW}}(\mathbf{r})&=\int\int d\xi_1 d\xi_2\int_{-\infty}^{h_{\mathrm{rot}}(\xi_1,\xi_2)}d\xi_3\\&\quad\times w[\sqrt{\xi_1^2+\xi_2^2+(D-\xi_3)^2}]\\&=-\frac{\pi\alpha}{6D^3}-\int\int d\xi_1 d\xi_2\\&\quad\times\int_{h_{\mathrm{rot}}(\xi_1,\xi_2)}^{0}d\xi_3 w[\sqrt{\xi_1^2+\xi_2^2+(D-\xi_3)^2}],\end{aligned} \tag{C4}$$

where we have first integrated over the entire region below the plane $\xi_3=0$, thereby getting the van der Waals interaction between a point and a flat substrate as the first term. We then subtract the surplus energy that has been included by integrating over the shaded region (see Fig. 29).

Since the force is short ranged, we use the quadratic approximation to h_{rot}, $h_{\mathrm{rot}}(\xi_1,\xi_2)=-\xi_1^2\kappa_1/2-\xi_2^2\kappa_2/2$ where we have assumed the axes to be aligned with the principal curvatures. Finally since $\kappa_{1,2}D\ll 1$ this wedge-shaped region is extremely thin close to the origin and the remainder term can therefore be approximated by ignoring the dependence of w on ξ_3:

$$\begin{aligned}\Delta p_{\mathrm{vdW}}&=-\int\int d\xi_1 d\xi_2\left(\frac{\xi_1^2}{2}\kappa_1+\frac{\xi_2^2}{2}\kappa_2\right)\\&\quad\times w(\sqrt{\xi_1^2+\xi_2^2+D^2}).\end{aligned} \tag{C5}$$

This integral can be evaluated in polar coordinates,

$$\begin{aligned}\Delta p_{\mathrm{vdW}}&=\alpha\int\int\frac{rdrd\phi}{(r^2+D^2)^3}\left(\frac{\kappa_1}{2}r^2\cos^2\phi+\frac{\kappa_2}{2}r^2\sin^2\phi\right)\\&=\alpha\frac{\kappa_1+\kappa_2}{2}\pi\int_0^\infty\frac{r^3dr}{(r^2+D^2)^3}=\alpha\frac{H\pi}{4D^2},\end{aligned} \tag{C6}$$

since the mean curvature H is given by $\frac{1}{2}(\kappa_1+\kappa_2)$. Upon combining this expression with the flat substrate result, we obtain Eq. (70).

APPENDIX D: GUIDE TO GREEN'S FUNCTIONS ON COMPACT SURFACES

The ambiguity in the one-vortex energy [Eq. (147)] on the sphere also implies that there is no particularly natural choice of a Green's function on the sphere. With so many choices out there, you will be grateful for this consumer's guide to help you focus on the important features and possible pitfalls of these different functions.

The first point you need to know is that all of them work pretty much just as well, provided they are used consistently; one should not use the single-vortex energy equation (83) designed to work with a different Green's function from the one used to calculate the pair interaction equation (82). The general definition of a Green's function, broadened from Eq. (13), is that it is a symmetric function of two points on the deformed sphere satisfying the equation

$$\nabla_{\mathbf{x}}^2\Gamma(\mathbf{x},\mathbf{y}) = -\delta(\mathbf{x},\mathbf{y}) + F(\mathbf{x}). \tag{D1}$$

The only restriction on the function F is that its integral over the deformed sphere must equal 1. (Integrating the Laplacian on the left shows that there is no solution unless the right-hand side integrates to zero.) The Green's function on a sphere $-(1/2\pi)\ln[\mathcal{D}(\mathcal{X},\mathcal{Y})/a]$ has $1/4\pi-\delta(\mathcal{X},\mathcal{Y})$ as its Laplacian (Lubensky and Prost, 1992). Equation (D1) is a more versatile vision of what a Green's function should be, using a function F in place of the constant.

That Eqs. (83) and (82) give the correct net energy follows from the result proven in Sec. VI.A by conformal mapping to the unit sphere,

$$E(\{n_i,\mathbf{u}_i\}) = \sum_{i<j} 4\pi^2 K n_i n_j \Gamma_{\text{sphere}}(\mathcal{U}_i,\mathcal{U}_j) - \sum_i \pi K n_i^2 \omega(\mathbf{u}_i). \tag{D2}$$

The interaction potential in this equation

$$\Gamma_c(\mathbf{x},\mathbf{y}) = -\frac{1}{2\pi}\ln(|\mathcal{X}-\mathcal{Y}|/a) \tag{D3}$$

satisfies

$$\begin{aligned}\nabla_{\mathbf{u}}^2\Gamma_c(\mathbf{u},\mathbf{u}') &= e^{2\omega(\mathbf{u})}\nabla_{\mathcal{U}}^2\Gamma_{\text{sphere}}(\mathcal{U},\mathcal{U}')\\ &= e^{2\omega}\left[-\delta_R(\mathcal{U},\mathcal{U}') + \frac{1}{4\pi}\right]\\ &= -\delta_T(\mathbf{u},\mathbf{u}') + \frac{e^{2\omega(\mathbf{u})}}{4\pi}.\end{aligned} \tag{D4}$$

In the first step, the scale factor is introduced to compensate for the change from the reference to the target surface. In the second step, the Laplacian of the sphere's Green's function $-(1/2\pi)\ln(\mathcal{D}_{ij}/a)$ is substituted. In the third step, the δ function is transformed back to the target surface. The last line shows that Γ_c is a Green's function as set out by Eq. (D1), which we call the "conformal Green's function." The F function that goes with this Green's function gets its spatial dependence from the conformal factor.

The single-particle potential ω in Eq. (D2) satisfies

$$\nabla_{\mathbf{u}}^2\omega = G_T(\mathbf{u}) - e^{2\omega(\mathbf{u})}, \tag{D5}$$

which follows from Eq. (97) with the curvature of the unit sphere $G_R=1$ substituted.

Now any Green's function Γ can be used to solve Poisson's equation for any *net-neutral* function ρ on the target surface,

$$\nabla_{\mathbf{u}}^2\int\int d^2\mathbf{u}'\Gamma(\mathbf{u},\mathbf{u}')\rho(\mathbf{u}') = -\rho(\mathbf{u}). \tag{D6}$$

This follows from Eq. (D1). It can be used to relate the conformal Green's function to any other. We first use the Poisson-like integral to "solve" two special cases of Poisson's equation, Eqs. (D4) and (D5), in terms of the arbitrary Green's function Γ. Regarding $\mathbf{u}'$ as a constant in the former equation, we find that

$$\Gamma_c(\mathbf{u},\mathbf{u}') = \Gamma(\mathbf{u},\mathbf{u}') - \int\int d^2\mathbf{u}''\Gamma(\mathbf{u},\mathbf{u}'')\frac{e^{2\omega(\mathbf{u}'')}}{4\pi} + f(\mathbf{u}'), \tag{D7}$$

where $f(\mathbf{u}')$ is the constant left undetermined by the Poisson equation. Since both Γ and Γ_c are symmetric in $\mathbf{u},\mathbf{u}'$, $f(\mathbf{u}')=-\int\int d^2\mathbf{u}''\Gamma(\mathbf{u}',\mathbf{u}'')e^{2\omega(\mathbf{u}'')}/4\pi+C_1$, where C_1 is a constant. Again applying Eq. (D6), this time to Eq. (D5), implies that

$$\omega(\mathbf{u}) = -\int\int d^2\mathbf{u}''\Gamma(\mathbf{u},\mathbf{u}'')G_T(\mathbf{u}'') - 4\pi f(\mathbf{u}) + C_2. \tag{D8}$$

[This is not really a *solution* of the nonlinear equation (D5) since ω still appears on both sides of the equation.] Rewriting the previous equations implies that

$$\Gamma(\mathbf{u},\mathbf{u}') = \Gamma_c(\mathbf{u},\mathbf{u}') - f(\mathbf{u}) - f(\mathbf{u}') - C_1,$$

$$U_G(\mathbf{u}) = \omega(\mathbf{u}) + 4\pi f(\mathbf{u}) - C_2,$$

namely, U_G and Γ are related to ω and Γ_c according to the energy-shuffling transformation equation (147) so that the more general expressions of Eqs. (83) and (82) can be used in place of Eq. (D2) to determine the energy. The sum of the energies from Eqs. (83) and (82) is equal to the correct energy equation (D2) up to a constant. The arbitrary Green's function can also be used to find the flow pattern according to

$$\chi(\mathbf{u}) = \sum_{i=1}^{N}\frac{hn_i}{m}\Gamma(\mathbf{u},\mathbf{u}_i). \tag{D9}$$

There are some advantages and disadvantages of different choices for F in Eq. (D1). We focus on the most popular choices. The "standard Green's function" is defined as $F=1/A$ (A is the area of the surface) and is simply related to the eigenfunctions of the Laplacian, $\nabla^2\Psi_\lambda=-\lambda\Psi_\lambda$,

$$\Gamma_s(\mathbf{x},\mathbf{y}) = \sum_{\lambda\neq 0} \frac{1}{\lambda}\Psi_\lambda(\mathbf{x})^*\Psi_\lambda(\mathbf{y}). \tag{D10}$$

The "pair Green's function" is defined via conformal mapping,

$$\Gamma_p(\mathbf{x},\mathbf{y}) = \Gamma_{\text{sphere}}(\mathcal{X},\mathcal{Y}) + \frac{1}{4\pi}[\omega(\mathbf{x}) + \omega(\mathbf{y})] \tag{D11}$$

and incorporates the single-particle energy into the interaction energy, so that the corresponding geometric potential $U_p=0$. This Green's function satisfies the most elegant differential equation,

$$\nabla^2\Gamma_p(\mathbf{x},\mathbf{y}) = -\delta(\mathbf{x},\mathbf{y}) + G(\mathbf{x})/4\pi. \tag{D12}$$

Last, the "conformal Green's function" (which was our starting point) has $F=e^{2\omega}/4\pi$ [see Eq. (D2)].

If you are looking for style in your Green's functions, I would choose the pair Green's function. It is easy to calculate by conformal mapping [Eq. (D11)] but it can be defined without referring to ω, Eq. (D12), much preferable to the haphazard looking Eq. (D4) defining the conformal Green's function. The standard Green's function is stodgier and does not handle well. The methods for finding the standard Green's function, Eq. (D10), are more limited and, if one wants to use it, the best option might be to derive it using conformal mapping anyway,

$$\Gamma_s(\mathbf{x},\mathbf{y}) = \Gamma_c(\mathbf{x},\mathbf{y}) - \frac{1}{A_{\text{tot}}}\int\int \Gamma_c(\mathbf{x},\mathbf{u}) + \Gamma_c(\mathbf{y},\mathbf{u})d^2\mathbf{u} + C_3. \tag{D13}$$

[This equation is derived analogously to Eq. (D7).] On the other hand, there are always advantages to familiarity. In particular, in the limit where part of the deformed sphere is stretched out to infinity so that it actually becomes a deformed plane, Γ_s converges to the ordinary Green's function of a noncompact surface, since $1/A$ tends to zero. For a short summary of all these Green's functions features and failings, see Table II.

TABLE II. The advantages and disadvantages of the Green's functions, as far as their ease of calculation, simplicity of the neutralizing function F, and limiting behavior in case the deformed sphere is stretched into a deformed plane.

	Calculability	Neutralizer	Limit
Conformal	+	−	−
Pair	+	+	−
Standard	−	+	+

APPENDIX E: APPROXIMATIONS FOR LONG SURFACES OF REVOLUTION

We start by determining the conformal map from the surface of revolution defined by $r=r(z)$, $z_s \leqslant z \leqslant z_n$, to the unit sphere. We use the coordinates ϕ,σ introduced in Sec. VI.D to parametrize the surface; σ is given by

$$\sigma = \int_z^{z_n} \sqrt{1+(dr/dz)^2}dz. \tag{E1}$$

The Cartesian coordinates are $x=r(\sigma)\cos\phi$, $y=r(\sigma)\sin\phi$, $z=z(\sigma)$, and hence the metric is

$$ds^2 = dx^2 + dy^2 + dz^2 = d\sigma^2 + r(\sigma)^2 d\phi^2. \tag{E2}$$

If the map $(\sigma,\phi)\to(\Theta,\Phi)$ to the unit sphere is to be conformal, then according to Eq. (78)

$$d\sigma^2 + r(\sigma)^2 d\phi^2 = e^{-2\omega}(d\Theta^2 + \sin^2\Theta d\phi^2). \tag{E3}$$

By symmetry, $\Phi=\phi$ and $\Theta=\Theta(\sigma)$ and is independent of ϕ [see Vitelli and Nelson (2004) for the analogous use of symmetry on a rotationally symmetric bump on a plane]. By matching the coefficients of $d\phi$ and $d\sigma$ one finds that $d\sigma/r(\sigma)=d\Theta/\sin\Theta$, or (after integration)

$$\sin\Theta = \operatorname{sech}\left(\int_\sigma^{\sigma_0} \frac{d\sigma'}{r(\sigma')}\right), \tag{E4}$$

where σ_0 can be an arbitrary arc length; this is equivalent to Eq. (135). According to Eq. (E3), $\omega=\ln(d\Theta/d\sigma)$, or

$$\omega = \ln\frac{1}{r(\sigma)}\operatorname{sech}\int_\sigma^{\sigma_{\text{eq}}} \frac{d\sigma'}{r(\sigma')}. \tag{E5}$$

To determine the energies and flow patterns on a rotationally symmetric surface, we use the "pair Green's function" of Eq. (D11), the Green's function which incorporates all of the energy into interaction-energy terms. This Green's function can be found using Eqs. (E5) and (E4); adding ω at the sites of the vortices to the Green's function on the sphere,

$$\Gamma_c = -\frac{1}{2\pi}\ln\frac{1}{a}\sqrt{2[1-\cos\Theta_1\cos\Theta_2 - \sin\Theta_1\sin\Theta_2\cos(\Phi_1-\Phi_2)]},$$

and rearranging, gives

$$\Gamma_p = -\frac{1}{2\pi}\ln\sqrt{\frac{2r(\sigma_1)r(\sigma_2)}{a^2}}\left[\cosh\int_{\sigma_1}^{\sigma_2}\frac{d\sigma}{r} - \cos(\phi_1-\phi_2)\right]. \tag{E6}$$

The energy of a set of vortices is simple using the pair Green's function (see Appendix D), $E = \Sigma_{i<j} 4\pi^2 n_i n_j K \Gamma_{\text{pair}}(\mathbf{u}_i, \mathbf{u}_j)$. As an example the energy of a vortex-antivortex pair at opposite sides of a circle of latitude ($\phi_1 = \phi_2 + \pi$ and $\sigma_1 = \sigma_2 = \sigma$) is

$$E = 2\pi \ln[2r(\sigma)/a], \tag{E7}$$

showing that the energy grows logarithmically with the distance between the vortices in this case, as in Eq. (129).

To prove that the flows are approximately azimuthally symmetric, note that according to Eq. (D9) the flow velocity at $\mathbf{u}$ is

$$\mathbf{v} = \nabla_{\mathbf{u}} \sum_i \frac{n_i h}{m} \Gamma_p(\mathbf{u}, \mathbf{u}_i). \tag{E8}$$

Now if the vortices are all far from $\mathbf{u}$, then the integral in Eq. (E6) is very large. Since $\ln(A+\epsilon) \approx A + \epsilon/A$ for large A, the cosine term, the only one which depends on the azimuthal angles, gives exponentially small contributions. Therefore the flows can be calculated as in Sec. VI.D, using the circulation quantization and the approximate azimuthal symmetry to determine the flow speeds. Alternatively, we may calculate the velocity directly from Eq. (E6) with the help of the further approximation that $\cosh x \approx \frac{1}{2} e^{|x|}$, yielding

$$\Gamma(\mathbf{u}, \mathbf{u}_i) \approx -\frac{1}{4\pi} \left| \int_{\sigma}^{\sigma_i} \frac{d\sigma'}{r} \right| - \frac{1}{4\pi} \ln \frac{r(\sigma) r(\sigma_i)}{a^2}. \tag{E9}$$

The first term gives the flow pattern of Eq. (134), after a calculation using the neutrality constraint, while the second term, when summed as in Eq. (E6), cancels out also by neutrality.

For a surface (such as an ellipsoid) where the x-y plane is a plane of symmetry, our results will simplify if we make the choice $\sigma_0 = \sigma_{\text{eq}}$ in Eq. (E4), where σ_{eq} is the arclength corresponding to the equator, at $z=0$. In this case, the conformal map takes pairs of antipodal points on the deformed surface to antipodal points on the sphere. [Since antipodal points (σ_1, ϕ_1), (σ_2, ϕ_2) are points at opposite ends of a diameter of the surface, $\sigma_2 = 2\sigma_{\text{eq}} - \sigma_1, \phi_2 = \pi + \phi_1$.] If we consider the interaction energy of a pair of antipodal points, we find according to Eqs. (81) and (80)

$$E_{\text{antipodal}}/K = 2\pi \ln(2/a) - 2\pi\omega(z_1). \tag{E10}$$

Whether the two vortices are at opposite tips or at opposite ends of the equator, their image vortices are always at the same distance on the unit sphere, so the first term, the interaction energy of the images, is a constant. This gives another illustration of the folly of making a strict separation between intervortex and curvature-vortex interactions. One thinks that the growth of the energy as the two vortices are separated on an elongated surface is due to the attraction between them. But Eq. (E10) shows that it can also be interpreted as resulting from the single-particle potential ω.

We now turn to the problem of describing the equilibrium positions of a pair of vortices on a rotating ellipsoid. Both the transitions at Ω_a and Ω_b can be understood only with a more accurate version of the force than the band-force approximation, Eq. (132). The error in the approximation is important when the vortices are near the poles of the ellipsoid or near each other. We assume that the aspect ratio of the ellipsoid $\alpha = H/R$ is very large. The equation for the ellipsoid can be expressed in terms of α in the form

$$r = R\sqrt{1 - z^2/\alpha^2 R^2}. \tag{E11}$$

The energy of a vortex-antivortex pair according to Eq. (40) is

$$E = E_{\text{rest}} + E_{\Omega}. \tag{E12}$$

Here the energy of the flow pattern, or "resting energy," is the energy of the vortices on a stationary ellipsoid $E_{\text{rest}} = -4\pi^2 K \Gamma_{\text{pair}}(\sigma_1, \phi_1; \sigma_2, \phi_2)$. The "rotation energy" E_{Ω} is given by Eq. (137). Both energies are functions of a single variable, the distance s between the two vortices along the surface, if we assume that the vortices are at $(\sigma_1, \phi_1) = (\sigma_{\text{eq}} - s/2, 0)$ and $(\sigma_2, \phi_2) = (\sigma_{\text{eq}} + s/2, 0)$. These relationships assume that the vortices are situated symmetrically about the x-y plane; the vortices will have equal azimuthal angles in order to minimize the energy of the flow pattern.

The equilibrium position of a pair of vortices is determined by balancing the rotational force and resting force acting on one of them. The resting force F_{rest} on vortex 1 is derived from the kinetic energy of the flow pattern and is positive since it pulls the vortices toward each other in order to decrease the width of the band of moving fluid between them. The rotational force F_{rot} is negative since it pulls the vortices toward the poles of the ellipsoid (and away from each other) in order to increase the total angular momentum of the flow. At equilibrium the rotational and resting forces on the vortices balance, as we can see by differentiating Eq. (E12) to obtain $0 = dE_{\text{rest}}/ds + dE_{\Omega}/ds$ or equivalently

$$F_{\text{rest}}(s) = -F_{\Omega}(s), \tag{E13}$$

where F_{rest} and F_{Ω} are the resting and rotational forces on the vortices. (A calculation shows that the force on one of the vortices $-\partial E/\partial \sigma_1$ is equal to dE/ds, since the energy change produced by moving one vortex an infinitesimal distance is the same as the energy change produced by moving both vortices half the distance.) The equilibrium positions can be found by graphing F_{rest} and $-F_{\Omega}$ as in Fig. 30 and finding the intersection points.

The exact expression for the resting force can be found by differentiating Eq. (E6) to obtain

$$F_{\text{rest}} = \frac{\pi K}{r(\sigma_1)} \left(\coth \left[\int_{\sigma_1}^{\sigma_{\text{eq}}} \frac{d\sigma'}{r(\sigma')} \right] - \frac{1}{\sqrt{1 + (dz/dr)^2}} \right). \tag{E14}$$

The rotational force is given exactly by Eq. (138).

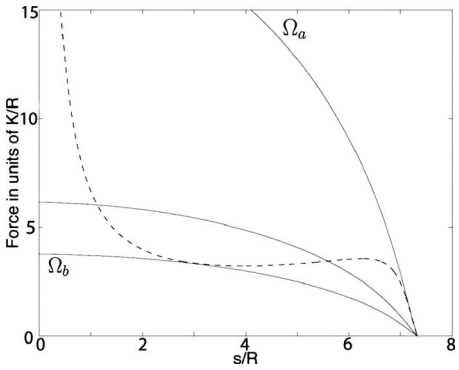

FIG. 30. The resting force (dashed line) and minus the rotational force (solid lines) between two vortices on an ellipsoid of aspect ratio 3.5. The rotational forces are shown for Ω_a (top curve), Ω_b (bottom curve), and an intermediate value of Ω. The vortex equilibrium positions are the intersection points. For smaller values of Ω, the attraction between the vortices always overcomes the rotational force, causing them to annihilate. For larger values of Ω, the rotational force overcomes the attraction, causing the vortices to move to opposite poles.

Figure 30 shows the resting force and minus the rotational force on one of the vortices for $\Omega=\Omega_b$, $\Omega=\Omega_a$ and for an intermediate value of the frequency.

Stability of the equilibria shown in Fig. 30 can be determined by considering the direction in which the resting force curve crosses the rotational force curve. The middle point of the three equilibrium points at the intermediate frequency is a stable equilibrium because the resting force curve crosses the rotational force curve from bottom to top. This implies that if the vortices fluctuate away from each other (increasing s), then the resting force becomes stronger than the rotational force and pulls them back together.

Consider how the stable equilibrium disappears at Ω_b. As Ω is lowered the stable and unstable equilibria come together and then "annihilate" when the rotation force curve detaches from the resting force curve, as shown by the lowest curve in Fig. 30, which corresponds to $\Omega=\Omega_b$. Since the rotation force and resting force curves are tangent at Ω_b, the frequency Ω_b and separation of the vortices s_b at this transition point can be determined by solving Eq. (E13) simultaneously with

$$F'_{\rm rest}(s_b) = -F'_{\Omega}(s_b). \tag{E15}$$

When $\alpha \gg 1$, we are able to avoid solving simultaneous equations since the value of Ω_b is already determined by Eq. (141). Using this result, we are able to solve Eq. (E15) for s_b.

The simple band approximation to the force, Eq. (132), suggests that the vortices move continuously toward one another as Ω is decreased, annihilating at the equator. Substituting the expression for the critical frequency that is implied by the band model, Eq. (141), into Eq. (140) in fact implies that $s_b=0$, which is incorrect. The band approximation fails because it implies that the force between the vortices decreases *monotonically* as the vortices approach one another. Though in conflict with our intuition from the plane, this result is correct over the large middle range of the resting force curve in Fig. 30. In this range weakening the rotational confinement allows the vortices to get closer together, and the resting force weakens too, preserving the equilibrium. However, the resting force starts *increasing* strongly as the vortices approach one another, because the vortices start to feel one anothers' asymmetric flow fields. This force will certainly overcome the rotational force when the rotational confinement decreases further. [Actually, Eq. (E15) implies that s_b does not correspond exactly to the maximum of $F_{\rm rest}$ because the rotational confinement is not a constant force field.]

We can derive the corrections to the force from Eq. (E14); if α is large, we may neglect the second term and assume that

$$\int_{\sigma_1}^{\sigma_{\rm eq}} \frac{d\sigma'}{r(\sigma')} \approx \frac{\sigma_{\rm eq}-\sigma_1}{R} \tag{E16}$$

since the radial profile of the ellipsoid, Eq. (E11), is slowly varying. We then obtain the approximation that is valid when the vortices are close (compared to r/r', the characteristic distance for variation of the radius),

$$F_{\rm rest} \approx [\pi K/r(\sigma_1)]\coth(s/2R). \tag{E17}$$

Notice that the force diverges as $2\pi K/s$ when the vortices are close together (as in the plane) and approaches Eq. (132) exponentially fast as the vortices move apart; this generalizes the band model approximation to the case where the two vortices may be close together. As we will see, for a large value of α, $s_b \gg R$ at the moment when the vortices annihilate. We therefore simplify Eq. (E17) by making another approximation, $\coth x \approx 1+2e^{-2x}$. Then an approximate version of Eq. (E15) that is derived from Eqs. (E17) and (138) reads

$$\frac{\pi K}{2}\frac{1}{R^2}\frac{dr}{d\sigma_1}\bigg|_{s_b} - 2\pi K\frac{e^{-s_b/R}}{R^2} = -\frac{\pi\Omega_b\hbar\rho_s}{m}\frac{dr}{d\sigma_1}\bigg|_{s_b}. \tag{E18}$$

The first term describes the decrease of the resting force due to the variation in $r(z)$. The second term results from the exponentially decaying portions of the flow fields. [We are replacing $r(\sigma_1)$ by R whenever that is accurate enough since the width of the ellipsoid is slowly varying. Of course, the slow variation of $r(\sigma_1)$ is important in some terms; the resting force initially decreases as s decreases because the band approximation to the force decreases with increasing circumference.] Using Eq. (141) for Ω_b in Eq. (E18) gives

$$\frac{dr}{d\sigma_1}\bigg|_{s_b} = 2e^{-s_b/R}. \tag{E19}$$

In order to evaluate the left-hand side for the ellipsoid, we note that $\sigma_1=\sigma_{\rm eq}-s/2\approx\sigma_{\rm eq}-z$ aside from terms of order $1/\alpha^2$ since the sides of the ellipsoid are nearly vertical near the equator. Therefore Eq. (E11) implies that $dr/d\sigma_1=s_b/2\alpha^2R$.

Rearranging Eq. (E19) now gives

$$s_b = R \ln(4\alpha^2 R/s_b), \tag{E20}$$

which can be solved by substituting it into itself. The first iteration gives

$$s_b = R \ln 4\alpha^2 - R \ln \ln(4\alpha^2 R/s_b). \tag{E21}$$

Since the second term has two logarithms in it, it is smaller than the first in the limit where $\alpha \to \infty$, so finally

$$z_b \approx R \ln \alpha. \tag{E22}$$

We have justified Eq. (142). Two iterations of Eq. (E20) give $z_b = R \ln \alpha - \frac{1}{2} \ln(\ln \alpha/2)$; the error for this approximation actually approaches 0 for large α. The exact result can be found by computer, but the approximate result is reasonable even at $\alpha=5$, where $z_b/R = 1.8 \approx \ln 5 = 1.6$.

The height z_b depends only logarithmically on α because the extra short-distance vortex-vortex interaction decays exponentially and would not be strong enough to pull the vortices together if z_b were very large. [Check this by substituting our final result, Eq. (E22), into Eq. (E18). All the terms, the ones from the band model as well as the exponential correction, have the same basic dependence on α.] To see that the approximations we have made are valid, one has to calculate $F'_{\text{rest}}(s)$ from the exact expression (E14). The resulting expression can be simplified by dropping various terms, which mostly have a relative size of $1/\alpha^2$ and $(\ln \alpha/\alpha)^2$; the reason is that $z_b/H = \ln \alpha/\alpha$ so the vortices are proportionally very close to the equator, and again $r(z)$ can be replaced by R. [This also justifies the approximation in Eq. (E16) where the integrand is replaced by a constant.] One particularly large term, resulting from the second term of Eq. (E14), has been neglected in Eq. (E18), but the neglected term, $K\pi r''(\sigma_1)/2r(\sigma_1)$, is still of relative order $1/\ln \alpha$.

Now we turn to the critical frequency Ω_a where the vortices move to the poles. The band model also requires a correction in order for this transition to be described correctly. In fact, Eq. (140) would imply that the vortices never exactly reach the tips of the ellipsoid even as $\Omega \to \infty$, and thus $\Omega_a = \infty$. In fact, the band force on the left-hand side of Eq. (139), which approaches infinity at the poles, cannot be balanced by the rotational force at a finite frequency. Of course, the exact force approaches zero rather than infinity at the pole (see Fig. 30). The value of Ω_a may be derived from the condition that the actual resting force curve and the rotation force curve have to be tangent at the origin, as for the uppermost ($\Omega = \Omega_a$) curve in Fig. 30. We therefore have to find when $s = 2\sigma_{\text{eq}}$ satisfies Eq. (E15). Linearizing Eq. (E14) near $\sigma_1 = 0$ to find the derivative of the force implies that Ω_a is given by

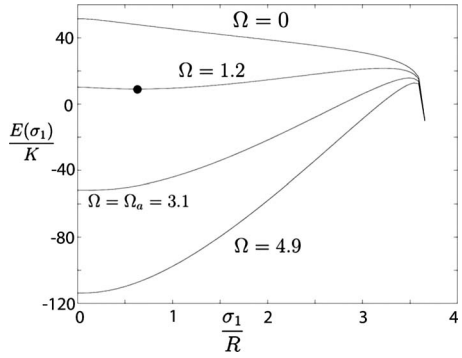

FIG. 31. Illustration of the combined rotational and resting energies for different frequencies Ω and $H = 3.5R$. The second curve corresponds to a frequency greater than Ω_b, the frequency where the rotation keeps vortices from annihilating. Although it looks practically flat on this scale, the energy has a curvature of about $10K/R^2$ at the off-center equilibrium position indicated. The third curve corresponds to $\Omega = \Omega_a$, where the vortices are first pushed to the ends of the ellipsoids. The angular frequencies are given in units of $\hbar/mR^2$.

$$\frac{m\Omega_a}{\hbar} = \frac{\kappa^2}{4} + \frac{1}{R^2} \exp\left[-2 \int_0^R \left(\frac{d\sigma}{dr} - 1 \right) \frac{dr}{r} \right], \tag{E23}$$

where κ is the curvature at the tip of the ellipsoid. The critical frequency is larger than the result $\hbar\kappa^2/4m$, derived in Sec. IV.B, for a bump with the same curvature because the rotational confinement must overcome the mutual attraction of the vortices as well as the repulsion of the vortices from the curvature. For an ellipsoid with a large value of α, the correction term is unimportant, so

$$\Omega_a \approx \alpha^2 \hbar/4mR^2. \tag{E24}$$

The transition can be visualized using the energy curves shown in Fig. 31, where the local minimum of the energy function moves away from the axis as Ω is decreased through Ω_a.

There is an aspect ratio α_c below which there are no off-center local minima, for any rotation speed. That is, when the angular velocity is decreased enough, a vortex-antivortex pair initially at the poles *immediately* moves to the equator and annihilates. This situation is shown for a sphere in Fig. 32. The value of α_c can be determined numerically, and is 1.33. One simply graphs the total energy at $\Omega = \Omega_a$ [as given by the exact expression, Eq. (E23)] and checks whether there is an energy barrier or not. At $\Omega > \Omega_a$, a pair of vortices at the poles will be stable. If there is no barrier, as in Fig. 32, slightly decreasing Ω will cause these vortices to leave the poles and annihilate each other. If there is a barrier, as in Fig. 31, slightly decreasing Ω will create an off-center local minimum. This can be seen from the energy curves: there is a local maximum at the origin, because $\Omega < \Omega_a$, and there is also a local maximum at the top of the barrier. Therefore the vortex can find a local minimum somewhere in between.

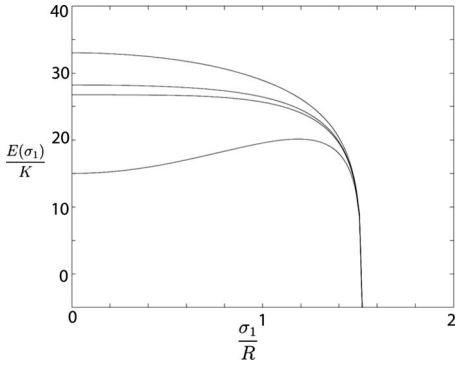

FIG. 32. The combined rotational and kinetic energy for vortices on a sphere, where there are no stable off-axis positions. The energy is graphed as a function of $\sigma_1=\sigma_{\rm eq}-s/2$. From the top, the curves correspond to $\Omega=0,0.4\hbar/mR^2,0.52\hbar/mR^2,1.5\hbar/mR^2$. The third of these corresponds to $\Omega=\Omega_a=\Omega_b$. In the last curve, the vortices are trapped near $\sigma_1=0$ (i.e., at the poles) by the rotational energy.

APPENDIX F: DERIVATIONS OF BOUNDS VALID EVEN FOR STRONG DISTORTIONS

The results of Sec. VII can be derived from theorems on "univalent" analytic functions. We state these theorems here and derive the limits on the geometric force from them [see Rudin (1987) for the proofs]. An abstract example of the type of question these theorems address is the following. Let $f(t)$ be an analytic function defined by the following series:

$$f(t)=t+a_2t^2+a_3t^3+\cdots. \tag{F1}$$

Suppose this series converges out to radius 1, at least. If one of the coefficients, maybe a_6, is much larger than the rest, then the function is dominated by the t^6 behavior, and most points in the range of the function will occur six times as values of the function. Therefore, if one is looking for a univalent function (a function which is one to one inside the unit circle), then there will be upper limits on the sizes of the a_n. A challenging mathematical problem is: What are the maximum sizes for the a_n's? The answer (proved by De Branges, 1985) is that if f is univalent inside the unit circle, then $|a_n|\leqslant n$, and that the function $t/(1-t)^2$ attains the maximum value for every Taylor series coefficient simultaneously. To find the upper bound on the vortex force in a flat disk, we use only the bound

$$a_2\leqslant 2, \tag{F2}$$

which has a simpler proof (Rudin, 1987). Note that the conditions of this theorem do not assume that the function remains one to one *outside* the unit circle. For example, the function $t+0.1t^2$ satisfies the univalency condition of the theorem although it takes on the value zero at $t=0,-10$. The analyticity of $f(t)$ is allowed to break down as well beyond a radius of 1.

Similar problems can be stated for functions $g(t)$ defined outside of the unit circle, with expansions of the form

$$g(t)=t+b_1/t+b_2/t^2+\cdots. \tag{F3}$$

To make the predictions about the quadrupole force due to a bump in a plane we use the area theorem (Rudin, 1987), which states that if g is one to one and analytic outside the unit circle, and

$$g(t)=t+a_1/t+\cdots, \tag{F4}$$

then

$$a_1\leqslant 1. \tag{F5}$$

To prove Eq. (159), one realizes that the assumption means that a part of the surface has the same geometry as a radius R disk in the plane with a vortex at the center. We introduce a coordinate system on this portion of the surface by introducing Cartesian coordinates u,v (with $w=u+iv$) on the disk in the plane, and then mapping these coordinates isometrically to the surface. This mapping is different from the conformal mapping C used to calculate vortex energies. To relate them, let $\mathcal{Z}=\mathcal{X}+i\mathcal{Y}$, where $\mathcal{X},\mathcal{Y}$ are the coordinates of the conformal image of the surface. Then Eq. (78) takes the form $du^2+dv^2=e^{-2\omega}(d\mathcal{X}^2+d\mathcal{Y}^2)$ and it follows that $\mathcal{Z}(w)$ is a conformal map from a portion of the plane to itself, hence an analytic function of w on the circle of radius R (say, $\mathcal{Z}=c_1w+c_2w^2+\cdots$). Furthermore, rewriting the expression for the scaling of lengths as $|dw|^2=e^{-2\omega}|d\mathcal{Z}|^2$, we see that

$$\omega=\ln|d\mathcal{Z}/dw|. \tag{F6}$$

We now define

$$f(t)=[\mathcal{Z}(Rt)-\mathcal{Z}(0)]/Rc_1.$$

Then f is a one-to-one analytic function on the unit circle (which is scaled by $t\to Rt$ into the radius R circle). Since $f(0)=0$, $f'(0)=1$, f has the form of Eq. (F1), so Eq. (F2) implies

$$2\geqslant R|c_2/c_1|. \tag{F7}$$

Now the force on the vortex is $\pi K\nabla\omega(0)$ which can be expressed in terms of the coefficients of $\mathcal{Z}$'s Taylor series by means of Eq. (F6): $\mathbf{F}=2\pi K(\Re c_2/c_1,-\Im c_2/c_1)$. The upper bound, Eq. (159), follows from Eq. (F7).

We now see whether the bound just proven can be improved at all; i.e., whether the ratio of the force on a singly quantized vortex to K/R can ever be as large as 4π. For example, for vortices on cones, the ratio of the force to K/R is maximal in the limit where the cone angle $\theta\to 0$. To find this ratio, we must take R to be the radius of a disk centered at the vortex which is *flat* and *non-self-intersecting*; taking $R=R_{\rm max}$, the radius of a disk, which is as large as possible, maximizes the ratio we are interested in. The radius $R_{\rm max}$ can be found by imagining the disk expanding out from the vortex. If $\theta>\pi$, $R_{\rm max}=D$ because the first calamity that befalls the disk as it expands is that it starts overlapping the cone's apex. But if $\theta<\pi$, then the disk overlaps itself before this as one can see on the unfolded version of the cone shown in Fig. 33. Some simple trigonometry shows that

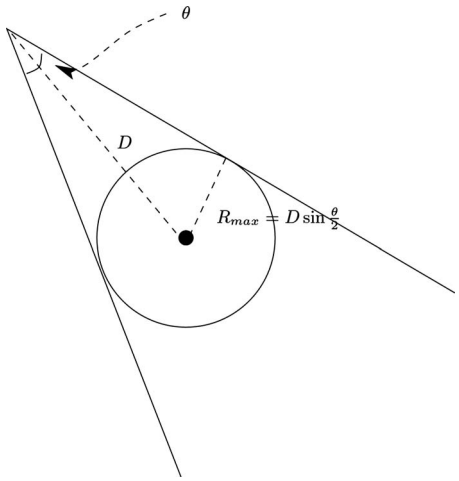

FIG. 33. Construction of the largest circle centered at a point on a cone with $\theta < \pi$. The cone is cut open and flattened so that the center is on the bisector of the angle.

$R_{\max} = D \sin \theta/2$. Equation (162) shows that, for small θ, $|\mathbf{F}|R/K \to \pi^2$, which is a little less than 4π.

There is a surface that saturates the original bound, though; this surface is shown in Fig. 34. The surface is obtained by folding a disk in half and sealing it shut except for a very small opening at one end of the diameter. This opening is then connected to an infinite plane. The top part of the substrate is a semicircular slab with the superfluid layer laminating both sides so that the helium spreads out to the plane. The topology of the helium film is still that of a plane.

A vortex placed at the center of the disk B saturates the bound; it is attracted by the negative curvature of the neck joining the plane and the disk and is repelled by the positive curvature at the top of the fold.

To show that this surface (the "calzone surface") saturates the bound, we find the force on the vortex using conformal mapping. Instead of mapping the entire surface to a reference plane, we can just map the folded disk portion of the surface. The flow patterns on the two portions of the surface are uncorrelated when the neck

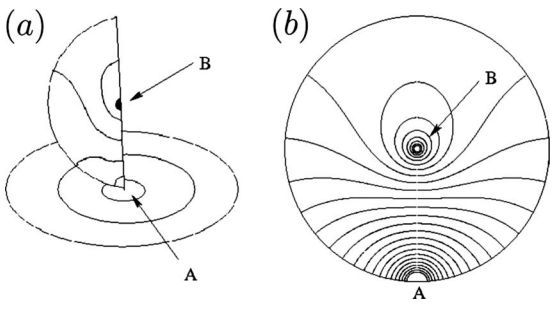

FIG. 34. A surface with the maximum geometric force. (a) The surface which contains an isometric disk of radius R and has the maximum geometrical force. A semicircle (with films on both sides) is connected by a neck A to a plane. If a single vortex is placed at B, the force on the vortex approaches $4\pi K/R$ as the edges of the surface become sharper. (b) An unfolded image of the flow pattern.

becomes infinitely small, aside from requirements imposed by the circulation's invariance. The circulation around any curve on the plane enclosing the neck will be h/m because the vortex in the disk region is inside it, and the flow pattern on the planar base will not be sensitive to the location of this vortex because the neck is so narrow. It will consist of a set of concentric circles, representing a flow whose energy is independent of the position of the vortex. The force does not depend on this portion of the flow, so the two portions may be dismantled at the neck. As shown in Fig. 34, the neck now turns into the core of a second vortex, at point A of the folded disk. The folded disk now has the topology of a sphere, satisfying the neutrality condition because the two vortices are equal and opposite. The map $\mathcal{Z} = R^2 iw/(R-iw)^2$ on the radius R disk can be used to relate the folded disk to a reference plane, since the points on the circle which fold together, $w = iRe^{\pm i\phi}$, both map to the same point of the real axis in the plane. Since the vortex at A maps to infinity, the force on the vortex at B can be calculated from the geometric potential alone (without any interaction terms), giving $\pi K \mathcal{Z}''^*(0)/\mathcal{Z}'^*(0) = -4\pi i K/R$. Also the flow pattern shown in the figure can be found by mapping the concentric circles centered around the origin in the $\mathcal{Z}$ plane to the disk using the function $w(\mathcal{Z})$.

The result Eq. (164) about the long-range force due to a bump contained inside of a radius R but with an arbitrary height and arbitrary curvatures follows (by an argument similar to the one used for the first inequality) from Eq. (F10). The conformal mapping takes the flat part of the surface (a plane with a radius R hole parametrized by the complex variable w) in a one-to-one fashion to a reference plane with a hole of some distorted shape. As above, this function is analytic and $\omega = \ln|d\mathcal{Z}/dw|$. By rescaling one can ensure that $\mathcal{Z} \sim w$ at infinity. Applying the area theorem to $g(t) = \mathcal{Z}(Rt)/R$ shows that

$$\mathcal{Z}(w) = w + R^2 a_1/w + \cdots, \tag{F8}$$

where $a_1 \leqslant 1$. Expand $E = (\pi K/2)\Re \ln(d\mathcal{Z}/dw)$ for large w to find the large distance form of the energy,

$$E \sim -\pi K R^2 \Re a_1/w^2. \tag{F9}$$

It follows that $\mu_2 = \pi K R^2 |a_1|$ and $\gamma_2 = \arg(a_1) + \pi$ in Eq. (163) and the bound on the quadrupole moment $\mu_2 \leqslant \pi K R^2$ follows from the bound on a_1.

Now we can also ask what type of bump maximizes the quadrupole moment. It turns out that the value $\pi K R^2$ cannot be attained by any surface which is flat outside a circle of radius R. There is a surface which consists of a bump surrounded by a surface *isometric* but not *congruent* to K_R, the plane with a circle of radius R removed. This surface is gotten from K_R by sealing opposite sides of the circle together to make a mountain ridge. The curved portion of this surface is an infinitely thin curve.

The reason this surface has the largest quadrupole moment is because its conformal mapping to the plane is

the function that maximizes a_1. According to the area theorem the only one-to-one analytic function on K_R for which $a_1=1$ is

$$\mathcal{Z}(w) = w + R^2/w. \tag{F10}$$

This function maps both points $Re^{\pm i\phi}$ to the same point in the reference plane, so any flow pattern on the target plane will still be continuous when the two edges of K_R are sealed.

This quadrupole-maximizing surface does not contain a flat copy of K. Hence an open question is to find the largest value of μ_2 for a bump in a plane which is actually flat outside a radius of R, as well as the shape of the bump which has this maximum quadrupole moment.

REFERENCES

Achard, M. F., M. Kleman, Y. A. Nastishin, and H. T. Nguyen, 2005, Eur. Phys. J. E **16**, 37.

Ambegaokar, V., B. I. Halperin, D. R. Nelson, and E. D. Siggia, 1978, Phys. Rev. Lett. **40**, 783.

Andelman, D., J. F. Joanny, and M. O. Robbins, 1988, Europhys. Lett. **7**, 731.

Antoniadis, I., P. O. Mazur, and E. Mottola, 2007, New J. Phys. **9**, 11.

Aronovitz, J. A., and T. C. Lubensky, 1988, Phys. Rev. Lett. **60**, 2634.

Atanasov, V., and R. Dandoloff, 2008, Phys. Lett. A **371**, 118.

Barenghi, C. F., R. Hanninen, and M. Tsubota, 2006, Phys. Rev. E **74**, 046303.

Batchelor, G. K., 2001, *An Introduction to Fluid Dynamics* (Cambridge University Press, Cambridge).

Bausch, A. R., M. J. Bowick, A. Cacciuto, A. D. Dinsmore, M. F. Hsu, D. R. Nelson, M. G. Nikolaides, A. Travesset, and D. A. Weitz, 2003, Science **299**, 1716.

Berezinskii, V. L., 1971, Sov. Phys. JETP **34**, 493.

Birrell, N. D., and P. C. W. Davies, 1982, *Quantum Fields in Curved Space* (Cambridge University Press, Cambridge).

Blanc, C., and M. Kleman, 2001, Eur. Phys. J. E **4**, 241.

Bowick, M. J., and L. Giomi, 2009, Adv. Phys. **58**, 449.

Bowick, M., D. R. Nelson, and A. Travesset, 2000, Phys. Rev. B **62**, 8738.

Bowick, M., D. R. Nelson, and A. Travesset, 2004, Phys. Rev. E **69**, 041102.

Bowick, M., and A. Travesset, 2001, Phys. Rep. **344**, 255.

Campbell, L. J., and R. M. Ziff, 1979, Phys. Rev. B **20**, 1886.

Capper, D. M., and M. J. Duff, 1974, Nuovo Cimento A **23**, 173.

Caspar, D., and A. Klug, 1963, in *Basic Mechanisms in Animal Virus Biology*, Cold Spring Harbor Symposia on Quantitative Biology XXVII (Long Island Biological Association, New York).

Cerda, E., and L. Mahadevan, 2005, Proc. R. Soc. London, Ser. A **461**, 671.

Chantawansri, T. L., A. W. Bosse, A. Hexemer, H. D. Ceniceros, C. J. Garcia-Cervera, E. J. Kramer, and G. H. Fredrickson, 2007, Phys. Rev. E **75**, 031802.

Chen, Bryan Gin-ge, and Randall D. Kamien, 2009, Eur. Phys. J. E **28**, 315.

Christensen, S. M., and S. Fulling, 1977, Phys. Rev. D **15**, 2088.

Cole, M. W., 1974, Rev. Mod. Phys. **46**, 451.

da Costa, R. C. T., 1981, Phys. Rev. A **23**, 1982.

David, F., 1989, in *Statistical Mechanics of Membranes and Surfaces*, edited by Nelson, D. R., S. Weinberg, and T. Piran (World Scientific, Singapore).

David, F., E. Guitter, and L. Peliti, 1987, J. Phys. (Paris) **48**, 2059.

De Branges, L., 1985, Acta Math. **154**, 137.

de Gennes, Pierre-Gilles, Françoise Brochard-Wyart, and David Quéré, 2004, *Capillarity and Wetting Phenomena: Drops, Bubbles, Pearls, Waves* (Springer, New York).

de Gennes, P.-G., and C. Taupin, 1982, J. Phys. Chem. **86**, 2294.

Derjaguin, B. V., 1940, Trans. Faraday Soc. **35**, 203.

DeVries, G. A., M. Brunnbauer, Y. Hu, A. M. Jackson, B. Long, B. T. Neltner, O. Uzun, B. H. Wunsch, and F. Stellacci, 2007, Science **315**, 358.

Dinsmore, A. D., M. F. Hsu, M. G. Nikolaides, M. Marquez, A. R. Bausch, and D. A. Weitz, 2002, Science **298**, 1006.

D'Inverno, Ray, 1992, *Introducing Einstein's Relativity* (Clarendon, Oxford).

Dodgson, M. J. W., and M. A. Moore, 1997, Phys. Rev. B **55**, 3816.

Duan, X., C. Nui, V. Sahi, J. Chen, J. W. Parce, S. Empedocles, and J. L. Goldman, 2003, Nature (London) **425**, 274.

Dubrovin, B. A., A. Fomenko, and S. P. Novikov, 1992, *Modern Geometry—Methods and Applications* (Springer-Verlag, New York), Vol. 1.

Duplantier, B., 1989, Phys. Rev. Lett. **62**, 2337.

Earnshaw, S., 1842, Proc. Cambridge Philos. Soc. **7**, 97.

Entin, M. V., and L. I. Magarill, 2001, Phys. Rev. B **64**, 085330.

Evans, D. Fennell, and Håkan Wennerström, 1999, *The Colloidal Domain: Where Physics, Chemistry, Biology and Technology Meet* (Wiley, New York).

Evans, R. M. L., 1996, Phys. Rev. E **53**, 935.

Fernandez-Nieves, A., V. Vitelli, A. Utada, D. R. Link, D. R. Nelson, and D. A. Weitz, 2007, Phys. Rev. Lett. **99**, 157801.

Frank, J. R., and M. Kardar, 2008, Phys. Rev. E **77**, 041705.

Ganser, B. K., S. Li, V. Y. Klishko, J. T. Finch, and W. I. Sundquist, 1999, Science **283**, 80.

Giomi, L., and M. J. Bowick, 2007, Phys. Rev. B **76**, 054106.

Giomi, L., and M. J. Bowick, 2008, Phys. Rev. E **78**, 010601(R).

Glaberson, W. I., and R. J. Donnelly, 1966, Phys. Rev. **141**, 208.

Gompper, G., and D. M. Kroll, 1997, Phys. Rev. Lett. **78**, 2859.

Guyon, E., J. P. Hulin, L. Petit, and C. D. Mitescu, 2001, *Physical Hydrodynamics* (Oxford University Press, Oxford).

Halperin, B. I., 2004, private communication.

Halperin, B. I., and D. R. Nelson, 1978, Phys. Rev. Lett. **41**, 121.

Han, Y., Y. Shokef, A. M. Alsayed, P. Yunker, T. C. Lubensky, and A. G. Yodh, 2008, Nature (London) **456**, 898.

Hashimoto, N., R. Goto, H. Yano, K. Obara, O. Ishikawa, and T. Hata, 2007, Phys. Rev. B **76**, 020504.

Helfrich, W., 1985, J. Phys. (Paris) **46**, 1263.

Hexemer, A., 2006, Ph.D. thesis (University of California, Santa Barbara).

Hexemer, A., V. Vitelli, E. J. Kramer, and G. H. Fredrickson, 2007, Phys. Rev. E **76**, 051604.

Hyde, S., K. Larsson, Z. Blum, T. Landh, S. Lidin, B. W. Ninham, and S. Andersson, 1997, *The Language of Shape* (Elsevier, Amsterdam).

Irvine, W. T. M., S. Sacanna, Y. Roichman, A. D. Hollingsworth, M. T. Elsesser, M. Bowick, D. G. Grier, and P. M. Chaikin, 2009, APS March Meeting Communication.

Jeans, J. H., 1927, *The Mathematical Theory of Electricity and*

Magnetism, 5th ed. (Cambridge University Press, Cambridge).
Jiang, H. Y., G. Huber, R. A. Pelcovits, and T. R. Powers, 2007, Phys. Rev. E **76**, 031908.
Kamien, R., 2002, Rev. Mod. Phys. **74**, 953.
Kantor, Y., M. Kardar, and D. R. Nelson, 1987, Phys. Rev. A **35**, 3056.
Katifori, E., E. Cerda, D. R. Nelson, and J. Dumais, 2010, Proc. Natl. Acad. Sci. U.S.A. (to be published).
Kleman, M., 1987, Phys. Scr. **T19**, 565.
Kleman, M., and J. Friedel, 2008, Rev. Mod. Phys. **80**, 61.
Kohyama, T., and G. Gompper, 2003, Phys. Rev. Lett. **98**, 198101.
Kohyama, T., D. M. Kroll, and G. Gompper, 2003, Phys. Rev. E **68**, 061905.
Kosterlitz, J. M., and D. J. Thouless, 1973, J. Phys. C **6**, 1181.
Li, S., C. P. Hill, W. I. Sundquist, and J. T. Finch, 2000, Nature (London) **407**, 409.
Libal, A., C. Reichhardt, and C. J. Olson Reichhardt, 2006, Phys. Rev. Lett. **97**, 228302.
Lidmar, J., L. Mirny, and D. R. Nelson, 2003, Phys. Rev. E **68**, 051910.
Lubensky, T. C., and J. Prost, 1992, J. Phys. II **2**, 371.
MacKintosh, F. C., and T. C. Lubensky, 1991, Phys. Rev. Lett. **67**, 1169.
Maradudin, A., and P. Mazur, 1980, Phys. Rev. B **22**, 1677.
Mazur, P., and A. Maradudin, 1981, Phys. Rev. B **23**, 695.
McMahon, H. T., and J. L. Gallop, 2005, Nature (London) **438**, 590.
Modes, Carl D., and Randall D. Kamien, 2007, Phys. Rev. Lett. **99**, 235701.
Modes, Carl D., and Randall D. Kamien, 2008, Phys. Rev. E **77**, 041125.
Moessner, R., and A. P. Ramirez, 2006, Phys. Today **59** (2), 24.
Needham, Tristan, 2000, *Visual Complex Analysis* (Clarendon, Oxford).
Nelson, D. R., 1983, Phys. Rev. B **28**, 5515.
Nelson, D. R., 2002a, Nano Lett. **2**, 1125.
Nelson, D. R., 2002b, *Defects and Geometry in Condensed Matter Physics* (Cambridge University Press, Cambridge).
Nelson, D. R., and J. M. Kosterlitz, 1977, Phys. Rev. Lett. **39**, 1201.
Nelson, D. R., and L. Peliti, 1987, J. Phys. (Paris) **48**, 1085.
Nemirovskii, S. K., and W. Fiszdon, 1995, Rev. Mod. Phys. **67**, 37.
Nguyen, T. T., R. F. Bruinsma, and W. M. Gelbart, 2005, Phys. Rev. E **72**, 051923.
Ovrut, B. A., and S. Thomas, 1991, Phys. Rev. D **43**, 1314.
Park, J.-M., and T. C. Lubensky, 1996, Phys. Rev. E **53**, 2648.
Pearl, J., 1964, Appl. Phys. Lett. **5**, 65.
Peliti, L., and S. Leibler, 1985, Phys. Rev. Lett. **54**, 1690.
Pérez-Garrido, A., M. J. W. Dodgson, and M. A. Moore, 1997, Phys. Rev. B **56**, 3640.
Polyakov, A. M., 1981, Phys. Lett. B **103**, 207.
Polyakov, A. M., 1987, *Gauge Fields and Strings* (Harwood Academic, Chur, Switzerland).
Pomeau, Y., 1998, Philos. Mag. B **78**, 235.
Qi, Y., T. Brintlinger, and J. Cumings, 2008, Phys. Rev. B **77**, 094418.
Quéré, D., J. M. di Meglio, and F. Brochard-Wyart, 1989, Europhys. Lett. **10**, 335.
Ramirez, A. P., 2005, MRS Bull. **30**, 447.
Ricca, R. L., D. C. Samuels, and C. F. Barenghi, 1999, J. Fluid Mech. **391**, 29.
Rudin, W., 1987, *Real and Complex Analysis*, 3rd ed. (McGraw-Hill, New York).
Sabisky, E. S., and C. H. Anderson, 1973, Phys. Rev. A **7**, 790.
Sachdev, S., and D. R. Nelson, 1984, J. Phys. C **17**, 5473.
Sadoc, Jean-François, and Rémy Mosseri, 2006, *Geometrical Frustration* (Cambridge University Press, Cambridge).
Saffman, P. G., 1992, *Vortex Dynamics* (Cambridge University Press, Cambridge).
Salomaa, M. M., and G. A. Williams, 1981, Phys. Rev. Lett. **47**, 1730.
Santangelo, C., V. Vitelli, R. D. Kamien, and D. R. Nelson, 2007, Phys. Rev. Lett. **99**, 017801.
Schwarz, K. W., 1981, Phys. Rev. Lett. **47**, 251.
Schwarz, K. W., 1990, Phys. Rev. Lett. **64**, 1130.
Scott, W. T., 1959, Am. J. Phys. **27**, 418.
Seung, S., and D. R. Nelson, 1988, Phys. Rev. A **38**, 1005.
Shin, H., M. J. Bowick, and X. Xing, 2008, Phys. Rev. Lett. **101**, 037802.
Subramaniam, A. B., M. Abkarian, and H. A. Stone, 2005, Nature Mater. **4**, 553.
Tanda, S., T. Tsuneta, Y. Okajima, K. Inagaki, K. Yamaya, and H. Hatakenaka, 2002, Nature (London) **417**, 397.
Tarjus, G., S. A. Kivelson, Z. Nussinov, and P. Viot, 2005, J. Phys.: Condens. Matter **17**, R1143.
Tempere, J., I. F. Silvera, and J. T. Devreese, 2001, Phys. Rev. Lett. **87**, 275301.
Tilley, D. R., and J. Tilley, 1990, *Superfluidity and Superconductivity*, 3rd ed. (IOP, Bristol).
Tinkham, M., 1996, *Superconductivity* (McGraw-Hill, New York).
Toulouse, G., 1977, Commun. Phys. (London) **2**, 115.
Trugman, Stuart, 2004, private communication.
Vinen, W. F., 1958, Proc. R. Soc. London, Ser. A **243**, 400.
Vinen, W. F., 1963, *Proceedings of the International School of Physics "Enrico Fermi," Course XXI: Liquid Helium* (Academic, New York).
Vinen, W. F., 1969, in *Superconductivity*, edited by R. D. Parks (Dekker, New York), Vol. 2.
Vitelli, V., J. B. Lucks, and D. R. Nelson, 2006, Proc. Natl. Acad. Sci. U.S.A. **103**, 12323.
Vitelli, V., and D. R. Nelson, 2004, Phys. Rev. E **70**, 051105.
Vitelli, V., and D. R. Nelson, 2006, Phys. Rev. E **74**, 021711.
Vitelli, V., and A. M. Turner, 2004, Phys. Rev. Lett. **93**, 215301.
Voll, P., N. apRoberts-Warren, and R. J. Zieve, 2006, e-print arXiv:cond-mat/0601395.
Volodin, A. P., M. S. Khaikin, and V. S. Edelman, 1977, JETP Lett. **26**, 543.
Wang, R. F., C. Nisoli, R. S. Freitas, J. Li, W. McConville, B. J. Cooley, M. S. Lund, N. Samarth, C. Leighton, V. H. Crespi, and P. Schiffer, 2006, Nature (London) **439**, 303.
Witten, T., 2007, Rev. Mod. Phys. **79**, 643.
Xing, X., 2008, Phys. Rev. Lett. **101**, 147801.
Yarmchuk, E. J., and R. Packard, 1982, J. Low Temp. Phys. **46**, 479.
Young, A. P., 1979, Phys. Rev. B **19**, 1855.
Zieve, R. J., and I. Newmann, 2010, private communication.